INTUITIVE TELEMANIPULATION OF MICRO-MANIPULATORS WITH PIEZOELECTRIC STICK-SLIP ACTUATORS WITH APPLICATION IN RETINAL SURGERY

by

Manikantan Nambi

A dissertation submitted to the faculty of
The University of Utah
in partial fulfillment of the requirements for the degree of

Doctor of Philosophy

Department of Mechanical Engineering

The University of Utah

December 2015

The University of Utah Graduate School

STATEMENT OF DISSERTATION APPROVAL

The dissertation of **Manikantan Nambi**

has been approved by the following supervisory committee members:

Jake J. Abbott	, Chair	**10/01/2015** Date Approved
Paul S. Bernstein	, Member	**10/14/2015** Date Approved
John M. Hollerbach	, Member	**10/20/2015** Date Approved
Stephen A. Mascaro	, Member	**10/15/2015** Date Approved
William R. Provancher	, Member	**10/02/2015** Date Approved

and by **Timothy A. Ameel**, Chair of

the Department of **Mechanical Engineering**

and by David B. Kieda, Dean of The Graduate School.

ABSTRACT

In this dissertation, we present methods for intuitive telemanipulation of manipulators that use piezoelectric stick-slip actuators (PSSAs). Commercial micro/nano-manipulators, which utilize PSSAs to achieve high precision over a large workspace, are typically controlled by a human operator at the joint level, leading to unintuitive and time-consuming telemanipulation. Prior work has considered the use of computer-vision-feedback to close a control loop for improved performance, but computer-vision-feedback is not a viable option for many end users. We discuss how open-loop models of the micro/nano-manipulator can be used to achieve desired end-effector movements, and we explain the process of obtaining open-loop models. We propose a rate-control telemanipulation method that utilizes the obtained model, and we experimentally quantify the effectiveness of the method using a common commercial manipulator (the Kleindiek MM3A).

The utility of open-loop control methods for PSSAs with a human in the loop depends directly on the accuracy of the open-loop models of the manipulator. Prior research has shown that modeling of piezoelectric actuators is not a trivial task as they are known to suffer from nonlinearities that degrade their performance. We study the effect of static (non-inertial) loads on a prismatic and a rotary PSSA, and obtain a model relating the step size of the actuator to the load. The actuator-specific parameters of the model are calibrated by taking measurements in specific configurations of the manipulator. Results comparing the obtained model to experimental data are presented.

PSSAs have properties that make them desirable over traditional DC-motor actuators for use in retinal surgery. We present a telemanipulation system for retinal surgery that uses a full range of existing disposable instruments. The system uses a PSSA-based manipulator that is compact and light enough that it could reasonably be made head-mounted to passively compensate for head movements. Two mechanisms are presented that enable the system to use existing disposable actuated instruments, and an instrument adapter enables quick-change of instruments during surgery. A custom stylus for a haptic interface enables intuitive and ergonomic telemanipulation of actuated instruments. Experimental results with a force-sensitive phantom eye show that telemanipulated surgery results in

reduced forces on the retina compared to manual surgery, and training with the system results in improved performance.

Finally, we evaluate operator efficiency with different haptic-interface kinematics for telemanipulated retinal surgery. Surgical procedures of the retina require precise manipulation of instruments inserted through trocars in the sclera. Telemanipulated robotic systems have been developed to improve retinal surgery, but there is not a unique mapping of the motions of the surgeon's hand to the lower-dimensional motions of the instrument through the trocar. We study operator performance during a precision positioning task on a force-sensing phantom retina, reminiscent of telemanipulated retinal surgery, with three common haptic-interface kinematics implemented in software on a PHANTOM Premium 6DOF haptic interface. Results from a study with 12 human subjects show that overall performance is best with the kinematics that represent a compact and inexpensive option, and that subjects' subjective preference agrees with the objective performance results.

CONTENTS

LIST OF FIGURES

LIST OF TABLES

ACKNOWLEDGMENTS

I am most grateful to my dissertation advisor, Dr. Jake Abbott, for his guidance and mentorship throughout my dissertation research. His hardworking attitude and passion for research is infectious. Without his persistent help, this dissertation would not have been possible. I would also like to thank my committee members, Dr. Paul Bersntein, Dr. John Hollerbach, Dr. Stephen Mascaro, and Dr. William Provancher, for their guidance over the course of my graduate career.

I would like to thank Dr. Bernstein, Dr. Nikhil Batra, and Dr. Jim Bell for introducing me to the world of retinal surgery. The wealth of information they provided during surgical observation was indispensable to the work presented in this dissertation. I would also like to thank Aayush Damani with whom I collaborated on the work presented in Chapter 3, and Alexandra Shamir for her technical assistance.

I would like to thank Intuitive Surgical Inc. for funding the work presented in Chapter 4 through their Technology Research Grant program, and the Moran Eye Center for assistance with surgical equipment.

I am thankful to my wonderful colleagues at the Telerobotics Lab for the innumerable stress-busting walks we took on campus, and for being a source of comic relief during testing times.

And finally, I would like to thank my family and friends for their unwavering support as I pursued my education thousands of miles away from home.

CHAPTER 1

INTRODUCTION

Piezoelectric stick-slip actuators (PSSAs) are widely used in applications that require micro- to nano-level precision because of their advantages such as very high resolution ($<$ 1 nm), high dynamic displacement range (cm–nm), and simple structure [1]. Commercially available stick-slip actuators [2–6] have become the preferred method of actuation for micro/nano-scale manipulation tasks inside a scanning electron microscope (SEM). To minimize the size of manipulators with PSSAs, most manipulators do not have integrated joint sensors. As a result, these manipulators are controlled in a very primitive manner, typically using joint control where the operator turns knobs to control each joint of the manipulator. The mapping between end-effector motion observed in a microscope image and joint commands is not intuitive, especially in cases where the manipulators are mounted on different stages at varying angles. Even simple manipulation tasks can often require up to eight manipulators working in concert, which exacerbates the problem.

Prior research has focused on using external sensors for implementing closed-loop control of PSSA-based manipulators [7, 8]. Such methods require additional sensors that are not easy to incorporate in SEMs, which are typically shared resources, and modifications to SEMs are seldom allowed. We would like the human operator to telemanipulate PSSA-based manipulators efficiently by looking at the image from a microscope, without requiring any additional modifications to the system. To this end, we present an algorithm in Chapter 2 to implement rate control of the end-effector attached to a PSSA-based manipulator. The algorithm uses open-loop models of the joints to obtain an estimate of joint positions, and calculates joint commands based on a desired velocity input for the end-effector. We discuss the efficacy of our algorithm for a telemanipulated micromanipulation task, and analyze drift due to imprecise joint estimates.

Accurate models of the joints of PSSA-based manipulators are required to estimate joint positions in the absence of sensor feedback. Mathematical models for PSSAs have been developed in [9–12] for custom actuators developed in research laboratories. However,

these methods require knowledge of actuator-specific parameters that are not available for commercially available PSSA-based manipulators. Chapter 3 describes methods for empirically obtaining load-dependent open-loop models for the joints of a PSSA-based manipulator. The proposed methods use measured data from the manipulators and can be applied to a wide range of commercially available manipulators that lack sensor feedback. These open-loop models can be used with methods developed in Chapter 2 for improving efficiency of the rate-control algorithm.

Chapters 2 and 3 are aimed toward improving telemanipulation efficiency when using PSSA-based manipulators for *general* micromanipulation tasks. However, we are particularly interested in the use of these manipulators for retinal surgery, which has received little attention. Characteristics such as high resolution, conditional backdrivability, small size, and low weight are some of the desirable properties for a manipulator used in retinal surgery. Surgeons typically work in a workspace of few millimeters, often operating on objects as small as few micrometers. There is a risk of injury to vital structures due to involuntary hand tremor and extremely low force tolerances (few mN), especially as fatigue sets in when surgery is performed over a number of hours. Further, the surgeons have to compensate for factors such as patient movement and operating in unintuitive frames of reference, similar to what surgeons experience during laparoscopic surgery.

There are a number of fundamental problems with existing robot-assisted retinal-surgery systems that do not address some of the major requirements of retinal surgery. Existing systems for retinal surgery are typically bulky table-mounted systems that use traditional DC motors as actuators. Additionally, these systems are not backdriveable, which leaves the patient's eye, and potentially their skull, at risk in case of equipment malfunctions. Chapter 4 describes the development and experimental evaluation of a novel telemanipulation system for retinal surgery that capitalizes on the advantages of PSSAs. Of the many systems designed for robot-assisted retinal surgery, only one other has considered a PSSA-based manipulator [13], in spite of their desirable properties. Our system comprises a compact head-mountable manipulator that uses commercially available PSSAs, and a modified Geomagic Touch haptic interface that enables intuitive telemanipulation of the end-effector attached to the manipulator. One of the most significant contributions of our system relative to existing systems is that our system incorporates a quick-change adapter that enables the full range of existing disposable retinal-surgery instruments to be utilized with the manipulator.

Haptic interfaces with a variety of kinematics have been utilized for telemanipulating

retinal-surgery systems. Kinematics that mimic the orientation of the instrument in manual retinal surgery were used in [14] and [15]. A master interface with underactuated kinematics was developed in [16] for precision tasks in neuro- and retinal surgery, and the telemanipulation system introduced in Chapter 4 locks the gimbal joint of the haptic-interface to enforce a one-to-one mapping between the master and slave degrees of freedom. The data available in the literature do not sufficiently justify the choice of a particular haptic-interface kinematics over the others. Chapter 5 describes our work on comparing operator performance with different haptic-interface kinematics for a task that is representative of telemanipulated retinal surgery. We find that the operators' overall performance is best with the kinematics that represent a compact and inexpensive option, and that the operators' subjective preference agrees with the objective performance results.

Recently PSSAs have been developed that have integrated joint sensors [6], which were used in the manipulator introduced in Chapter 4. Adding joint sensors to the family of manipulators similar to the Kleindeik MM3A [3] does not seem feasible because of their small size and compact construction. Regardless, the methods developed in Chapters 2 and 3 will improve telemanipulation performance for PSSAs both with and without joint sensors. For manipulators that have integrated joint sensors, such as the retinal-surgery manipulator used in Chapters 4 and 5, the joint sensor data eliminate any drift in the position due to the inaccuracies in the open-loop models. Accuracy of the open-loop models used certainly affect the closed-loop response of the actuators.

During the course of this work, a number of valuable lessons were learned regarding the efficacy of robot-assisted retinal surgery. Based on these lessons, recommendations are made for future work in Chapter 6. Finally, appendices are included that give additional details of the retinal-surgery telemanipulation system.

CHAPTER 2

TOWARD INTUITIVE TELEOPERATION OF MICRO/NANO-MANIPULATORS WITH PIEZOELECTRIC STICK-SLIP ACTUATORS

The work in this chapter was presented by Manikantan Nambi at the 2011 IEEE/RSJ International Conference on Intelligent Robots and Systems in San Francisco, CA, USA, and was published in [17]. It is included here without modification.

2.1 Introduction

With visualization from scanning and transmission electron microscopes (SEMs/TEMs), as well as light microscopes, researchers are able to conduct experiments and construct devices with a precision of only a few nanometers. State-of-the-art micro/nano-manipulators currently enable: manipulation and isolation of individual nanomaterials and nanostructures for imaging and analysis, 3D construction and characterization of MEMS/NEMS, failure analysis in semi-conductor fabrication, and surgery on individual cells [18–20]. The development and use of commercial manipulators like the Kleindiek MM3A [3], the Zyvex Nanomanipulator [2], Imina Technologies miBot [4], and the Attocube Nanopositioners [5] has increased with the demand for precise standardized tools for micro/nano-manipulation.

Among the limited range of actuators available, piezoelectric stick-slip actuators have become the foundation of modern micro/nano-manipulation (Fig. 2.1). They have a very simple structure, high positional accuracy, unlimited movable distance, and have high stability and stiffness as they are supported by guiding surfaces [1]. These actuators consist of a piezoelectric element and a sliding mass that moves relative to the piezoelectric element. They have two modes of operation, namely the fine mode and the coarse mode. In the fine mode, used to achieve the highest resolution possible, a slowly varying voltage is applied to the piezoelectric element resulting in a stretch, and friction between the piezoelectric element and the sliding mass causes the mass to move continuously with the piezoelectric element. In the coarse mode, used to take relatively large discrete steps, the applied voltage is quickly reversed after the initial stretch, resulting in a net displacement of the sliding mass relative to the piezoelectric element, as depicted in Fig. 2.1.

Rate control, which allows a user to command the end-effector of a manipulator at a desired speed and direction by coordinating the motion of the joints, has been known to the robotics community for decades, yet micro/nano-manipulators are operated in an inefficient open-loop manner using individual joint control (e.g., one knob per joint), ultimately due to the lack of sensor feedback at the joints. It is not always clear what combination of joint commands will lead to a desired end-effector movement from only a microscope image. In addition, manipulators are often mounted on moving stages and on different surfaces at varying angles. The user observing the end-effector of such a manipulator under a microscope has to perform the difficult task of mapping the image frame to his/her egocentric frame of reference. Use of multiple manipulators further complicates the situation. Thus, micro/nano-manipulation is currently unintuitive and time consuming.

Closed-loop control of micro/nano-manipulators using sensory data in real-time is chal-

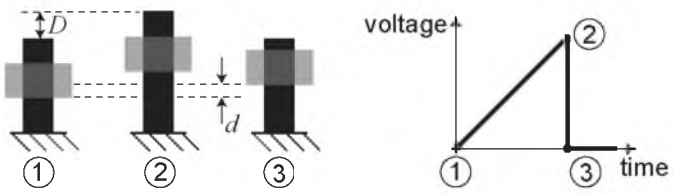

Figure 2.1. Functional description of a piezoelectric stick-slip actuator. A saw-tooth voltage is applied to the piezoelectric element. As the voltage slowly increases from 1 to 2, the piezoelectric element stretches by a distance D, and due to stick-slip friction between the piezoelectric element and the sliding mass, the sliding mass also advances. When the voltage is quickly reduced from 2 to 3, the piezoelectric element quickly shrinks, but the inertia of the sliding mass prohibits it from moving backward as quickly, resulting in a net forward displacement of the sliding mass of $d < D$.

lenging due to difficulty in getting real-time nanoscale visual and force feedback [20]. A number of different feedback control schemes such as voltage/frequency control [21], hybrid control [22], and sliding mode control [23] have been implemented for stick-slip actuators. Others have utilized vision feedback from SEM [7] and optical-microscope [8] images. Saeidpourazar and Jalili [24], [25] developed an adaptive controller to estimate the parameters of the manipulator on-line, and fused visual servoing and force feedback to enable closed-loop automatic control of the MM3A. Although using vision feedback has been shown to be successful for micro/nano-manipulation, it might not be feasible for many end users who work on shared SEMs, requiring them to book and pay for usage time. It can be difficult to implement a vision system on a shared SEM, owing to their high cost and sensitive nature.

The goal of our research is to enable teleoperated rate control of micro/nano-manipulators without relying on any feedback from the vision system, other than the human user looking at the microscope image. Specifically, we would like to 1) empirically model micro/nano-manipulators so that reliable position estimates can be obtained in the absence of feedback, 2) develop methods to calibrate the micro/nano-manipulators *in situ* to reduce modeling errors that can be introduced due to changes in environmental conditions or applied loads, 3) develop control methods to move the end-effector using position estimates obtained from the aforementioned models, and 4) develop methods to mitigate drift due to joint-estimate errors. In this paper, we focus exclusively on the coarse mode of operation.

Accurate modeling of piezoelectric stick-slip actuators is not a trivial task as they are known to suffer from nonlinearities such as hysteresis, creep, and drift, which degrade their performance. These actuators are also susceptible to environmental changes. However, a

number of studies on piezoelectric drives have shown that it might be possible to reliably model these actuators. Peng and Chen [11] developed a model to explain the effect of end-effector masses on their stick-slip actuator. Lockwood *et al.* [12] found that when gravitational force was acting parallel to the axis of their stick-slip actuator, the step size and corresponding displacement rate in the 'downward' direction was observed to be 14.7% greater than in the 'upward' direction. Inertial drives developed at ETH Zurich were found to have open-loop error of less than 1% [26]. In a study most closely related to ours, Tonet *et al.* [27] studied different strategies for time-delayed teleoperation of systems using an MM3A, under direct vision feedback. They used incremental position control for master-slave coupling; in their variable step amplitude strategy, which allowed for the greatest precision, the user sacrificed control of the manipulator once a command was sent to the manipulator, losing the ability to correct for error in position attained by the manipulator.

2.2 The Impulsive Manipulator Jacobian

Micro/nano-manipulators such as the MM3A are kinematically no different from traditional robotic manipulators; we can relate joint movement to end-effector movement through a configuration-dependent manipulator Jacobian $J(\vec{q})$ as $\dot{\vec{x}} = J(\vec{q})\dot{\vec{q}}$, where $\vec{q}$ is the vector of joint positions, $\vec{x}$ is the position of the end-effector, and the "dot" indicates a time derivative. For a desired end-effector movement $\dot{\vec{x}}_d$, we can simply command the joints to move as $\dot{\vec{q}} = J^{-1}(\vec{q})\dot{\vec{x}}_d$, assuming the Jacobian is invertible. However, this method makes two critical assumptions that are potentially invalid in the case of micro/nano-manipulators. First, although the form of the Jacobian can be found analytically, its calculation is dependent on knowledge of the current configuration, and commercial micro/nano-manipulators are not equipped with sensor feedback of the joint positions. Second, the discrete stick-slip nature of the piezoelectric actuators, combined with the lack of sensor feedback, makes directly controlling the velocity of each joint, $\dot{\vec{q}}$, challenging.

Dynamically, a serial-link micro/nano-manipulator such as the MM3A has the same governing Lagrangian dynamic equation as a traditional robotic manipulator:

$$M(\vec{q})\ddot{\vec{q}} + C(\vec{q},\dot{\vec{q}})\dot{\vec{q}} + G(\vec{q}) - J^T(\vec{q})\vec{f} = \vec{\tau} \tag{2.1}$$

where $\mathrm{M}(\vec{q})$, $\mathrm{C}(\vec{q},\dot{\vec{q}})$, and $\mathrm{G}(\vec{q})$ are configuration-dependent inertia, Coriolis, and gravity matrices, respectively, $\vec{f}$ is any load applied to the end-effector, and $\vec{\tau}$ is the vector of joint torques/forces. This equation is useful to control traditional robotic manipulators, where we have control over joint torques. However, in the case of micro/nano-manipulators, we can only command discrete steps. Because (2.1) is still a valid dynamic equation, the

configuration-dependent matrices M($\vec{q}$), C($\vec{q}, \dot{\vec{q}}$), and G($\vec{q}$) affect the end-effector's movement during a single discrete step, but how they affect the movement is currently unknown.

Experiments indicate that the average step size of the actuators is affected by inertial load (m), static loads (g), and environmental factors. We hypothesize that a function γ can be constructed for a given joint that maps the above factors to a joint step size $\Delta q = \gamma(m, g, \vec{\alpha}, \delta)$, where $\vec{\alpha}$ is the set of joint-specific parameters to be determined through calibration. The values m and g can be taken from the appropriate entries from M and G in (2.1). The average step size can be a function of the number of steps commanded if they are commanded too quickly to be considered independent, so γ is a nonlinear function of δ in general.

For very small steps, the Jacobian can be approximated as $\Delta\vec{x} = J(\vec{q})\Delta\vec{q}$, where small joint steps $\Delta\vec{q}$ lead to small end-effector steps $\Delta\vec{x}$. Using an open-loop model γ for each joint, we can relate the joint step size of the manipulator to the joint step commands as

$$\Delta\vec{q} = \Gamma(M(\vec{q}), G(\vec{q}), A, \vec{\delta})\vec{\delta} \tag{2.2}$$

where the matrix Γ is diagonal with the i^{th} element being the function γ described above for the i^{th} joint, and the vector $\vec{\delta}$ contains the integer number of steps commanded to each joint, with sign indicating direction. The relationship (2.2) assumes that the joint step commands are given sequentially. Finally, an *impulsive manipulator Jacobian* J_δ is formed as

$$\Delta\vec{x} = J(\vec{q})\Gamma(M(\vec{q}), G(\vec{q}), A, \vec{\delta})\vec{\delta} = J_\delta\vec{\delta} \tag{2.3}$$

The result is an open-loop model relating impulsive joint step commands to movements of the micro/nano-manipulator in both joint space and Cartesian space.

2.3 Rate-control Teleoperation

When operating under a microscope, only a magnified view of the end-effector is visible to the user. We would like the user to be able to command a desired velocity to the end-effector (both direction, and magnitude within bounds) using only what can be observed in the image. We would like the actual velocity to be as close to the intended velocity as possible, but hypothesize that humans will be able to account for small errors with limited cognitive load [28]. We would like the discrete-step nature of the controller to be transparent to the user. To realize this goal, we propose a rate-control method that handles the step commands for the user, based on commanded end-effector velocity.

Algorithm 1 shows the basic steps for the proposed method. The algorithm is called in a continuous loop by the software controlling the manipulator, which we assume is running

with a constant time step of Δt seconds. The algorithm takes the desired input velocity ($\dot{\vec{x}}_d$) commanded by the user (e.g., from an input device such as a joystick) and returns the number of steps ($\vec{\delta}$) to be taken at each joint during the current cycle. Starting from current estimates of end-effector position $\vec{x}$ and joint-configuration $\vec{q}$, a proxy point ($\vec{p}$) is projected away by a distance $\dot{\vec{x}}_d \Delta t$, giving the desired end-effector location. The number of steps that the manipulator should take to reach the proxy is then calculated as $\vec{\delta}_{real}$ by inverting the impulsive manipulator Jacobian. However, the result is a vector of real numbers that must be converted to an integer number of steps to be commanded as $\vec{\delta}$; we simply round to the nearest integer. This rounding step implies that we will never perfectly attain the desired proxy position. The estimated final joint configuration ($\vec{q}_f$) is then calculated based on the steps actually commanded, and the final end-effector position ($\vec{x}_f$) is estimated using the manipulator's kinematic model. Finally, the current estimates of end-effector position and joint configuration are updated for the next cycle. The algorithm sequence as given assumes that Γ is not a function of $\vec{\delta}$; if it is, then lines 4–8 must be called iteratively from an initial guess of $\vec{\delta}$ until it converges.

We have also explored an alternative to the basic algorithm, which we will call Algorithm 2. It is identical to Algorithm 1, except that Line 2 is replaced by

$$\vec{p} = \vec{p} + \dot{\vec{x}}_d \Delta t \tag{2.4}$$

Algorithm 2 maintains memory of the proxy position from the last cycle, which can be beneficial considering that the previous desired proxy position was not perfectly attained.

Algorithm 1 Proxy-based rate control without memory

1: **read** $\dot{\vec{x}}_d$
2: $\vec{p} = \vec{x} + \dot{\vec{x}}_d \Delta t$
3: $\Delta\vec{x} = \vec{p} - \vec{x}$
4: $\Gamma = \text{compute}\Gamma(M(\vec{q}), G(\vec{q}), A, \vec{\delta})$
5: $J = \text{compute}J(\vec{q})$
6: $J_\delta = J\Gamma$
7: $\vec{\delta}_{real} = J_\delta^{-1}\Delta\vec{x}$
8: $\vec{\delta} = \text{round}(\vec{\delta}_{real})$
9: $\Delta\vec{q} = \Gamma\vec{\delta}$
10: $\vec{q}_f = \vec{q} + \Delta\vec{q}$
11: $\vec{x}_f = \text{forwardKinematics}(\vec{q}_f)$
12: $\vec{x} = \vec{x}_f$
13: $\vec{q} = \vec{q}_f$
14: **return** $\vec{\delta}$

Fig. 2.2 shows the simulation results for a 2D task in a horizontal plane for both algorithms applied to the MM3A. A 2D task in the horizontal plane can be performed by actuating joints 1 and 3, and fixing joint 2 at $q_2 = -\pi/2$ (i.e., outstretched as shown in Fig. 2.3); the kinematics of the resulting 2-DOF manipulator are trivial to compute, and are omitted here. For this simulation, the initial position $\vec{x}_i$ is computed for the joint configuration $\vec{q} = [0, -\pi/2, 0]^T$. The desired target position $\vec{x}_t$ to be reached by the user is set at a distance of $50\,\mu m$ from the initial position at an angle of 30° from the x-axis. In our simulation, we assume an ideal human operator that is trying to reach $\vec{x}_t$ at a rate of 0.1 mm/s, and that always points the desired velocity of the end-effector perfectly from the current end-effector location toward $\vec{x}_t$. The simulation is stopped when the error between $\vec{x}$ and $\vec{x}_t$ is less than $5\,\mu$m. We are assuming the model of the micro/nano-manipulator to be perfect in this simulation, but in reality, the actual position observed under the microscope will be different from that estimated; this issue will be discussed subsequently.

For some low velocities, Algorithm 1 shows a drift as can be seen in Fig. 2.2. Because the algorithm updates the proxy from the end-effector's current position, at low velocities, it decides that taking a step along the x-axis and no step along the y-axis is the best solution for many cycles. This is due to the rounding of $\vec{\delta}_{real}$ to $\vec{\delta}$, and is a function of the end-effector

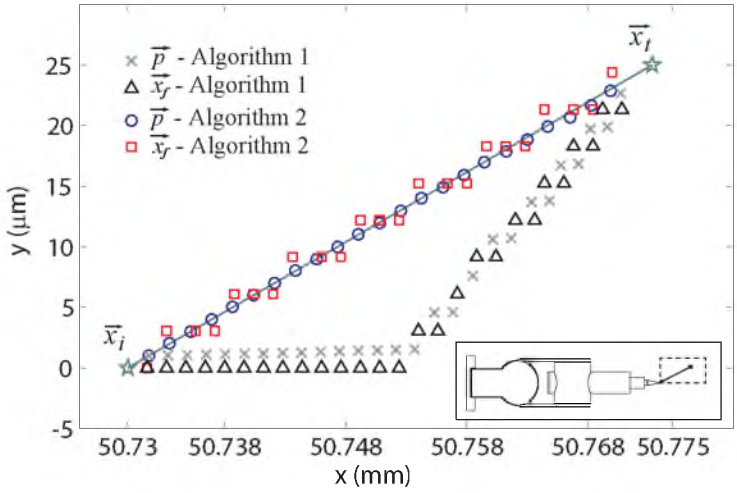

Figure 2.2. Simulation results for Algorithms 1 and 2 implemented on an MM3A, for a 2D task in a horizontal plane. At each instant, the user commands the end-effector to move from its current location toward $\vec{x}_t$ at 0.1 mm/s. A line joining $\vec{x}_i$ and $\vec{x}_t$ is shown for reference. The step-size model used has $\gamma_1 = 60\,\mu$rad and $\gamma_3 = 0.8\,\mu$m, where γ_1 and γ_3 are diagonal elements of Γ. Inset shows the top view of the MM3A with its workspace in the horizontal plane used in simulation.

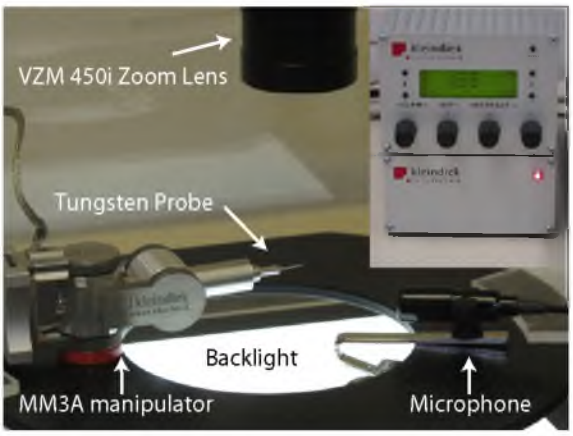

Figure 2.3. Experimental setup. A tungsten probe with a tip diameter of 1 μm is attached as an end-effector. The NanoControl unit is shown in the inset.

step $\Delta\vec{x}$ caused by each joint. As the direction of commanded velocity is updated by the ideal operator, at some point, the error along the y-axis will be high enough for the algorithm to command movement in that direction. In Algorithm 2, because the proxy is updated from its previous position, it acts as memory of the previous error between commanded and actual velocity and is able to compensate for this error. Algorithm 2 appears to have better performance than Algorithm 1, but this is due to the target position being stationary. If we assume that the period Δt is small compared to human bandwidth, then Algorithm 2 is likely to give desirable performance even if the desired target $\vec{x}_t$ is changing. A high value of Δt would cause larger deviations of the end-effector from the desired path and could result in unstable behavior as the operator tries to overcorrect for the deviation. If the commanded velocity is below a certain threshold, then Algorithm 1 will result in no movement of the end-effector with no error accumulation, but using Algorithm 2 will cause the proxy to keep moving until sufficient distance has been generated such that the end-effector can take a step toward the proxy; whether or not this property is desirable requires further research.

2.4 Experimental Methods

2.4.1 Apparatus

2.4.1.1 MM3A manipulation system

The Kleindiek MM3A manipulation system consists of the MM3A micromanipulator and the NanoControl (NC) unit (Fig. 2.3). The MM3A manipulator has a RRP configuration with two rotary (R) and one prismatic (P) joint. The MM3A has two modes of operation, the fine mode and the coarse mode, which enable it to achieve high resolution of up to 0.25 nm for the P joint and 10^{-7} rad for the R joints in the fine mode, and high speeds of

up to 10 mm/s in the coarse mode.

The NC unit is used to command control signals to the MM3A. It has a four knobs, three of which are used to control the individual joints on the MM3A in both the fine and the coarse mode. The number of steps to be taken by a joint for a turn of the knob can be set in the NC unit. Commands can also be sent to the NC unit via a serial port as a string of the form "Mode δ Joint", where mode is either 'coarse' or 'fine', "δ" is an integer value which specifies the number of steps to be taken in each command with sign indicating direction, and "Joint" is either "A", "B", or "C" corresponding to joints 1, 2, and 3, respectively. Only one joint can be controlled by the NC unit per command. Hence, three commands have to be sent sequentially to control the three joints of the MM3A.

2.4.1.2 Vision System

A Basler A601fc firewire camera with a VZM 450i zoom lens is used to obtain position information for experiments herein (Fig. 2.3). The VZM 450i has a primary magnification of 0.7× – 4.5×, with a respective field view of 12.0 mm – 1.9 mm. The Basler A601fc has a resolution of 659× 491 pixels with a maximum frame rate of 60 fps. The vision system has a resolution of 10 μm at a magnification of 1× for the lens. An LED backlight was used as the primary light source for the vision system.

2.4.1.3 Software

A custom GUI program developed in C++ using the Qt 4.6 ui framework and OpenCV vision library was used to collect calibration data and implement teleoperation. The program communicates with the NC unit using serial communication. Once a command is sent to the NC unit, the software waits for feedback from the NC unit, which indicates the execution of a command. Audio inputs are taken from a microphone and the Fast Fourier Transform (FFT) of the audio signal is computed for the calibration method described below. Counters are used to keep track of the number of commands (n) commanded to each joint, and the total number of steps along a joint is given by $\sum_{i=1}^{n} |\delta_i|$.

OpenCV library is used to capture frames from the camera at a rate of 60 fps, and a blob-detection algorithm is run to track the tip of the tungsten probe attached to the manipulator in real time. Commands for a single joint are given to the NC unit at a rate of 100 Hz. The program was run on a Dell Optiplex computer (2 Ghz Dual Core, 2 GB ram) running the Ubuntu 10.04 operating system.

2.4.2 Calibration

To use the impulsive manipulator Jacobian, we need accurate knowledge of Γ, which relates joint step commands $\vec{\delta}$ to the joint step size $\Delta\vec{q}$. A deterministic Γ would result in the best performance for the algorithms in Section 2.3, but due to uncertainty in the step size and lack of sensor feedback in the MM3A, we calculate the average step size as:

$$\overline{\gamma}_i = \frac{R_i}{\delta_{t,i}} \tag{2.5}$$

where $\overline{\gamma_i}$ is the average step size for a joint i, R_i is the total range of motion for joint i ($4\pi/3$ rad for joints 1 and 2, and 12 mm for joint 3), and $\delta_{t,i}$ is the total number of steps required to travel across R_i: $\delta_{t,i} = |\delta|n$, where n is the number of commands given to a joint at δ steps/command.

The displacement of the end-effector for a single step along a joint is so small that it is not visible to the naked eye. Hence, it is not possible to visually detect that a joint has reached the limit of its joint space. However, there is a perceptible change in sound made by the manipulator when a joint of the MM3A hits a mechanical stop as it reaches the limit of its travel, and the software detects this intensity rise in the FFT of the audio signal (captured by the microphone) at a frequency of 2.7 kHz. This property was used to develop an audio limit switch that enables us to accurately detect the end of travel for a joint. The change in intensity of the FFT has to be tuned for each joint.

The values of $\overline{\gamma}_i$ are measured before the start of an experiment to reduce the effect of environmental changes, as there is a significant change in step size from day to day. As the experiments in this paper are performed in a horizontal plane using joints 1 and 3, only $\overline{\gamma}_1$ and $\overline{\gamma}_3$ are measured. Joints 1 and 3 are moved across R_1 and R_3 by commanding a single step ($\delta = 1$) in each command, and $\delta_{t,1}$ and $\delta_{t,3}$ are obtained. Γ is constructed by substituting the diagonal elements Γ_1 and Γ_3 with $\overline{\gamma}_1$ and $\overline{\gamma}_3$. Two different step size models $\overline{\gamma}_1$ and $\overline{\gamma}_1(q_3)$ were evaluated. For the constant value of $\overline{\gamma}_1$, q_3 is kept at zero. $\overline{\gamma}_1(q_3)$ takes into account the increase in inertial load on joint 1 due to the position of joint 3. To determine the effect of increase in inertial load, the number of steps required by joint 1 to travel across R_1 with $q_3 = 0$ mm and $q_3 = 12$ mm are determined as $\delta_{t,1,0}$ and $\delta_{t,1,12}$, respectively. The step size function $\overline{\gamma}_1(q_3)$, which gives a configuration dependent step size for joint 1, is then calculated using linear interpolation as:

$$\overline{\gamma}_1(q_3) = \frac{R_1}{\delta_{t,1,0} + (\delta_{t,1,12} - \delta_{t,1,0})\left(\frac{q_3}{R_3}\right)} \tag{2.6}$$

Before starting an experiment, each joint is driven along the full range of its motion three times to reduce any warming effect that might be present in the actuators.

2.4.3 Experiments

Experiments were designed to test the effectiveness of the proposed method with the MM3A. For this purpose, a 2D task was performed in the horizontal plane using joints 1 and 3, with the simulated ideal human operator driving the manipulator from the initial position ($\vec{x}_i$) to the desired target position ($\vec{x}_t$) (Fig. 2.4). At the start of a trial, the initial position ($\vec{x}_i$) is computed for the joint configuration $\vec{q} = [0, -\pi/2, 0]^T$. In the initial position, a step along joint 3 leads to tip movement along the x-axis and a step along joint 1 leads to tip movement along the y-axis. The desired target position ($\vec{x}_t$) is set at a distance of 4 mm from $\vec{x}_i$, at different angles of $\theta = 0°, 30°, 60°$, and 90° from the x-axis. The ideal human operator is given the position of the tip (i.e., the end-effector) from the vision system, so that it can always point the desired input velocity ($\dot{\vec{x}}_d$) towards $\vec{x}_t$. The number of steps to be taken by the manipulator $\vec{\delta}$ in each cycle is then calculated using Algorithm 2, and a set of two commands corresponding to joints 1 and 3 are sequentially sent to the NC unit with a period of 0.01 s between commands. As the ideal human operator is continuously correcting $\dot{\vec{x}}_d$ to point towards $\vec{x}_t$, the tip will always reach $\vec{x}_t$. However, the estimated position $\vec{x}_f$ will be different than $\vec{x}_t$ because of modeling errors. Trials are conducted with the ideal human operator commanding two different velocities of $|\dot{\vec{x}}_d| = 0.05$ mm/s and 0.5 mm/s. At the end of each trial, the position of the tip is manually reset to $\vec{x}_i$. Five trials are conducted for each $|\dot{\vec{x}}_d|$ and θ value. Due to limitations in the speed of serial communication and the time taken for executing a coarse step by the manipulator, a maximum of 24 coarse steps can be commanded to the manipulator along a joint when using a rate of 100 Hz. Hence, the maximum magnitude of velocity that can be achieved by the manipulator at any instant, at any point in the 2D workspace under consideration, is limited by the maximum value of $24\overline{\gamma}_{min}$, where $\overline{\gamma}_{min}$ is the average step size of the joint with smaller end-effector movement

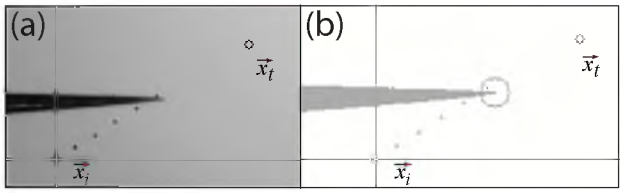

Figure 2.4. Experimental results, corresponding to the simulation of Fig. 2.2. (a) Screenshot of the camera-image display on the GUI with the end-effector moving at $\dot{\vec{x}}_d = 0.5$ mm/s. (b) Screenshot of the display after applying blob detection algorithm. The medium circles indicate the initial ($\vec{x}_i$) and desired positions ($\vec{x}_t$) at the start of a trial. The large circle indicates the probe tip as seen by the vision system and the small circles show the history of estimated positions during the trial.

for a single step. The experiments were carried out for the two step size models $\overline{\gamma}_1$ and $\overline{\gamma}_1(q_3)$.

2.5 Results and Discussion

As a metric to quantify the error in our step-size models, we use the relative error in the estimated position defined as:

$$E_r = \frac{|\vec{x}_f - \vec{x}_t|}{|\vec{x}_t - \vec{x}_i|} \tag{2.7}$$

where $\vec{x}_f$ is the estimated position of the end-effector and $\vec{x}_t$ is the target position (and actual position, within the convergence criterion) reached by the end-effector in a trial. E_r gives the relative error between the actual and estimated position of the end-effector with respect to the total displacement.

Fig. 2.5 shows experimental results for E_r plotted against θ, for different values of $|\dot{\vec{x}}_d|$, for step size models $\overline{\gamma}_1$ and $\overline{\gamma}_1(q_3)$. E_r seems to increase with an increase in $|\dot{\vec{x}}_d|$. A higher value for E_r at a velocity of 0.5 mm/s can be explained by the fact that the models $\overline{\gamma}_1$ and $\overline{\gamma}_1(q_3)$ were measured at $\delta = 1$. At $|\dot{\vec{x}}_d| = 0.05$ mm/s, δ commanded to each of the joints is at most 1, while at $|\dot{\vec{x}}_d| = 0.5$ mm/s, value of δ commanded to each joint is much higher than 1. As δ increases, there is significant change in the step size and hence, higher velocities lead to a higher value for E_r.

$\overline{\gamma}_1(q_3)$ seems to be a better predictor of step size than $\overline{\gamma}_1$ at $|\dot{\vec{x}}_d|$=0.05 mm/s. For stick-slip actuators, we would expect that an increase in inertial load would increase the

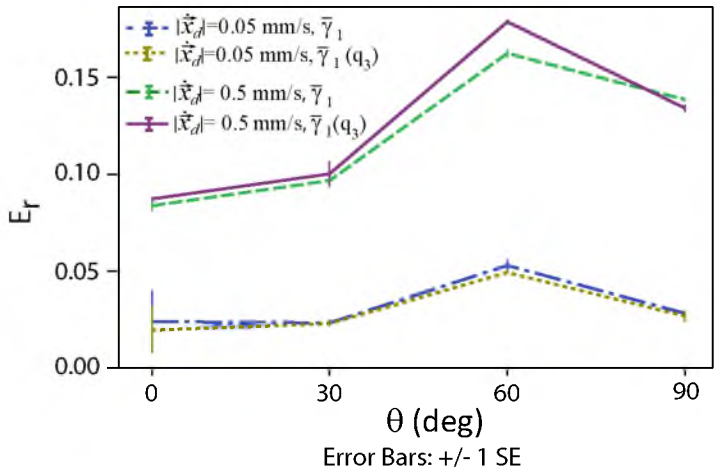

Figure 2.5. Experimental results for E_r. The step size models used were $\overline{\gamma}_1 = 68\,\mu rad$, $\overline{\gamma}_1(q_3) = (14688 - 171q_3)^{-1}\,\mu rad$, and $\overline{\gamma}_3 = 0.77\,\mu m$.

efficiency of the stick-slip phase and result in an increase in step size. We observe this behavior for joint 1 at $\delta = 1$ and $\delta = 2$, but at values of $\delta > 2$, this effect is reversed and inertial load seems to reduce the step size. This results in degraded performance for model $\overline{\gamma}_1(q_3)$ at high velocities.

E_r has a maximum value of around 20% for velocities considered in this paper, which corresponds to a maximum error of about 20% in the joint estimates. Unless we have a perfect model of the manipulator, the error in joint estimates will accumulate over time resulting in an unintuitive response from the system for a given user input. From the experiments conducted herein, we know that even with an error of 20% in the joint estimates the ideal human operator is able to position the end-effector within 1 pixel of the desired target position in a stable manner. It was observed that even if the joint estimates were always set to the initial joint configuration (i.e., the joint estimates were not updated), the ideal human operator was able to position the end-effector accurately with no visible drift in the path taken by the end-effector as compared to the path taken when the joint estimates were being updated. When the joint estimates are not being updated, there would be no drift in joint estimates, but an error in the estimated Jacobian (maximum of 8% for the workspace used) due to the error in the joint estimates would result in an error in the velocity actually achieved by the manipulator. The fact that the ideal human operator is able to position the end-effector accurately means that this error in velocity is relatively low, and we believe that a human operator should also be able to compensate for small errors in velocity. Thus, in small workspaces typically encountered in micro/nano-manipulation, drift in joint estimates can be avoided by setting the joint estimates to a fixed known configuration. In the future, we would like to develop drift-mitigation techniques that would allow the human operator to use the manipulator for long periods of time without the need for recalibration.

The ideal human operator has infinite visual resolution and no processing time delay. However, this is not true of a real human operator. Thus, stability of our method has to be tested with human subject tests.

From step-size measurements recorded under different loading conditions and orientations for the joints, we know that there is a significant effect of inertial loads, static loads, and δ on the step size. The step size for joint 3 was found to vary by more than 50% when gravity was acting along the axis of the joint. However, the trends in step size are highly repeatable, which tells us that a model of the manipulator joints of the form of (2.2) can be developed. Additionally, the current calibration routine for joints 1 and 3 are run at $\delta = 1$, which takes about 25 minutes to complete. Using a model that takes into account

the effect of δ would allow us to perform the calibration routine in a shorter period of time by using a higher value for δ during calibration. We would like to develop efficient calibration techniques that would take advantage of the observed trends in step sizes and enable us to obtain a complete open-loop model of the manipulator with a minimum number of measurements.

2.6 Conclusions

In this paper, we have presented a rate-control teleoperation method for control of manipulators using stick-slip actuators. The formulation of an impulsive manipulator Jacobian was explained, which enables us to use open-loop models of the manipulator to solve for the input number of steps required by the manipulator for a desired end-effector movement. Experimental results quantifying the effectiveness of the proposed methods were presented. We found that effective teleoperation is possible despite inaccurate joint measurements, and we discussed ways to minimize errors.

CHAPTER 3

AN EMPIRICAL STUDY OF STATIC LOADING ON PIEZOELECTRIC STICK-SLIP ACTUATORS OF MICROMANIPULATORS

The work in this chapter was conducted by Aayush Damani and Manikantan Nambi, who contributed equally. It was presented by Manikantan Nambi at the 2012 International Symposium on Experimental Robotics in Quebec City, Canada, and was published in [29]. It is included here without modification.

3.1 Introduction

Micromanipulation deals with small motions on the order of 10^{-3} to 10^{-6} m. Under the guidance of electron and optical microscopes, micromanipulation is now commonly used in the areas of MEMS construction and characterization, isolation and characterization of individual materials, and manipulation of single cells. The development and use of commercial manipulators like the Kleindiek MM3A [3], the Zyvex Nanomanipulator [2], Imina Technologies miBot [4], SmarAct Actuators [6], and the Attocube Nanopositioners [5] has increased with the demand for precise standardized tools for micromanipulation.

Piezoelectric stick-slip actuators have become the foundation of modern micromanipulation due to their simple structure, high positional accuracy, unlimited movable distance, and high stability due to support by guiding surfaces [1]. Due to their useful characteristics, these actuators have been extensively used in manipulation of micro/nano-sized objects, medical devices, camera lens actuation systems, and in bio-sciences [30,31]. These actuators consist of a piezoelectric element and a sliding mass that moves relative to the piezoelectric element (Fig. 3.1). Typically, these actuators have no sensor feedback (with the exception of SmarAct Actuators [6]), and hence, the individual joints of the manipulators are controlled open-loop, using one knob per joint. Due to difficulty in implementing real-time closed-loop controllers (which are generally based on vision feedback [8, 32]) for micromanipulators, methods to control them open-loop that capitalize on the intelligence of the human user are being developed [27, 33]. The utility of such methods depends directly on the accuracy of the open-loop models of the manipulator used.

Modeling of piezoelectric actuators is not a trivial task as they are known to suffer from nonlinearities such as hysteresis, creep, and drift, which degrade their performance [23, 34, 35]. A number of researchers have mathematically modeled the dynamics of piezoelectric stick-slip actuators [9, 10]. Peng *et al.* [11] used a pre-sliding friction model to explain the dynamics of stick-slip actuators, and obtained an empirical model for the effect of end-effector mass on the step size of the actuator. Lockwood *et al.* [12] found that when gravitational force was acting parallel to the axis of their stick-slip actuator, the step size and corresponding displacement rate in the downward direction was observed to be 14.7% greater than in the upward direction. Thus, it is known that static (i.e., noninertial) loads in the direction of motion of the actuator increases the step size and vice-versa. However, this effect has not been well characterized in the past.

In this paper, we study the effect of static loads on a prismatic and a rotary piezoelectric stick-slip actuator, obtain an empirical model relating the step size to the load, and develop

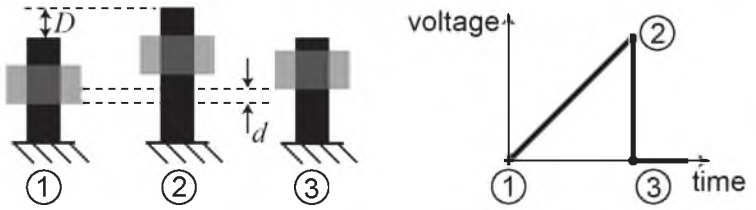

Figure 3.1. Functional description of a piezoelectric stick-slip actuator. A saw-tooth voltage is applied to the piezoelectric element. As the voltage slowly increases from 1 to 2, the piezoelectric element stretches by a distance D, and due to friction between the piezoelectric element and the sliding mass, the sliding mass also advances (stick phase). When the voltage is quickly reduced from 2 to 3, the piezoelectric element quickly shrinks, but the inertia of the sliding mass prohibits it from moving backward as quickly, resulting in a net forward displacement of the sliding mass of $d < D$ (slip phase). This is also known as the coarse mode of operation of the actuator. In the fine (traditional) mode, the voltage signal between 1 and 2 is controlled to achieve fine positioning.

a method to calibrate the parameters of the empirical model using measurements from the actuators. The modeling experiments presented herein were performed for the coarse (stepping) mode of operation of the actuator (Fig. 3.1). The empirical models derived can be used with algorithms developed in [33] to perform intuitive teleoperation of the micromanipulator's end-effector, rather than controlling individual joints. With piezoelectric stick-slip actuators, the step size is stochastic, with a hard-to-model variance about a load-dependent mean. The method presented in this paper deals with modeling this mean. The method is primarily designed to provide an accurate estimate of the size of the next commanded step, such that a user's desired motion command can be accurately mapped to a required number of joint steps. Having a more accurate model of joint stepping could also lead to a method to estimate the joint configuration in manipulators without joint sensing, but such estimation methods would be subject to drift, and as such would need to incorporate additional sensing methods to be useful in practice.

3.2 Technical Approach

The commonly used Kleindiek MM3A manipulator is used in this study (Figs. 3.2 and 3.3). It has three degrees of freedom (DOF) with two rotary joints and one prismatic joint, which use piezoelectric stick-slip actuators. Due to the discrete step nature of these actuators, as well as the MM3A's controller, commands are given in the form of number of steps to be taken along a given joint. The joints of the MM3A lack sensor feedback, hence, it is difficult to obtain accurate measurements of the step size. To study the effect of static loads on the step size of a joint j, we use the average step size given by:

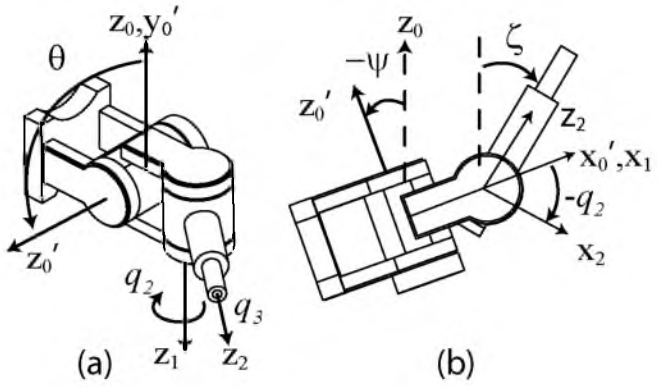

Figure 3.2. Kleindiek MM3A. With the z_0 axis initially vertical, the base frame is rotated by θ about x_0 and then rotated by ψ about the new y_0. (a) Isometric view at $\theta = 90°$. No gravitational loads acting on joints 2 or 3. (b) Side view at $\theta = 0°$, with gravitational loads acting on both joints 2 and 3. $\zeta = \psi - q_2$.

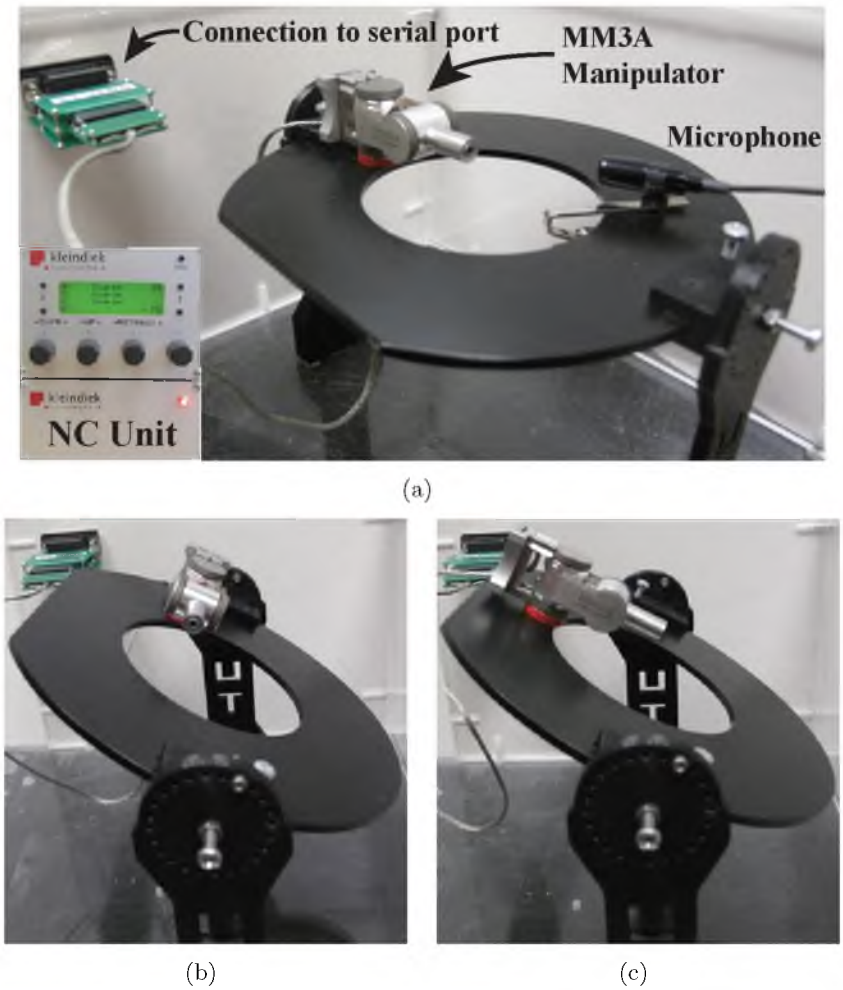

Figure 3.3. The Kleindiek MM3A manipulator is shown at different orientations. (a) $q_2 = -\pi/2$, $\theta = 0$, and $\psi = 0$ (b) $q_2 = -\pi/2$ and $\psi = 0$ at a particular θ (c) $q_2 = -\pi/2$ and $\theta = 0$ at a particular ψ.

$$\overline{\gamma}_{ji} = \frac{R_j}{N_{ji}} \tag{3.1}$$

where R_j is the total range of joint j ($4\pi/3$ rad for the rotary joints and 12 mm for the prismatic joint), N_{ji} is the total number of steps required by joint j to travel through R_j, and $i \in \{+, -\}$ indicates the direction of joint motion.

As the step size for each joint is small (on the order of 1 μm), it is difficult to visually detect when a joint reaches its end of travel. However, the actuators make a distinct noise when they hit a mechanical stop. This knowledge is used to develop an audio limit switch that detects the end of travel for a joint. Custom software monitors the sound from a microphone at each instant and computes the Fast Fourier Transform (FFT) of the audio signal. The change in sound when a joint hits a mechanical stop is detected as a peak in the power of the FFT. The frequency at which this peak occurs, and the intensity of the peak, is different for each joint and has to be tuned before each experiment.

By measuring $\overline{\gamma}_{ji}$ at different configurations of the manipulator, we study the effect of gravitational loads on the rotary and the prismatic joint (no other external forces are acting on the manipulator). Because an individual joint cannot distinguish a gravitational load due to the distal links from an equivalent load due to a force applied at the end-effector (passing through the manipulator's Jacobian), our results generalize to all static (i.e., noninertial) loads. Nonlinear regression is used to fit a function, based on our knowledge of the load acting on the actuator, to the empirical data, to obtain a relation for the step size of the form $\gamma_{ji} = \Gamma_{ji}(g, \alpha_{ji})$, where α_{ji} is a set of actuator specific parameters, and g is the gravity vector. The actuator specific parameters α_{ji} of the model are then calibrated for by using $\overline{\gamma}_{ji}$ measurements at selected configurations for each joint. Significance of unmodeled factors such as change in environmental conditions from day to day are analyzed by performing ANOVA on the data obtained for $\overline{\gamma}_{ji}$.

3.3 Results

This section contains the main empirical modeling results of this paper. The experiments that were conducted to obtain these results are detailed in Section 4.3.

3.3.1 Effect of unmodeled factors

Environmental conditions (e.g., temperature, humidity) are uncontrolled in our experiments, so we will not incorporate these factors into our model (although it is possible that they could be incorporated in the future [36]). To minimize these unmodeled effects on the open-loop control of the Kleindiek MM3A, we propose to calibrate the joints before

each session of use. This assumes that there is a significant change from day to day that warrants such recalibration. To substantiate this claim, the average step size for prismatic joint 3 and the rotary joint 2 in the positive ($\overline{\gamma}_{3+}$ and $\overline{\gamma}_{2+}$) and negative ($\overline{\gamma}_{3-}$ and $\overline{\gamma}_{2-}$) directions were taken on two different days, which would incorporate a change in environmental conditions. The positive direction for the prismatic joint means moving out from 0 mm to 12 mm as defined by the z_2 direction. For the rotary joint, the positive direction is defined by the right-hand rule about the z_1 axis. For the prismatic joint, the configuration of the manipulator was kept constant at $q_2 = -\pi/2$, $\theta = 0$, and $\psi = 0$ on both days, and three readings each of the step size values $\overline{\gamma}_{3+}$ and $\overline{\gamma}_{3-}$ were taken on each day. For the rotary joint, $\overline{\gamma}_{2+}$ and $\overline{\gamma}_{2-}$ was recorded at q_3=0 mm, $\theta = -\pi/2$, and $\psi = 0$. In these configurations, there is no effect of gravity on the joint being investigated, isolating the unmodeled factors of interest.

An ANOVA test on the data shows that the difference in step size on different days is statistically significant ($p < 0.05$) for both positive and negative directions for both the prismatic and the rotary joints. The ANOVA test also shows a significant difference in the step size between the positive and negative directions within a given day for both joints. Thus, calibration is recommended each time the manipulator is to be used, and different calibration parameters should be found for each direction of motion.

3.3.2 Modeling of a prismatic joint

Fig. 3.4 shows the results for the modeling experiments on the prismatic joint. The gravitational load on the prismatic joint is varied by changing the angles q_2, θ, and ψ (see Fig. 3.2). Curve 1 in Fig. 3.4a shows $\overline{\gamma}_{3+}$ recorded at $\theta = -\pi/2$ such that there is no load due to gravity along the joint regardless of q_2. At $q_2 = -\pi/2$ on curve 1, the entire structure of the manipulator is aligned with the axis of the prismatic joint, absorbing the recoil caused due to the quick stepping nature of the actuator, resulting in a maximum value for $\overline{\gamma}_{3+}$. The result from curve 1 is converted into an efficiency factor as:

$$\eta_i(q_2) = 1 - b_i|\cos q_2| \tag{3.2}$$

Joint 3 has a maximum stepping efficiency of 1 at $q_2 = -\pi/2$. The reduced step size (i.e., the reduction in stepping efficiency) at values of q_2 other than $-\pi/2$ is likely due to the component of the recoil force of the actuator acting perpendicular to the link connecting joint 1 to joint 2 causing a small deflection in the link (which is not infinitely rigid). This effect is captured by the $|\cos(q_2)|$ term in $\eta_i(q_2)$. The free parameter b_i captures the loss of

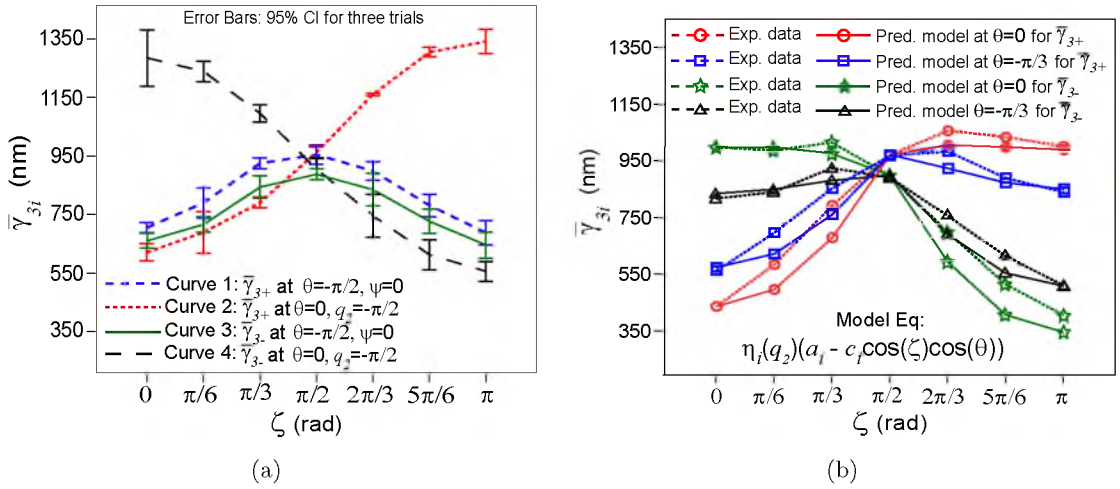

Figure 3.4. (a) Experimental data for the step size of the prismatic joint ($\overline{\gamma}_{3i}$) as a function of ζ, plotted at $\theta = 0$ and $-\pi/2$, with data recorded on three different days. (b) Model equation fitted to experimental data for a single day (Day 1) at $\theta = 0$ and $-\pi/3$, with $\psi = 0$. Calibrated parameter values of $a_+ = 972$, $b_+ = 0.27$, $c_+ = 372$, $a_- = 899$, $b_- = 0.25$, and $c_- = -436$ were found using the three calibration configurations described in the text.

stepping efficiency when the prismatic joint is fully perpendicular to the maximum-efficiency configuration.

To isolate the effect of gravity without any loss of stepping efficiency due to recoil, q_2 is fixed at $-\pi/2$ such that the manipulator arm is always outstretched, and the gravitational load is changed by varying ψ; results of this experiment are shown by curve 2, which is the pure effect of gravity on $\overline{\gamma}_{3+}$. Results for $\overline{\gamma}_{3-}$ are similar to $\overline{\gamma}_{3+}$, but mirrored about $\zeta = \pi/2$ as can be been from curves 3 and 4 in Fig. 3.4a, indicating that moving joint 3 outward with $\zeta = 0$ is equivalent to moving joint 3 inward at $\zeta = \pi$.

We hypothesized a model that combines the information in curves 1 and 2 as:

$$\overline{\gamma}_{3i} = \eta_i(q_2)(a_i - c_i\cos(\zeta)\cos(\theta)) \tag{3.3}$$

The model has six actuator-dependent parameters ($\alpha_3 = \{a_+, a_-, b_+, b_-, c_+, c_-\}$) that can be identified by measuring $\overline{\gamma}_{3+}$ and $\overline{\gamma}_{3-}$ at the three different configurations: $(q_2, \theta, \psi) = (-\pi/2, 0, 0)$, $(0, -\pi/2, 0)$, and $(0, 0, 0)$. This process of finding the free parameters for the prismatic joint is explained in Section 3.3.3. The parameter a_i represents the basic step size of the joint when no gravitational load or recoil inefficiency is acting on the joint, measured at $(-\pi/2, 0, 0)$. It can be seen that curve 1 and curve 2 intersect at the value of a_i. The term $c_i\cos(\zeta)\cos(\theta)$ is a function of the component of the gravitational load due to the

weight of the distal link acting along the axis of the joint. The parameter b_i was defined above.

3.3.3 Calibration procedure for a prismatic joint

The step size model for the prismatic joint as described in Eq. 3.3 has six unknown parameters that can be calibrated for by taking six measurements of $\overline{\gamma}_{3i}$ as shown in Fig. 3.5. For simplicity, the average step size at a known configuration of q_2, θ, and ψ is denoted by $\overline{\gamma}_{3i(q_2,\theta,\psi)}$. The following procedure is used to identify the six free parameters $\alpha_3 = \{a_+, a_-, b_+, b_-, c_+, c_-\}$ of the prismatic joint:

1. First, $\overline{\gamma}_{3+(-\pi/2,0,0)}$ and $\overline{\gamma}_{3-(-\pi/2,0,0)}$ are measured at $(q_2, \theta, \psi) = (-\pi/2, 0, 0)$ and by substituting in Eq. 3.3, we find parameter a_i of the model by the following relation:

$$a_i = \overline{\gamma}_{3i(-\pi/2,0,0)} \tag{3.4}$$

2. Next, $\overline{\gamma}_{3+(0,-\pi/2,0)}$ and $\overline{\gamma}_{3-(0,-\pi/2,0)}$ are measured at $(q_2, \theta, \psi) = (0, -\pi/2, 0)$ and using Eq. 3.3 and the calculated value of a_i, we find parameter b_i using the following relation:

$$b_i = 1 - \frac{\overline{\gamma}_{3i(0,-\pi/2,0)}}{a_i} \tag{3.5}$$

3. Finally, $\overline{\gamma}_{3+(0,0,0)}$ and $\overline{\gamma}_{3-(0,0,0)}$ are measured at $(q_2, \theta, \psi) = (0, 0, 0)$, and by substituting these values in Eq. 3.3 along with a_i and b_i, we find parameter c_i using the following relation:

$$c_i = a_i - \frac{\overline{\gamma}_{3i(0,0,0)}}{1 - b_i} \tag{3.6}$$

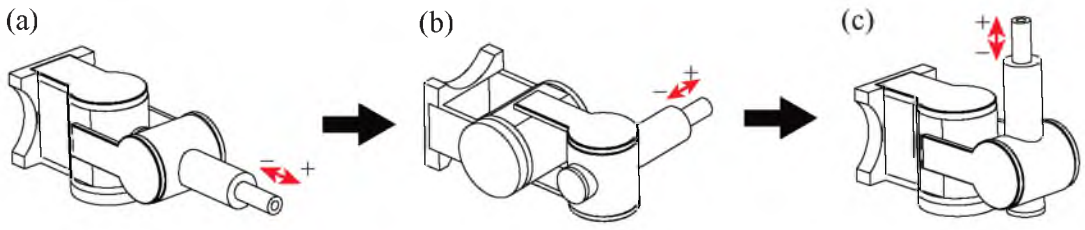

Figure 3.5. Calibrating configurations (in sequence) for identifying the six unknown parameters of the model of the prismatic joint (joint 3). (a) a_i is calculated by measuring $\overline{\gamma}_{3i}$ at (q_2, θ, ψ) = (-π/2,0,0), (b) b_i is calculated using a_i calculated in the previous step and $\overline{\gamma}_{3i}$ at (q_2, θ, ψ)= (0,-π/2,0), and (c) c_i is calculated using the values of a_i and b_i above, and $\overline{\gamma}_{3i}$ at (q_2, θ, ψ)= (0,0,0).

The order of the three steps above, which correspond to steps (a), (b), and (c), respectively, does not have to be carried out in any specific order. In practice, it may be more efficient to conduct the calibration in a different order that requires less joint movements (e.g., (b), (c), (a)).

Fig. 3.4b shows the model plotted against experimental data for a single day at $\theta = 0$ and $-\pi/3$ with ψ fixed at 0. The value of $\theta = -\pi/3$ is not included as one of the calibration configurations mentioned above, yet the model captures the step size of the joint as a function of the configuration. We observe similar results in other configurations. Thus, the calibrated parameters can completely characterize the effect of the load due to gravity on the prismatic joint in any arbitrary configuration of the manipulator.

3.3.4 Modeling of a rotary joint

Two experiments were performed to study the effect of gravitational loads on the rotary joint 2 (in an effort to study static loading in general). In experiment 1, θ is kept at $-\pi/2$ such that there is no load due to gravity on the joint, in an attempt to verify that the joint has a consistent behavior throughout its range of motion if other factors are controlled. Variation in $\overline{\gamma}_{2i}$ is studied in different sub-ranges of q_2, for $q_3 = 0\,\text{mm}$ and $12\,\text{mm}$. From the results of experiment 1, it is safe to conclude that the step size of the rotary joint is relatively constant throughout its range of motion when no load due to gravity is acting on the joint, since the variation in step size for different values of q_2 in this configuration is found to be less than $\pm 2\%$, with no discernible trend in the data. Fig. 3.6 shows the experimental results for experiment 2 in which θ is kept at zero such that there is load due to gravity on the joint; here the gravitational load on joint 2 is a function of its own position q_2.

The model for static loading on the rotary joint is derived based on the physics that, if $\theta = 0$, the torque on joint 2 is related to gravitational loads as $\tau_2 \propto g\sin(q_2)$, where g is the acceleration due to gravity; the constant of proportionality is related to the mass and lengths of the distal links, which are unknown to us. The empirical model to predict the step size for the rotary joint is formulated as:

$$\overline{\gamma}_{2i} \;=\; \overline{\gamma}_{2i,\theta=\pm\pi/2} + d_i \sin(\zeta) \tag{3.7}$$

where $\overline{\gamma}_{2i,\theta=\pm\pi/2}$ denotes the direction-dependent step size of the rotary joint when there is no effect of gravity on the link (i.e., at $\theta = \pm\pi/2$), d_i is a free parameter that denotes the maximum increase in step size over the baseline step size $\overline{\gamma}_{2i,\theta=\pm\pi/2}$, and $\zeta = \psi - q_2$ as described in Fig. 3.2. We assume that the step size at $\theta = -\pi/2$ and $\theta = \pi/2$ would be

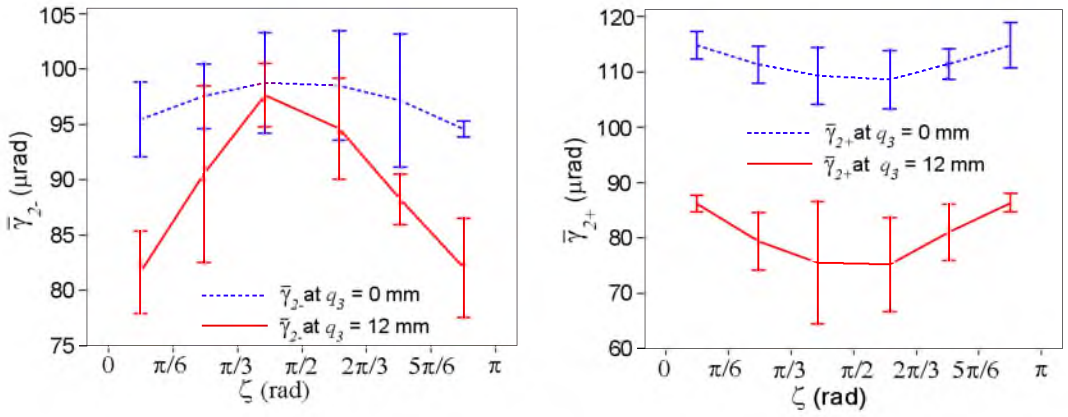

(a) (b)

Figure 3.6. Step size (a) $\overline{\gamma}_{2-}$ and (b) $\overline{\gamma}_{2+}$ as a function of ζ at $q_3 = 0$ and 12 mm, $\psi = 0$, and $\theta = 0$. $\overline{\gamma}_{2i}$ is recorded for intervals of $\pi/6$ from $-\pi/6$ to $7\pi/6$ and is plotted at the midpoint of each interval as explained in Section 4.3.

equal to the step size at $q_2 = 0$ and $q_2 = -\pi$ when $\psi = \theta = 0$, since there is no torque due to gravity on the joint in any of these cases.

It can be seen that the nature of step size in the positive direction is an inverted form of its nature in the negative direction. This is attributed to the fact that the load due to gravity acts against the direction of motion of the joint in the positive direction, and with it in the negative direction. Hence, the step size obtained in the positive direction, $\overline{\gamma}_{2+}$, will be less than that obtained at $\theta = -\pi/2$ where no gravitation load is acting on the joint. The opposite holds true for the step size in negative direction, $\overline{\gamma}_{2-}$. In other words, downward steps are bigger that horizontal steps, which in turn are bigger than upward steps, as we would expect.

If the manipulator were to be tilted by an angle $\theta \neq 0$, then the torque due to gravity on joint 2 would become proportional to the cosine of the gravitational component, such that the model of Eq. 3.7 should be modified as:

$$\overline{\gamma}_{2i} \quad = \quad \overline{\gamma}_{2i,\theta=\pm\pi/2} + d_i \sin(\zeta)\cos(\theta) \tag{3.8}$$

3.3.5 Calibration procedure for a rotary joint

Fig. 3.7 shows the calibration sequence for rotary joint 2, which gives us values for the joint-specific parameters, d_i and $\overline{\gamma}_{2i,\theta=\pm\pi/2}$, for the rotary joint in the positive and negative directions. For simplicity, the average step size at a known configuration of q_3, θ, and ψ is denoted by $\overline{\gamma}_{2(q_3,\theta,\psi)}$ unless otherwise mentioned. The following procedure is followed to obtain the free parameter:

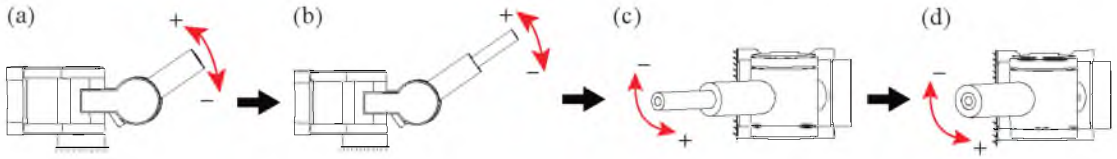

Figure 3.7. Calibrating configurations (in sequence) for identifying the six unknown parameters of the model of the rotary joint 2. q_2 is driven across its full range from $\pi/6$ to -$7\pi/6$ in the negative and positive directions at (a) $q_3 = 0\,\text{mm}$, $\theta = 0$, and $\psi = 0$; (b) $q_3 = 12\,\text{mm}$, $\theta = 0$, and $\psi = 0$; (c) $q_3 = 12\,\text{mm}$, $\theta = -\pi/2$, and $\psi = 0$; and (d) $q_3 = 0\,\text{mm}$, $\theta = -\pi/2$, and $\psi = 0$.

1. $\overline{\gamma}_{2-(0,0,0)}$ and $\overline{\gamma}_{2+(0,0,0)}$ are measured by driving joint 2 across its range from $q_2 = \pi/6$ to $-7\pi/6$ in the negative direction and then in the positive direction at $(q_3, \theta, \psi) = (0, 0, 0)$.

2. The prismatic joint is then fully extended. $\overline{\gamma}_{2-(12,0,0)}$ and $\overline{\gamma}_{2+(12,0,0)}$ are measured by driving joint 2 across its range from $q_2 = \pi/6$ to $-7\pi/6$ in the negative direction and then in the positive direction at $(q_3, \theta, \psi) = (12\,\text{mm}, 0, 0)$.

3. The manipulator is then tilted by setting $\theta = -\pi/2$ such that there is no gravitational torque on joint 2. $\overline{\gamma}_{2-(12,-\pi/2,0)}$ and $\overline{\gamma}_{2+(12,-\pi/2,0)}$ are measured by driving joint 2 across its range from $q_2 = \pi/6$ to $-7\pi/6$ in the negative direction and then in the positive direction at $(q_3, \theta, \psi) = (12\,\text{mm}, -\pi/2, 0)$.

4. The prismatic joint is then fully retracted. $\overline{\gamma}_{2-(12,-\pi/2,0)}$ and $\overline{\gamma}_{2+(12,-\pi/2,0)}$ are measured by driving joint 2 across its range from $q_2 = \pi/6$ to $-7\pi/6$ in the negative direction and then in the positive direction at $(q_3, \theta, \psi) = (0\,\text{mm}, -\pi/2, 0)$.

Since γ_2 is a function of q_2 at each instant, it not a trivial task to calculate the parameter d_i from Eq. 3.8 by using the average step size values ($\overline{\gamma}_{2i}$) that are available to us based on the entire range of motion. A simulation of the model shown in Eq. 3.8 was implemented wherein a number of different values of the free parameters $\overline{\gamma}_{2i,\theta=-\pi/2}$ and d_i were given to the simulation as inputs, and the simulation returns the step size at each instant and the total number of steps required to move through the joint's entire range. The total number of steps obtained is then used to calculate the simulated average step size $\overline{\gamma}_{2i,\theta=0}$.

Fig. 3.8 shows the simulation results obtained for the rotary joint after stepping q_2 through its full range of motion from $\pi/6$ to $-7\pi/6$ for fixed arbitrary (typical) values of $\overline{\gamma}_{2i,\theta=-\pi/2}$ and d_i. The figure shows the dependence of step size on the current configuration.

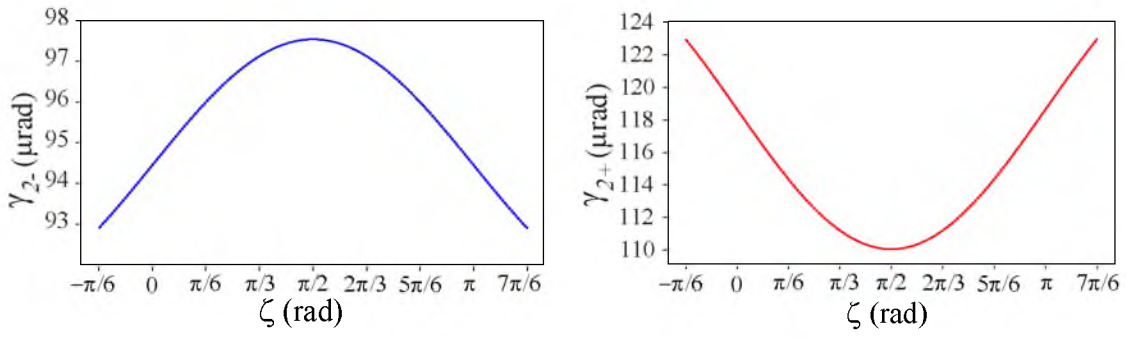

(a) (b)

Figure 3.8. Simulated model of the step size of joint 2 in (a) the negative direction, and in (b) the positive direction. The values of $\overline{\gamma}_{2,\theta=0}$ and $\overline{\gamma}_{2,\theta=-\pi/2}$ are fixed, and θ was kept at zero in simulation. The nature of data obtained in simulation agrees with experimental results shown in Fig. 3.6.

This validates our model of the rotary joint 2 with data observed in experiments (Fig. 3.6). It was found that the difference between the two average step size values $\overline{\gamma}_{2i,\theta=0}$ and $\overline{\gamma}_{2i,\theta=-\pi/2}$ has a quadratic relation with the free parameter d_i as shown in Fig. 3.9. Irrespective of the *individual* values of $\overline{\gamma}_{2i,\theta=0}$ and $\overline{\gamma}_{2i,\theta=-\pi/2}$, the free parameter value d_i remains the same (difference of less than 1 μrad) for the same *difference* between the two step size values. The simulation was performed such that the range of values for $\overline{\gamma}_{2i,\theta=0} - \overline{\gamma}_{2i,\theta=-\pi/2}$ obtained in simulation was from $-9.2\,\mu$rad to $9.2\,\mu$rad, because this was the range of $\overline{\gamma}_{2i,\theta=0} - \overline{\gamma}_{2i,\theta=-\pi/2}$ observed in experiments. A relation for computing d_i was formulated by fitting the simulation results obtained to a quadratic function as shown in Fig. 3.9. The equation formulated using nonlinear least-squares regression is:

$$\begin{aligned} d_i &= 3.41(\overline{\gamma}_{2i,\theta=0} - \overline{\gamma}_{2i,\theta=-\pi/2})^2 + 0.025(\overline{\gamma}_{2i,\theta=0} - \overline{\gamma}_{2i,\theta=-\pi/2}) \\ &\quad +6.42 \times 10^{-7} \end{aligned} \tag{3.9}$$

From Fig. 3.6, we see that $\overline{\gamma}_{2i,\theta=-\pi/2}$ and d_i are a function of q_3, as q_3 changes the inertial load on joint 2. Different values of d_i can be calculated when $q_3 = 0$ and 12 mm using Eq. 3.9, and the effect of changing q_3 is reflected in the values of $\overline{\gamma}_{2i,\theta=0}$ and $\overline{\gamma}_{2i,\theta=-\pi/2}$. The relation between d_i and q_3 cannot be derived with just two data points, and this change in step size due to inertial loading will be studied in the future, but we find a simple linear interpolation provides accurate results.

Fig. 3.10a-d shows the predicted model for γ_{2i} after computing d_i via calibration against experimental data collected on a single day with $q_3 = 0$ and 12 mm. Fig. 3.10e-f shows

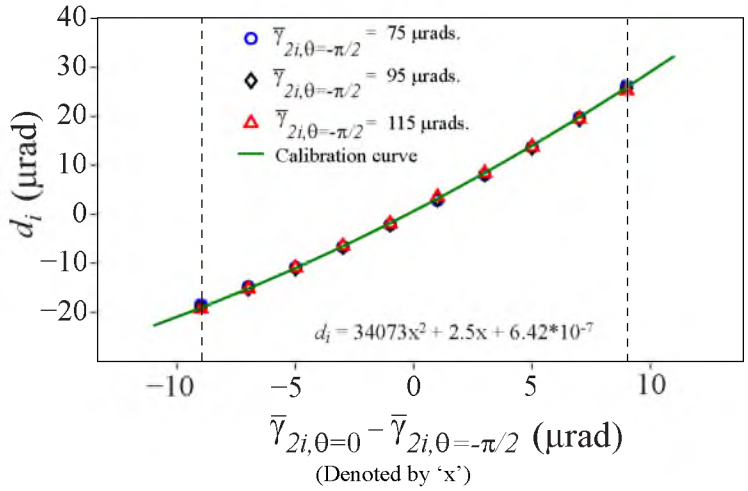

Figure 3.9. Variation of the free parameter d_i with respect to change in difference between $\overline{\gamma}_{2i,\theta=0}$ and $\overline{\gamma}_{2i,\theta=-\pi/2}$ at different values of $\overline{\gamma}_{2i,\theta=-\pi/2}$. The vertical dash lines represent the range of this difference as observed in experiments.

the data collected at $\theta = -\pi/4$ which is used to test the validity of the model for $\theta \neq 0$. The predicted models obtained after calibration are found to be accurate to within 1 μrad ($\pm 2\%$). Thus, the free parameters for the rotary joint can be calibrated for by using eight $\overline{\gamma}_{2i}$ measurements.

3.4 Experiments

The experiments in this paper were designed to isolate and study the effect of static loads on the rotary and prismatic joints of a Kleindiek MM3A. The gravitational load acting on the prismatic joint (joint 3) along the direction of its motion can be described by the angles q_2, θ, and ψ (Fig. 3.2). To study the effect of gravity on the prismatic joint, data was recorded in two different experiments. For each value of q_2, θ, and ψ, $\overline{\gamma}_{3+}$ was first recorded followed by $\overline{\gamma}_{3-}$. In experiment 1, $\overline{\gamma}_{3+}$ and $\overline{\gamma}_{3-}$ were recorded at different values of q_2 and θ in the range of 0 to π and 0 to $-\pi/2$, respectively, in increments of $\pi/6$ with ψ fixed at 0. For each value of q_2, data was recorded for different values of θ before moving on to the next value of q_2. In experiment 2, q_2 was fixed at $-\pi/2$ (outstretched) and the gravitational load was varied by changing ψ, with $\theta = 0$. $\overline{\gamma}_{3+}$ and $\overline{\gamma}_{3-}$ were recorded for one condition in experiment 1 followed by the corresponding condition in experiment 2, before recording data for the next condition in both experiments. This distributes any drift in $\overline{\gamma}_{3+}$ and $\overline{\gamma}_{3-}$ due to time equally in both experiments. One trial for each condition in both experiments was taken per day for three consecutive days to take into account the effect of unmodeled

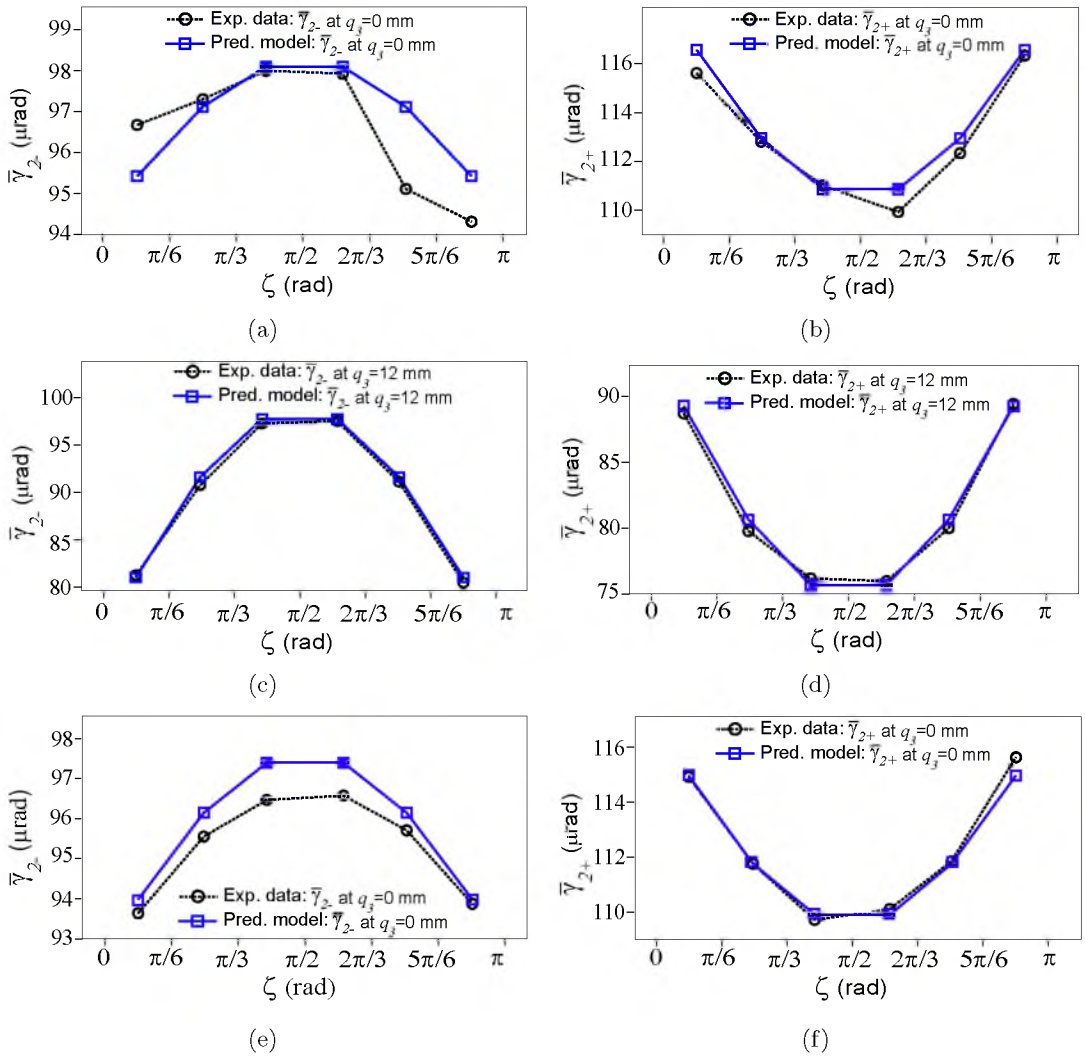

Figure 3.10. (a) Model equation fitted to experimental data taken on a single day for $\overline{\gamma}_{2i}$ at (a) $q_3 = 0\,\text{mm}$, $\theta = 0$, $\psi = 0$ in the negative direction, with d_-=3.83 μrad (b) $q_3 = 0\,\text{mm}$, $\theta = 0$, $\psi = 0$ the in positive direction, with d_+=-8.15 μrad (c) $q_3 = 12\,\text{mm}$, $\theta = 0$, $\psi = 0$ in the negative direction, with d_-=23.94 μrad(d) $q_3 = 12\,\text{mm}$, $\theta = 0$, $\psi = 0$ in the positive direction, with d_+=-19.40 μrad (e) $q_3 = 0\,\text{mm}$, $\theta = -\pi/4$, $\psi = 0$ in the negative direction, with d_-=6.91 μrad (f) $q_3 = 0\,\text{mm}$, $\theta = -\pi/4$, $\psi = 0$ in the positive direction, with d_+=-10.24 μrad.

changes in environmental conditions. Curves 1 and 3 in Fig. 3.4a are obtained from $\overline{\gamma}_{3+}$ and $\overline{\gamma}_{3-}$, respectively, recorded in experiment 1 using the values when $\theta = -\pi/2$, for all three days. Curves 2 and 4 are obtained from $\overline{\gamma}_{3+}$ and $\overline{\gamma}_{3-}$, respectively, recorded in experiment 2. Fig. 3.4b shows $\overline{\gamma}_{3+}$ and $\overline{\gamma}_{3-}$for experiment 1 recorded on Day 1 when $\theta = 0$ and $-\pi/3$. Data from experiments 1 and 2 performed on the same day were used to derive the model parameters shown in Fig. 3.4b.

For modeling a rotary joint, two experiments were performed on joint 2. Initially, $\overline{\gamma}_{2+}$ and $\overline{\gamma}_{2-}$ was measured for the entire range of motion for the joint with $q_3 = 0\,\text{mm}$ and $12\,\text{mm}$. Using a custom-made fixture, joint 2 was then moved in intervals of $\pi/6$ for q_2 from 0 to π and $\overline{\gamma}_{2i}$ was calculated for each interval. The average step size of each interval is assumed to be the step size at the midpoint of the interval as shown in Fig. 3.6. This allows us to study the variation in $\overline{\gamma}_{2i}$ as a function of q_2. $\overline{\gamma}_{2i}$ was recorded in both negative ($\overline{\gamma}_{2-}$) and positive ($\overline{\gamma}_{2+}$) directions. In experiment 1, the mentioned sequence of collecting data was performed at $\theta = -\pi/2$. When $\theta = -\pi/2$, there is no torque due to gravity on the rotary joint, and the step size observed is purely due to the inertial load on the joint and the inherent properties of the actuator. In experiment 2, θ is kept at zero. A gravitational torque is present on the rotary joint, and the step size obtained is influenced by gravitational loading on the joint. One set of data for both experiments was recorded on three different days. Fig. 3.6 shows the results for $\overline{\gamma}_{2i}$ in experiment 2 for all three days, with $\theta = 0$. Fig. 3.10a-d shows the data for $\overline{\gamma}_{2i}$ from experiment 2 for a single day with the predicted model fitted to the experimental data. An additional set of data was recorded at $\theta = -\pi/4$ to check the validity of the model described in Eq. 3.8, the results of which are shown in Fig. 3.10e-f.

3.5 Main Experimental Insights

From the experiments performed in this paper, it was concluded that the step size of a piezoelectric stick-slip actuator can be modeled as having two summed components—a baseline step size that occurs when there is no static load acting on the joint, and a positive/negative contribution due to any static load acting on the joint—and that this two-component step size must be modified to account for the manipulator being in a configuration in which its compliance decreases the efficiency of the stick-slip movement.

Models relating the step size to the static loads were developed for a prismatic (joint 3) and a rotary joint (joint 2) of the Kleindiek MM3A. The actuator-specific parameters of the model can be calibrated for by taking 14 measurements of the average step size (6 for the prismatic joint and 8 for the rotary joint) in specific configurations of the manipulator. The models can accurately predict the step size of the joints at a given manipulator configuration. Kleindiek does not provide specifications for step size of the joints of the MM3A, so we compare the accuracy of our model to a simpler constant-step-size model when there is no static load acting on the joints, i.e., $\overline{\gamma}_{3i}$ at (q_2, θ, ψ)=$(-\pi/2, 0, 0)$ for the prismatic joint, and $\overline{\gamma}_{2i}$ at (q_3, θ, ψ)=(0,0,0) for the rotary joint. The maximum error in the developed model is

approximately 15% for the prismatic joint, and 2% for the rotary joint, as compared to 40% and 7% for the prismatic and rotary joints, respectively, when using the constant-step-size model. Changes in environmental conditions have an effect on the parameters of the model; consequently, the model for the joint parameters should be recalibrated each day.

Fig. 3.6 shows that there is a significant effect of the joint 3 variable q_3 on the step size of the rotary joint 2. Also, $\overline{\gamma}_{2i,\theta=-\pi/2}$ and d_i are functions of q_3. This is expected, as a change in q_3 will lead to a change in inertial load on joint 2 and a change in the step size of joint 2. The effect of inertial loads on the step size is not addressed herein and will be studied in the future.

Joint 1 is another rotary joint with the same range as joint 2 and having the same properties except for the change in static load value. Hence, the model and calibration routine for joint 2 can be extended to joint 1. The only difference in the calibration routine would be that at $\theta = 0$ there is no effect of gravity on joint 1, while at $\theta = -\pi/2$ the gravity is perpendicular to the joint axis. So, in short, the definition of the terms, $\overline{\gamma}_{2i,\theta=0}$ and $\overline{\gamma}_{2i,\theta=-\pi/2}$ would be interchanged.

Models developed in this paper for the step size of piezoelectric stick-slip actuators are not perfect. Hence, when these models are used in teleoperation algorithms like the one proposed in [33], there will be drift in the position of the end-effector due to the accumulation of error in the model. However, this problem can be overcome as recently developed piezoelectric actuators have sensors with micro- and nanometer resolution [6]. This sensor feedback could be used to remove drift in the position, but the models of step size will still be necessary to command multiple steps in a single command to the joint before sensor feedback is obtained.

The experiments in this paper were performed in a room without tight climate control. When using the manipulator inside an SEM, frequent recalibration might not be necessary, since the manipulator will be in a vacuum. However, the audio limit switch used to detect end of travel will not work in a vacuum, and will need to be replaced by an accelerometer-based sensor mounted on the manipulator (when sensor feedback is not available) to detect the end of travel during calibration. The experiments in this paper were performed using a Kliendiek MM3A, but we expect the results to generalize to other similar devices that utilize peizoelectric stick-slip actuators.

CHAPTER 4

A COMPACT TELEMANIPULATED RETINAL-SURGERY SYSTEM THAT USES COMMERCIALLY AVAILABLE INSTRUMENTS WITH A QUICK-CHANGE ADAPTER

4.1 Introduction

Retinal microsurgery procedures are at the limits of human ability [37–41]. An error of only a few micrometers can cause the instrument to exert damaging force on the retina, causing localized loss of vision. The forces experienced during retinal surgeries are below what surgeons can feel ($< 7\,\mathrm{mN}$), so surgeons must rely on visual feedback only [37, 42, 43]. The surgeon must pivot the instruments about the scleral trocars (Fig. 4.1), limiting dexterity, and must use the instruments to manipulate the eye to provide better imaging through the surgical microscope. Patient movement due to breathing must be accounted for by the surgeon, and in addition, among patients who snore under monitored anesthesia ($\approx$16% of cases [44]), half have sudden head movements during surgery, leading to a high risk of complications.

One of the most difficult retinal-surgery procedures involves the peeling of membranes on the retina. Epiretinal membrane (ERM) comprises sheets of fibrous tissue up to 61-μm-thick [45] that distort macular anatomy and disturb vision after posterior vitreous detachment or retinal tears, and the inner limiting membrane (ILM) is a naturally occurring 0.15–4-μm-thick membrane [46] that can contract with age and generate macular holes. To improve vision in affected eyes, ERM and ILM are peeled by inserting delicate instruments inside the eye (Fig. 4.1). Membrane peeling is a delicate procedure, and complications occur frequently in the form of intraoperative hemorrhage, retinal detachment during or after surgery, infection after surgery, regrowth of epiretinal membrane, and increased rate of

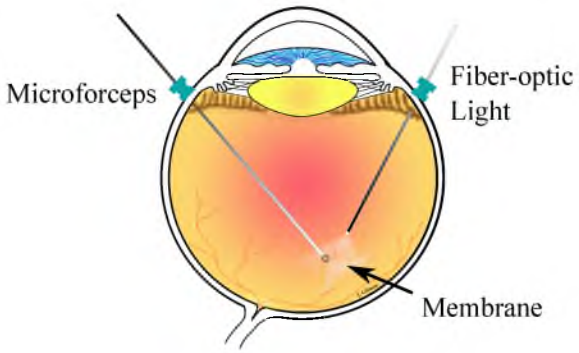

Figure 4.1. Instruments inserted through trocars in the pars plana region of the sclera are used to perform delicate scraping and peeling motions to peel membranes on the retina. Image courtesy James Gilman, CRA, FOPS.

cataract development [47]. In some cases, a second surgery is required to remove fragments of the ERM/ILM left behind. Other experimental procedures inside the eye like retinal vein cannulation involve delivering drugs to retinal veins that measure less than 100 μm in diameter, whereas physiological tremor in the human hand during retinal surgery was measured to be 100 μm [39].

There are opportunities for significant improvement in retinal-surgery procedures in terms of safety and consistency of outcomes. As our population ages over coming years, the number of surgical procedures will likely increase relative to the number of surgeons available [48]. Robot-assisted retinal surgery will enable surgeons to improve surgical efficiency by enabling them to overcome their human limitations, and to extend their working life and capitalize on their experience even after their manual abilities have diminished.

Prior research in robot-assisted retinal surgery has resulted in the development of telemanipulated systems [13, 15, 49–54] and cooperative manipulators [55, 56]. Robotic systems for retinal surgery have typically been relatively large and stiff, and thus table-mounted. In related work, active hand-held instruments primarily aimed at tremor reduction, with no ability to affect the "DC" system response, have been shown to reduce RMS tremor to 10 μm–60 μm [57–60]. Since the human hand is the source of tremor during microsurgery, telemanipulated systems, which eliminate direct contact between the surgeon and the instrument, seem particularly promising. Most prior systems leave the retina at risk in the event of sudden head movement, and rhythmic head movements would need to be actively compensated. Notable exceptions are the TU Munich [13] and Columbia/Vanderbilt systems [51], which are designed to be head-mountable. The TU Munich system [13] has been demonstrated to be head-mountable.

The specifications of retinal surgery are difficult to achieve using traditional mechatronic components (e.g., motors, gears), while maintaining a small form factor. In this paper, we present a manipulator for retinal surgery that utilizes piezoelectric stick-slip actuators, which were designed specifically for micromanipulation (this same style of actuator was used by Nasseri et al. [13]). Piezoelectric stick-slip actuators have a high resolution ($< 1\,\text{nm}$) and a high dynamic displacement range (cm–nm) [1]. During normal operation, these actuators behave like admittance-type devices (i.e., they are stiff, they passively remain in place until actively commanded to move, and they are stationary in the event of power loss), yet they can be back-driven with a gentle force by a human hand (or any other applied force) with no damage to the device, which is significantly different behavior than a traditional admittance-type devices. The manipulator presented in this paper has submicron resolution and is small and light enough to be head-mounted (although that is not demonstrated in this paper). A principal contribution of this work is an instrument adapter that enables the use of the full range of unmodified commercially available instruments, including instruments that require some form of actuation, such as microforceps and scissors, and nonactuated instruments, such as a diamond-dusted scraper (DDS), a vitrector, and a fiber-optic light. The instrument adapter also enables quick change of instruments, which is an important requirement in retinal surgery that has rarely been demonstrated in prior telemanipulated systems. We also describe a custom master input device that is inspired by an Alcon disposable microforceps, which has been designed for superior ergonomics compared to traditional pinch-grip devices. Our complete system is shown in Fig. 4.2. Finally, we include experimental results comparing manual membrane peeling to telemanipulated membrane peeling in a force-sensitive phantom eye. This paper is an extended treatment of an earlier work [61].

4.2 System Design

4.2.1 6-DOF manipulator

A six-degree-of-freedom (6-DOF) manipulator was designed using off-the-shelf piezoelectric stick-slip actuators from SmarAct GmbH (Fig. 4.2a). It comprises a 3-DOF translation stage and a 3-DOF spherical wrist, which enables the manipulator to position the instrument inside a 20-mm-diameter spherical-sectin bowl centered on the retina with a virtual remote center on the surface of the eye (a sphere of 25.4-mm diameter). The linear stages (q_1, q_2, and q_3) have a range of 40 mm with a closed-loop resolution of 100 nm. q_1 utilizes a parallel-rail structure, in which one rail is a stick-slip actuator and the other is a passive

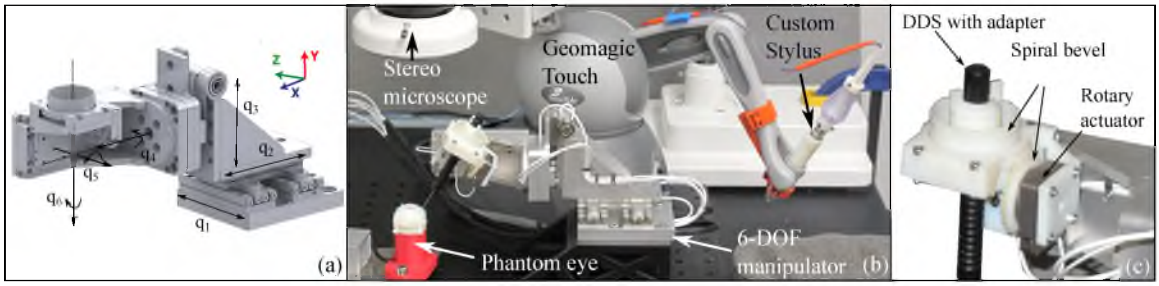

Figure 4.2. Retinal-surgery System. (a) 6-DOF manipulator for retinal surgery. (b) Experimental setup of the retinal-surgery system. The surgeon looks in the phantom eye using a stereo microscope, and telemanipulates the end-effector of the instrument with 4-DOF (3-DOF translation, and rotation of the instrument about its axis) using a Geomagic Touch (located to enable direct access to instruments) with a custom stylus that is constrained to have the same 4-DOF by locking the wrist. (c) Yaw joint of the manipulator, which is responsible for rotation of the instrument about its axis, with an adapter that enables instruments to be attached to the manipulator.

guide. The vertical direction (q_3) includes a constant-force spring to offset the weight of the spherical wrist. The spherical wrist comprises three rotary piezoelectric stick-slip actuators, with a closed-loop resolution of 25 μ° for the roll (q_4) and pitch (q_5) actuators, and with a yaw actuator that enables open-loop rotation about the axis of the instrument (q_6) with a resolution of 3 m°. The positioning precision of the manipulator is measured with joint sensors while performing constrained motion near the retina to be $<1\,\mu$m, and the maximum velocity at the end-effector is 6 mm/s. The positioning precision was verified using a VHX-5000 (Keyence Corp.) microscope. The linear actuators of the manipulator (SmarAct SLC-2460) can be backdriven by applying a force of 5 N, and the roll and pitch rotary actuators (SmarAct SR-4513, SR-2812) can be backdriven by appling torques of 15 N-cm and 6 N-cm, respectively. The maximum force that the linear actuators can apply while in motion is 4 N, and the roll and pitch actuators can apply a torque of 6 N-cm and 3 N-cm, respectively. The manipulator measures $200\times100\times70\,\text{mm}^3$ and weighs 0.8 kg.

The manipulator was manufactured by SmarAct to our specifications, and we further modified the yaw joint of the manipulator such that it can use a wide range of actuated and nonactuated instruments. The modified yaw joint was manufactured using a 3D printer (Objet Eden260). The yaw joint is designed with the yaw actuator's axis orthogonal to the instrument's axis, and the rotary motion to the instrument is transmitted using spiral bevel gears. The spiral bevel gear includes a 23-mm aperture and internal threads that enable instruments to be attached to the manipulator. The aperture size was selected such that disposable instruments of a wide range of form factors can be used with the manipulator.

From our observations in the operating room, we found that during retinal surgery, on average the surgeon changes the instrument every two minutes. It is important that a robotic system for such procedures facilitates the quick change of instruments without disturbing the flow of the procedure, so we designed an adapter that enables the surgeon to change instruments frequently, and enables the use of disposable instruments that require "pinch-grip" actuation such as microforceps and scissors, with this seventh DOF of actuation connected to the instrument rather than to the manipulator. Our mechanism utilizes adapters that are attached to disposable instruments before surgery. The length of each instrument is known, and the distance from the adapter base (see Fig. 4.3f) to the tip of the instrument is kept constant for each instrument. The adapters can be designed such that the shape of the adapters conforms to the shape of a specific instrument (Fig. 4.3c and Fig. 4.3f) maintaining a constant and repeatable distance between the instrument tip and the adapter base; we have implemented a distance of 84.5 mm in our prototype, which is largely governed by the Alcon microforceps (see Fig. 4.3b). The adapter uses threads inspired by Luer fittings and an adapter stop on the manipulator enables the instrument to be attached in the perfect position every time. Once the instruments with the adapters are attached to the manipulator, the end-effector of any instrument will be at the same known location within a small tolerance (80 μm measured using images).

To characterize the instrument change time for our manipulator, we performed a simple experiment with five subjects in which the subjects changed the instrument from a DDS to a microforceps and then back to a DDS (5 trials), at a comfortable speed. The time required to change an instrument was found to be 12.7 s $\pm$ 2.5 s (mean $\pm$ st.dev.). We repeated this simple experiment with the same instruments for a manual surgery, and found an average change time of 8.3 s $\pm$ 1.4 s. With an increase in time of 5 s for every 2 min of surgery (a 4% increase), we conclude that the additional time due to tool change is fairly insignificant. By recording the joint sensor values, we confirmed that there was no motion in the joints while the instrument was being changed. Hence, the instruments can be changed while the end-effector is still positioned inside the eye without a risk of injuring the retina due to unintended motions during instrument change. However, additional methods will have to be used to register the exact location of the trocar on the sclera in this case.

Sterilizability is an important consideration for manipulators used in surgery. Our manipulator is small enough that it is conceivable that the entire manipulator could be gassed or autoclaved between procedures (SmarAct makes autoclavable actuators). Alternatively, all components distal to the rotary actuator shown in Fig. 4.2c (i.e., the 3D-printed

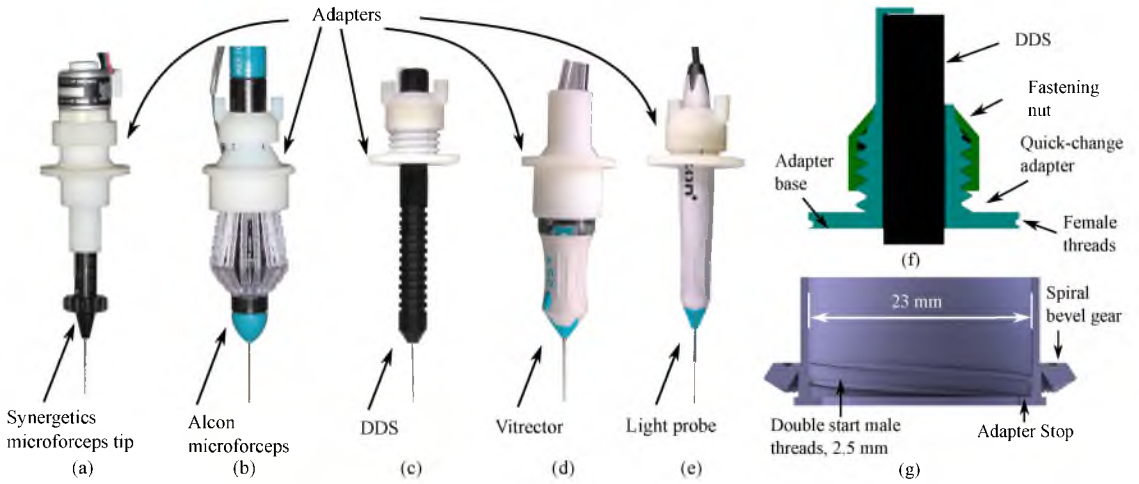

Figure 4.3. Quick-change adapter design. (a)–(e) Disposable retinal-surgery instruments with adapters that enable quick-change mounting to the 6-DOF manipulator. (f) Section view of a quick-change adapter attached to a diamond-dusted scraper (DDS). (g) Section view of the yaw joint to which the instruments with quick-change adapter are attached.

components) could easily be made disposable or removable for autoclaving. This would enable the remainder of the manipulator to be wrapped in sterile draping with a pass through for a rotary actuator's shaft, using a method inspired by that employed by Intuitive Surgical's da Vinci. Finally, we have also verified that surgical draping can be inserted between the quick-change adapter and the spiral gear on the manipulator to which the adapter is attached (Fig. 4.3f and 4.3g), and can be inserted between the linear stepper motor and the disposable microforceps tip (Fig. 4.4a) without affecting operation of the plunger, providing a potential alternate path to sterilization.

4.2.2 Actuation mechanisms for instruments

Two different actuation mechanisms were designed to enable the use of two different families of actuated instruments commonly used in retinal surgery: disposable instrument tips (e.g., Synergetics microforceps tip (Fig. 4.3a)) that are used with reusable handles, and completely disposable instruments (e.g., Alcon microforceps (Fig. 4.3b)).

4.2.2.1 Actuation with stepper motor

For actuating a disposable instrument tip, which requires pressing a plunger on the device, we used a linear stepper motor (LC15, HaydonKerk) with force capability of 5 N (2 N is required to actuate a Synergetics microforceps). The stepper motor is attached to the microforceps tip using an adapter that enables the microforceps to be mounted on the manipulator (Fig. 4.4a). The LC15 has a linear resolution of 2.5 μm, and requires 500

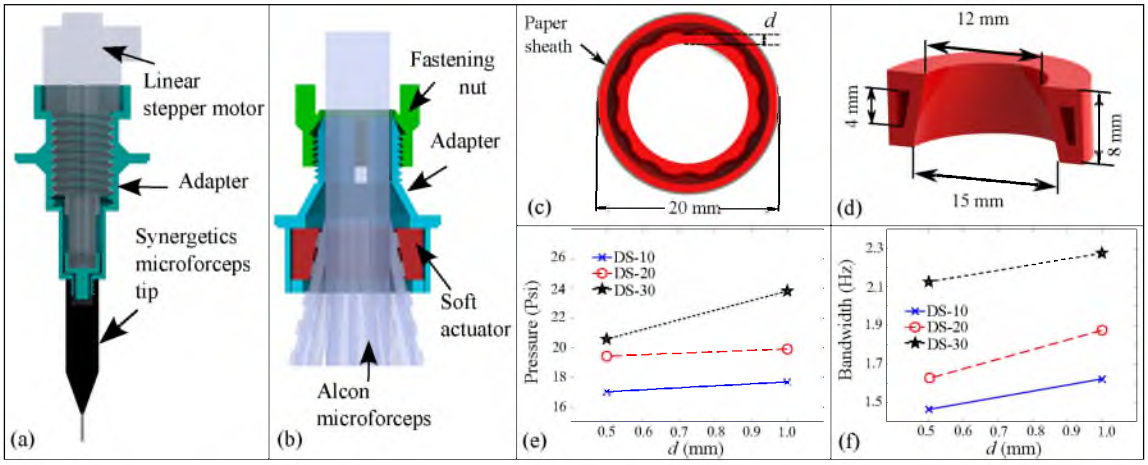

Figure 4.4. Actuation mechanisms for microforceps. (a) Section view of the Synergetics microforceps actuated by a linear stepper motor. (b) Section view of the Alcon microforceps actuated by a soft actuator. (c) Top section view of the soft actuator. The paper sheath on the outer wall and the profile of the inner wall only allow for expansion radially inward. (d) Side section view of the soft actuator. The height of the channel is inversely proportional to the maximum pressure required for actuation. (e) The maximum pressure required for complete actuation and (f) the bandwidth (for a complete open-close cycle) increases with d and the hardness of the silicone elastomer.

steps (travel of 1.25 mm) for the complete actuation (i.e., fully open to fully closed) of the microforceps. The measured bandwidth for a full open-close cycle of the microforceps with the stepper motor is 2.5 Hz.

4.2.2.2 Actuation with soft actuator

The second actuation mechanism, for use with completely disposable Alcon instruments, uses a soft actuator inspired by a blood-pressure cuff (Fig. 4.4b), which squeezes the ribs on a pinch-grip device when supplied with pressurized air (already available in the operating room). The soft actuator is molded from a silicone elastomer using soft-lithography techniques [62]. 3D-printed molds with inserts are used in a two-step process to fabricate the soft actuator that has a channel for pressurized air, which is then heat cured at 70°C. The inner walls of the soft actuator conform to the shape of the pinch-grip mechanism of an actuated disposable instrument (e.g., forceps). The profile of the inner walls are designed to cause preferential expansion toward the instrument. An outer sheath made of paper is used to mitigate outward expansion of the outer wall. The soft actuators were fabricated with silicone elastomers of three different hardnesses (Dragon Skin 10, 20, and 30, Smooth-on Inc.), and two different values for the inner wall thickness d of 0.5 mm and 1 mm (see Fig. 4.4c). The soft actuator attached to an Alcon forceps weighs 10 g, which is approximately

one third that of the stepper-motor-based forceps.

A PD control system comprising two ON/OFF valves (MHJ series, Festo) and a pressure sensor is implemented to regulate the pressure inside the soft actuator. The controller converts the error in pressure for the soft actuator into a PWM signal that is used to control the valves. Figure 4.4e shows that the maximum pressure required to completely close the forceps increases with the wall thickness and the elastomer hardness. A similar but counter-intuitive result was observed for the bandwidth for a full open-close cycle of the forceps (Fig. 4.4f). The bandwidth increases with an increase in the wall thickness and the elastomer hardness. This can be attributed to a decrease in the deflation time for the actuators when opening the forceps, with an increase in the wall thickness and the elastomer hardness. A version of the controller with a bandwdith of 2 Hz and a resolution of 10 discrete steps between fully open and fully closed forceps was used for experiments in Section 4.3.

4.2.3 Telemanipulation system

A Geomagic Touch (formerly known as the Phantom Omni) is used to telemanipulate the retinal manipulator. The Touch is an inexpensive haptic interface that has 6-DOF motion and sensing but only 3-DOF actuation; the position of the device's wrist can be controlled, but the orientation of the stylus cannot. We use the Touch as our master input device here for expediency; we are not advocating that it is the best device for overall performance.

A master-slave position controller is implemented in which the scaled end-effector position is mapped as a proxy point in the Touch workspace, and a virtual spring-damper is implemented between the proxy and the position of the Touch wrist. The gains were chosen to generate smooth and stable behavior. The scaled position of the Touch wrist (software-adjustable scaling, with a deadband of 200 μm on the master) is given as a position command to the end-effector. A low-level position controller (Section 4.2.3.2) is implemented to servo the end-effector to the desired position. A clutch (foot pedal) is used to engage/disengage the slave manipulator from the master. The remote-center-of-motion (RCM) movement of the instrument about the trocar is handled in software, such that the user directly controls 4-DOF of instrument movement (3-DOF Cartesian position, and rotation of the instrument about its axis). During experiments described in Section 4.3, the instrument tip is inserted into the trocar and the master forceps is squeezed once to register the RCM location ($\vec{x}_{rcm}$) in the manipulator workspace, which is fixed throughout the experiments. As there is an algorithmic singularity at the trocar, a virtual fixture is implemented for stable telemanipulation that constrains the instrument to one-DOF

instrument insertion/retraction when the end-effector is near the trocar. To reduce overall experiment time in our human-subject experiments, the instruments were positioned inside the eye during trials. A virtual fixture is implemented close to the trocar to prevent instabilities due to an algorithmic singularity at the trocar. Orbital manipulation is not implemented here, but nothing about the design of the retinal manipulator precludes it. In a telemanipulation experiment in which we attempted to generate the smallest possible instrument movement (5 trials in each of six cardinal directions), we measured, using joint sensors, a resolution of 18.6 μm $\pm$ 9 μm (mean $\pm$ st.dev.) with 8:1 scaling, and 2.3 μm $\pm$ 1.2 μm with 100:1 scaling; the manipulators inherent resolution is achieved in the limit as scaling is increased.

4.2.3.1 Microforceps stylus for Geomagic Touch

The Geomagic Touch haptic interface is modified with a custom stylus that enables control of actuated instruments on the manipulator (Fig. 4.5). The stylus is built to mimic an Alcon disposable microforceps (see Fig. 4.3b), using components salvaged from its pinch-grip device. The pinch-grip mechanism is attached to a stylus, with the distal end of the pinch-grip mechanism allowed to move along the stylus shaft. A soft-membrane linear potentiometer (ThinPot, Spectra Symbol) is used to measure the movement of the distal end. Rolling-tip set screws at the moving distal end of the mechanism are used to reduce friction and to serve as a wiper for the potentiometer. A spring (6 N/mm) approximately recreates the stiffness of an actual microforceps. The measured position resolution of the distal end of the pinch-grip mechanism is 10 μm for a travel length of 1.25 mm.

Figure 4.5. Modified stylus for the Geomagic Touch. The pinch-grip mechanism from a disposable Alcon microforceps is attached to the stylus shaft, and a spring is used to recreate the stiffness of the microforceps' pinch-grip mechanism. A linear potentiometer is used to measure the squeezing of the pinch-grip mechanism.

4.2.3.2 Low-level position controller

Initial attempts at using the native closed-loop joint controllers provided by SmarAct caused undesirable vibrations at the end-effector that were perceivable while telemanipulating the instrument under a microscope. As a result, we implemented a custom controller that minimizes the vibrations at the end-effector to a level that they are no longer visually perceivable under a microscope.

Algorithm 2 shows the basic steps for the implemented controller that enables our manipulator to perform RCM movements about a point in its workspace $\vec{x}_{rcm}$. The algorithm is called in a continuous loop by the software with a constant sampling time (dt). It takes the desired position commanded by the user ($\vec{x}_d$) and the current joint positions from the joint sensors ($\vec{q}$) as an input, and calculates the integer number of steps required along each joint ($\vec{\delta}$) with the frequency ($\vec{f}_{safe}$) at which the steps should be commanded in each cycle to achieve the desired position. The desired orientation vector for the end-effector is calculated from the RCM point ($\vec{x}_{rcm}$) and the desired position ($\vec{x}_d$), and is converted to a desired orientation matrix (R) using Rodrigues' rotation formula. Inverse kinematics is then used to calculate the desired joint values ($\vec{q}_d$), and subsequently, the change in joint values ($\vec{dq}$) required to achieve $\vec{x}_d$ is calculated. An empirically derived open-loop model of the step size of the joints ($\vec{\gamma}$) is then used to calculate the integer number of steps ($\vec{\delta}$) required along each joint. The step size is a function of the number of steps commanded, the frequency at which the steps are commanded, and the voltage amplitude of each step. To achieve submicron precision, the voltage amplitude for each actuator is reduced by 50% when the required change in joint values (dq_i) is less than the step size of a joint i. This results in a reduced step-size for the actuators.

The frequency at which each actuator should be driven ($\vec{f}_{calc}$) is calculated from $\vec{\delta}$ and

Algorithm 2 Low-level position controller

1: **read** $\vec{x}_d, \vec{q}$
2: $R = \text{calculateOrientation}(\vec{x}_{rcm}, \vec{x}_d)$
3: $\vec{q}_d = \text{inverseKinematics}(\vec{x}_d, R)$
4: $\vec{dq} = \vec{q}_d - \vec{q}$
5: $\vec{\delta} = \text{round}(\vec{dq}/\vec{\gamma})$
6: $\vec{f}_{calc} = k_f \vec{\delta}/dt$
7: $\vec{f}_{safe} = \text{rejectFreq}(\vec{f}_{calc})$
8: **return** $\vec{\delta}, \vec{f}_{safe}$

dt. k_f is an empirically derived constant that is required for stable closed-loop operation. For our manipulator, $k_f = 0.3$. We observed that certain frequencies of operation for the rotary actuators excited the resonant frequencies of the instrument, resulting in undesirable vibrations when starting and stopping motion of the end-effector. We empirically determined the undesirable frequencies by driving the rotary actuators at different frequencies and visually inspecting the vibration of the end-effector. If the calculated frequency ($\vec{f}_{calc}$) was in the range of undesirable frequencies, it was capped to the lowest safe frequency. The range of undesirable frequencies for a DDS and a microforceps were found to be between 100–400 Hz. No perceivable discontinuity in the motion of the end-effector was observed due to this rejection of frequencies. The SmarAct controller unit provides data from position sensors at a maximum rate of 70 Hz, and hence our controller update rate is limited to 70 Hz in this prototype. For membrane peeling during manual surgery, power analysis of the displacement of the instrument at 3 Hz has been found to be one-hundredth of the power at DC [40]. The frequency response of our manipulator for a sinudoid of amplitude 0.5 mm at 3 Hz has an absolute amplitude gain of 0.8. As a result our manipulator is able to track all voluntary movement, and has some inherent tremor reduction since the response of the manipulator is severely attenuated at higher frequencies.

4.2.3.3 Augmented controllers for retinal surgery

During actual surgery, membranes are peeled in a circular path close to the surface of the retina, as slowly as physically possible. Peeling the membrane too fast can result in fragmentation of the membrane and can also lead to retinal tears due to excessive upward forces. Additionally, surgeons have to account for the curvature of the retina when making lateral movements close to the surface of the retina. We implemented two additional telemanipulation controllers, the *variable-speed* controller, which we hypothesized could assist in slow peeling of membranes, and the *virtual-fixture* controller, which we hypothesized could enable safer movement close to the retina. These augemented controllers are added to the *standard* telemanipulation controller already described above. In the variable-speed controller, the speed of the end-effector is reduced by a somewhat-arbitrary factor of 10 if the forceps is closed by more than 10%. The closure of the forceps is taken as an intent of the user to operate on the retina, and our hypothesis is that the slower speed would improve peeling precision and reduce upward peeling forces. In the virtual-fixture controller, a virtual fixture is implemented to attenuate radial velocities toward the retina by 90% when in close proximity to the retina, whereas velocities tangent to or away from the surface

remain unchanged. The virtual fixture is determined using an identification procedure by touching at least four points on the retina with the end-effector, and a spherical surface that best fits the points on the retina is calculated. In clinical practice, touching the retina with instruments might not be feasible. Alternative methods that use force-sensing instruments or an optical coherance tomorgraphy (OCT) probe could be used [63, 64].

4.3 Experiments

4.3.1 Methods

To compare manual vs. telemanipulated retinal surgery (using 8:1 scaling exclusively), we performed experiments with a phantom eye shown in Fig. 4.6. Trocars were inserted into the model eye as would be done in surgery. The anterior (upper portion) of the eye is made of a synthetic rubber (Phake-I, 8 mm-diameter pupil) and approximates the size, shape, and feel of the human eye. The anterior of the eye was attached to a fixture as shown in Fig. 4.6, and inside the fixture, an ATI Nano17-Ti force/torque sensor (noise $<$1 mN) was mounted with a section of a spherical surface that acts as the posterior (retinal) surface of the eye on which surgery will be performed. This mechanical isolation between the anterior and posterior of the eye ensures that only the relatively small instrument-retina interaction forces are measured by the force sensor. The anterior portion of the model eye can rotate on the fixture allowing for minor orbital manipulation, but the posterior surface that is attached to the force sensor remains static.

The retinal surface was prepared with an artificial membrane made of paper (cut to 6-mm-diameter circle, 120 μm thickness), and 10 μl of an eye lubricant gel (GenTeal) was applied to the model retina by using a pipette to achieve adhesion between the model membrane and the model retina. Paper with different strength characteristics can be used to simulate different types of membranes based on their peeling difficulty. We chose a paper membrane that, according to our surgeons, qualitatively approximated the behavior of a real membrane. The low preparation time compared to artificial membranes previously developed in the literature [65] enabled us to keep our experiment time within reasonable limits. To measure the repeatability of our artificial membrane, we performed an experiment where the membrane was peeled at different constant velocities by the manipulator. Fig. 4.6f shows the upward peeling forces (F_y) at different peeling velocities (five trials for each velocity). At velocities below 3 mm/s, the upward peeling force seems to be insensitive to the velocity.

Three vitreoretinal surgeons with varying degrees of surgical experience—20 years (ex-

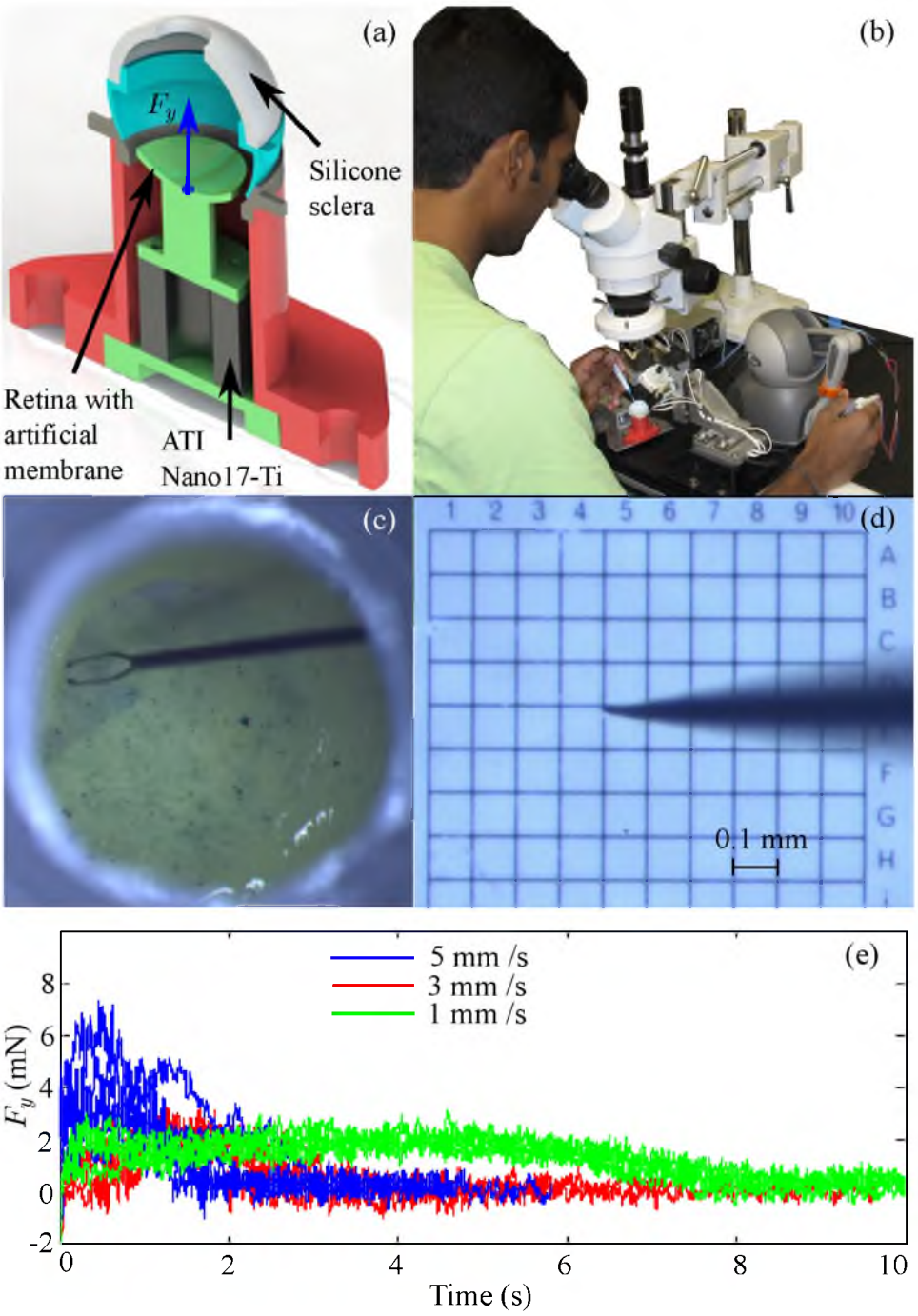

Figure 4.6. Phantom eye setup with artificial membrane used in experiments. (a) Section view of phantom eye used. (b) A user performing telemanipulated surgery on the phantom eye. A fiber-optic light is manipulated manually with the left hand. (c) A paper membrane being peeled by an Alcon microforceps using the retinal manipulator. (d) Snapshot from video demonstration of smooth motion across a 1 mm grid, with each subgrid measuring 100 μm, and each line having a width of approximately 8 μm. (f) Typical upward peeling force for the artificial membrane at different velocities.

pert), 2 years (intermediate), 6 months (novice)—and a graduate student with no experience in actual surgery, performed manual and telemanipulated surgery on the phantom eye setup with an Alcon microforceps and a DDS. The graduate student and expert surgeon are both authors of this paper. All the surgeons had two hours of practice on the telemanipulated system before data were recorded. The graduate student had been using the telemanipulation system for a year. Two experiments were performed by each subject. In Experiment 1, subjects performed manual surgery, and in Experiment 2, the surgery was performed with the telemanipulated system. Each experiment was performed with two different instruments, the DDS and the microforceps, with a single instrument being used in a given trial. With the DDS, the subjects had to scrape at the edge of the membrane for 1 min as they would during an actual surgery, applying delicate but useful forces. With the microforceps, the subjects had to completely peel a membrane off the force-sensing retina, which was visually verified in each trial. The subjects were instructed that applying minimal downward force to the retina was the primary objective, with minimizing completion time as a secondary objective. In Experiment 2, trials were performed for two additional controllers as described in Section 4.2.3.3 along with the standard controller. Three trials were performed in each experiment, for each instrument and controller type to obtain a total of 24 trials for a given day. Experiments were performed on two days (approximately 120 min per day) for a total of six trials per condition, and trials on a given day were randomized for instrument type and controller type (applicable only to Experiment 2). Two subjects (expert and novice) performed Experiment 1 followed by Experiment 2 on the first day, with the order reversed on the second day, and the other subjects (intermediate and graduate student) performed the experiments in a reverse order. A fresh membrane was prepared for each trial.

A third experiment was performed to measure performance in telemanipulated surgery over time, in order to measure learning effects with the robotic system without conflating factors such as switching between robotic and manual surgery. Five new subjects (4 male) with no experience in performing actual surgery performed telemanipulated surgery (standard controller only) with a microforceps to peel the artificial membrane off the force-sensing retina. Subject 1 (a surgical resident) had observed membrane peeling surgery, and the other four subjects had no knowledge about the procedure. Six blocks of five trials each were performed spread across two days (three and three). The subjects were instructed that peeling the membrane while applying minimal downward force to the retina was the primary objective, with minimizing completion time as a secondary objective. After each

block, the experiment conductor analyzed the data and informed the subjects that their performance could be improved by pressing even more gently on the retina, irrespective of how they had actually performed.

Although we do not purport that the experiments described in this pilot study are rigorous enough to make strong claims, we do believe that the results are informative regarding the potential of the telemanipulation system.

4.3.2 Results

To evaluate performance in our experiments, we use the maximum downward force (F_{-y}), completion time (T_c), and the maximum upward force (F_{+y}) in a given trial as independent metrics. During all microforceps experiments, the primary goal for the subjects was to minimize F_{-y}, with minimizing T_c as a secondary objective. The subjects were given no specific instruction regarding the upward peeling force F_{+y}. It should also be noted that the stiffness of the plastic used in our experiments is higher than that of an actual retina, and hence, the forces measured can only be used for comparisons within this study, since small positioning errors can lead to relatively large rises in force.

Fig. 4.7 shows F_{-y}, T_c, and F_{+y} for Experiments 1 and 2. For the trials performed with the microforceps, we observe that all four subjects perform approximately equivalently during manual surgery in terms of downard force F_{-y}, and that the expert and intermediate surgeons (which we will refer to as the *skilled* surgeons) perform substantially better than the other two subjects during manual surgery in terms of time T_c. We also observe there are no noticeable trends in F_{-y} (e.g., learning) from Day 1 to Day 2 for manual surgery, as we would expect; however, there is a reduction in forces for each of the telemanipulation controllers from Day 1 to Day 2 for all subjects except the graduate student, suggesting that there is a learning effect from Day 1 to Day 2 for the other subjects. As a result, for all subsequent analysis, we lump the two days of manual data together for a given subject to increase the power of the statistics. In addition, we lump the two days of manual data for the expert and intermediate surgeons into a single *skilled* manual data set. Table 4.1 shows the results for independent t-tests comparing manual surgery to different controllers in telemanipulated surgery for each subject, and comparing telemanipulated surgery using the various controllers to both within-subject manual surgery and skilled-surgeon manual surgery (i.e., the gold standard). All statistically significant results are presented for $\alpha < 0.05$ unless specified otherwise.

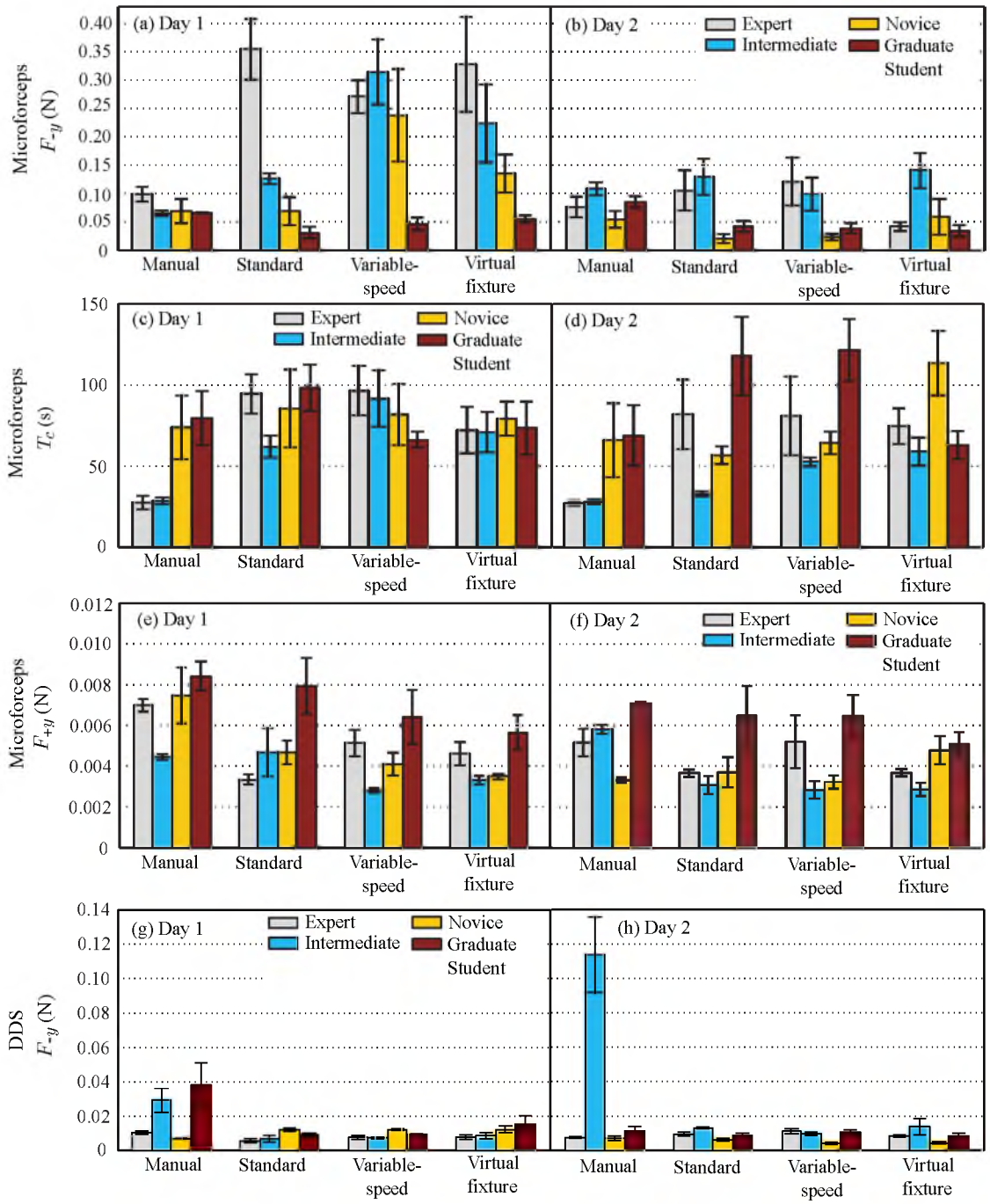

Figure 4.7. Results for Experiments 1 and 2. The maximum downward force (F_{-y}), completion time (T_c), and maximum upward force (F_{+y}) for membrane peeling with a microforceps are shown in (a)–(b), (c)–(d), and (e)–(f), respectively. (g)–(h) shows maximum downward force (F_{-y}) for the scraping task with a diamond-dusted scraper (DDS). Data are divided according to subject, day, and mode of experiment. Error bars indicate standard deviation between trials.

Table 4.1. Statistically significant results ($\alpha < 0.05$) for telemanipulated membrane peeling with a microforceps for all subjects, compared against within-subject manual surgery, and against skilled-surgeon manual surgery. S: Standard telemanipulation, V: Variable-speed controller, F: Virtual fixture controller. '$*$' indicates performance better than manual surgery, '$\sim$' indicates no significant difference was found, and '†' indicates performance worse than manual surgery. The two entries shown in parenthesis are only significant with $\alpha < 0.1$).

	Metric	Expert			Intermediate			Novice			Grad. Student			Subjects 1–5
		S	V	F	S	V	F	S	V	F	S	V	F	S
Within-Subject Manual Surgery	F_{-y}	$\sim$	$\sim$	$(*)$	$\sim$	$\sim$	$\sim$	$(*)$	$\sim$	$\sim$	$*$	$*$	$*$	
	F_{+y}	$*$	$\sim$	$*$	$*$	$*$	$*$	$\sim$	$\sim$	$\sim$	$\sim$	$\sim$	$*$	
	T_c	†	†	†	$\sim$	†	†	$\sim$	$\sim$	$\sim$	$\sim$	$\sim$	$\sim$	
Skilled-Surgeon Manual Surgery	F_{-y}							$*$	$*$	$\sim$	$*$	$*$	$*$	$*$
	F_{+y}							$*$	$*$	$*$	$\sim$	$\sim$	$\sim$	$*$
	T_c							†	†	†	†	†	†	†

We observe that the expert surgeon improves significantly from Day 1 to Day 2 with the standard and variable-speed controllers, bringing his force level down to approximately that of his manual surgery. Also, he performs significantly better than manual surgery when using the virtual-fixture controller on Day 2 ($F(1,7) = 4.0, p = 0.08$); however, his completion time is still significantly higher than manual surgery. The upward forces during membrane peeling F_{+y} reduces significantly with the standard controller and the virtual-fixture controller as compared to manual surgery.

For the graduate student, who is an expert user with the telemanipulation system, forces are lower in telemanipulated surgery for each of the telemanipulation controllers (with Days 1 and 2 lumped together) than in manual surgery; however, his completion time may be slightly slower. We see a slight trend in reducing upward forces with the telemaniulation system as compard to manual surgery, with upward forces (F_{+y}) significantly lower with the virtual-fixture controller as compared to manual surgery. We also find that his downward forces for each of the telemanipulation controllers are significantly lower than those of the skilled surgeons' manual forces; however, his completion time is significantly longer.

Similarly, but maybe more promising, for the novice surgeon with limited surgical experience, forces are lower with the standard controller on Day 2 than in manual surgery ($F(1,7) = 3.9$, $p = 0.094$); in addition, his completion time in telemanipulated surgery is comparable to completion time in manual surgery. We also observe that the novice surgeon's downward forces with the standard controller and variable-speed controller are lower than those of the skilled surgeons' manual forces; however, his completion time is significantly longer. His upward peeling forces F_{+y} are significantly lower with all three controllers for the telemanipulated system as compared to the skilled surgeons' forces in manual surgery.

For the trials with the DDS, only F_{-y} is relevant, as the time for each trial was fixed to 1 min. From Fig. 4.7g–h, we observe that the intermediate surgeon performs significantly better with each of telemanipulation controllers as compared to manual surgery. We also observe the telemanipulated system helps in reducing variance in F_{-y} for the graduate student.

Figure 4.8 shows the experimental results for the third experiment in which five subjects performed telemanipulated membrane peeling with a microforceps for each subject. We use data from the last block of experiments (Block 6) for each subject as representative of their performance after the short two-day training and compare it to the performance of the skilled surgeons in manual surgery for statistical significance. We observe a trend in reducing F_{-y} from Block 1 to 6 for all subjects. For subjects 1, 2, and 3, F_{-y} in Block

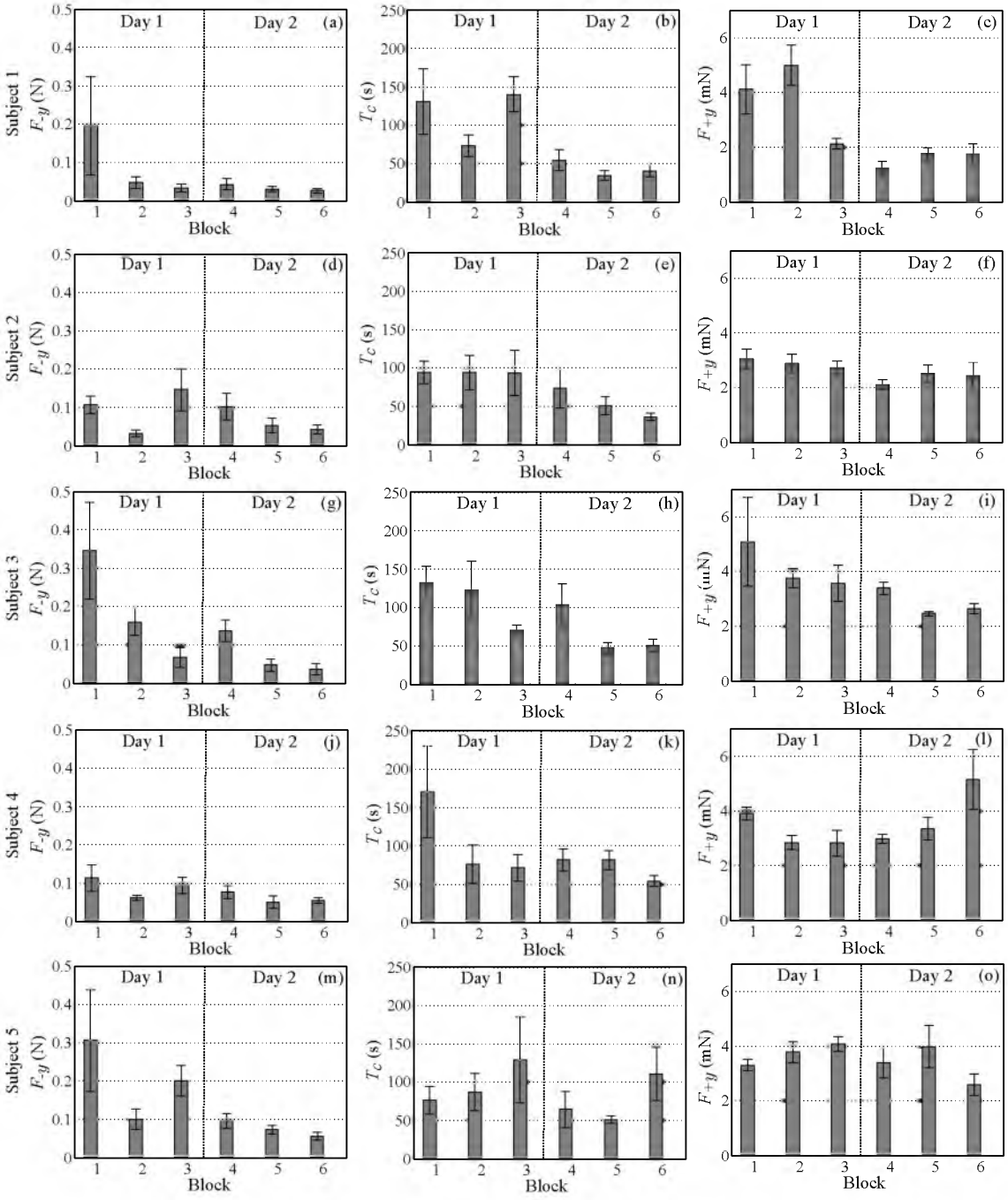

Figure 4.8. Experimental results for telemanipulated membrane peeling with a microforceps in the phantom eye for five subjects who have no experience performing membrane peeling surgery. Blocks 1–3 are performed on Day 1 and Blocks 3–6 are performed on Day 2. Error bars indicate standard deviation between trials.

6 is significantly lower than F_{-y} recorded in manual surgery for the skilled surgeons. For subjects 4 and 5, F_{-y} in Block 6 is significantly lower than F_{-y} recorded in manual surgery for the skilled surgeons, but with lower significance ($p < 0.1$).

We observe that the upward forces F_{+y} for subjects 1, 2, 3, and 5 in Block 6 is significantly lower than that of manual surgery performed by the skilled surgeons. Although no specific instructions were given to the subjects regarding the method of peeling the membrane, we believe that the instruction to minimize downward forces, i.e., perform the procedure more delicately, might have been interpreted by the subjects as an instruction to move slowly when interacting with the membrane, which ultimately resulted in lower F_{+y}.

We observe that T_c is lower on Day 2 compared to Day 1 for all subjects. However, T_c in Block 6 for each of the subjects is still significantly higher than T_c recorded in manual surgery for the skilled surgeons.

Figure 4.9 shows the experimental results shown in Fig. 4.8 with data for Subjects 1–5 combined in a single data set. We observe a reducing trend in F_{-y}, T_c, and F_{+y} from Block 1 to Block 6. We find that with just five subjects, F_{-y} and F_{+y} in Block 6 is lower than that of manual surgery performed by the skilled surgeons with a high significance ($p < 0.001$). T_c in Block 6 is significantly higher than T_c for manual surgery performed by the skilled surgeons.

4.4 Discussion

We observed that the high positioning resolution in telemanipulated surgery (particularly in the vertical direction) often resulted in the membrane being grasped and peeled off in layers, with multiple grasping actions required to peel the membrane, which contributed to a higher T_c. This never manifested itself with manual surgery. It may be necessary to train

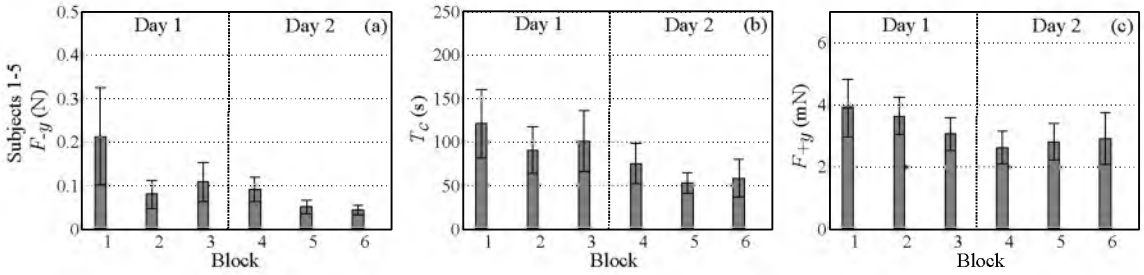

Figure 4.9. Experimental results for telemanipulated membrane peeling with a microforceps in the phantom eye for subjects 1–5 combined. Blocks 1–3 are performed on Day 1 and Blocks 3–6 are performed on Day 2. Error bars indicate standard deviation between trials.

users of the telemanipulator to penetrate *deep enough* into the retina to grasp the entire membrane. Additionally, we believe that the clutching required to reset the master-slave mapping also contributed to higher T_c. Also, it has been shown that positioning stability and perception of contact with the retina for skilled surgeons are significantly higher than that of surgically novice users [66]. This could explain the lower T_c for skilled surgeons as compared to novice users observed in our manual experiments.

Results from our experiments show that subjects performed better than manual membrane peeling surgery when they were trained to use the telemanipulated system over a limited period of time. In an effort to create a balanced experiment, we randomized our trials for different controllers, which we believe had a negative influence on the subjects' performance, since they were constantly having to relearn the current system's behavior. Surgeons performing robotic surgery would be trained to perform robotic surgery with the same system, and their motor skills will not have to compensate for changing system properties between trials as in our experiments. A drawback of our phantom eye setup was the lack of visual cues for forces applied on the retina. Surgeons rely on the deflection and discoloration of the retina as a measure of the force applied during membrane peeling surgery. This visual cue was lacking from our plastic retina, which could have affected our results. However, it has been shown that depth perception with visual feedback through a surgical microscope alone is similar for manual and robotic-assisted retinal surgery [67].

In terms of the achievable precision and velocity at the instrument's end-effector, our manipulator compares well with other retinal-surgery manipulators (Table 4.2). During membrane peeling in manual surgery, instrument velocities have been measured in the range of 0.1–0.5 mm/s [43], which our manipulator is easily capable of achieving. However, we found that during bulk repositioning tasks, velocities higher than our maximum of 6 mm/s would be desirable, if the goal is to recreate instrument movements similar to manual surgery. The skilled surgeons found the velocity limit to be an annoyance. Different kinematics could be used to modify the precision-velocity trade-off. Regardless of kinematics, the quick-change adapter, disposable-instrument actuators, telemanipulation controllers, and custom stylus presented here could be utilized with almost any manipulator kinematics, including many existing systems (Table 4.2). Our system could also incorporate force-sensing instruments [43] for improved safety.

The augmented controllers were designed to assist in membrane peeling close to the retina. Although the surgeons saw value in the augmented controllers, they mentioned that it was harder to get used to the additional damping introduced. Subjectively, they all

Table 4.2. Comparison of robot-assisted retinal-surgery systems. 'NA' indicates no publications or images are available.

System	Resolution/Precision	Max. velocity at the retina	Head-mountable	Quick-change/commercial actuated instruments	Surgeon input
Johns Hopkins [55]	$< 1\,\mu$m/$3\,\mu$m	5 mm/s	No	Yes/No	Cooperative or Telemanipulation
Northwestern [49]	$0.2\,\mu$m/$< 1\,\mu$m	NA	No	No/No	Telemanipulation
Univ. of Western Australia [50]	0.5μm/NA	NA	No	No/No	Telemanipulation
UCLA [54]	NA/NA	NA	No	No/No	Telemanipulation
Univ. of Tokyo [52, 68]	$5\,\mu$m/NA	NA	No	No/Yes	Telemanipulation
TU Eindhoven [53]	NA/$10\,\mu$m	NA	No	NA/No	Telemanipulation
Univ. of Leuven [15, 56]	NA/$3\,\mu$m	NA	No	NA/NA	Cooperative or Telemanipulation
Columbia/Vanderbilt [63, 69]	NA/$< 5\ \mu$m	NA	Yes	Yes/Yes	Telemanipulation
TU Munich [13]	NA/$5\,\mu$m	40 mm/s	Yes	NA/NA	Telemanipulation
Univ. of Utah	**$0.5\,\mu$m/$< 1\,\mu$m**	**6 mm/s**	**Yes**	**Yes/Yes**	Telemanipulation

preferred the standard telemanipulation controller over the augmented controllers. From our experiments, we did not find any statistically significant improvement in performance by using the augmented controllers as compared to the standard telemanipulation controller. The maximum end-effector velocity was limited by the manipulator velocity and the master-slave scaling. Additionally, although our artificial membrane approximates epiretinal membranes in terms of the peeling motions required, it is significantly different in terms of strength. As a result, users could peel a membrane in a single grasp-and-peel motion, which seldom happens in actual surgery. Hence, the augmented controllers should be revisited and evaluated for their performance with a more realistic artificial membrane or with animal studies, or if the system is capable of achieving higher velocities, which would motivate the potential benefits of a software brake.

Due to the underactuation of our inexpensive haptic device (6-DOF with only 3-DOF actuation), we constrained our haptic device to have the same 4-DOF as the instrument's *end-effector* (3-DOF translation + 1-DOF rotation) by mechanically locking the wrist angle of the haptic stylus. Also, in all of our experiments, the RCM point in telemanipulated surgery was fixed, and orbital movement of the eye was not possible. As a result, the hand motions required in telemanipulated surgery with our haptic interface were fundamentally different than in manual surgery in terms of the coupling between end-effector position and instrument/stylus angle. The subjects who perform better than manual surgery with the telemanipulated system also have the least experience in real surgery. Previously developed retinal-surgery telemanipulation systems have used master devices with 3-DOF translation + 1-DOF rotation [68], or with 3-DOF rotation + 1-DOF translation [53], whereas cooperative manipulators and hand-held instruments require the same hand motions as in manual surgery. It is not clear how the kinematic configuration of the master device affects the user's telemanipulation performance; this needs to be investigated further in the context of retinal surgery, potentially including the need for orbital manipulation.

Master-device kinematics aside, the control authority of the master-device actuators may also play a role in performance, particularly with the augmented controllers. The 3-DOF actuation of the Geomagic Touch used here is relatively weak, such that the highest achievable software stiffness binding the Touch's wrist to the projected end-effector is not particularly stiff compared to what could be achieved with more expensive haptic interfaces. As a result, slowing down the end-effector motion, as with the variable-speed controller, also results in a noticeable mismatch between the master and slave motions.

Experimental conditions in our study were ideal, in the sense that there was no patient

eye/head movement. In actual surgery, patient head movement has to be compensated for by the surgeon. We hypothesize that all performance metrics will degrade in manual surgery when patient eye/head movement is involved, whereas a head-mounted telemanipulator will likely show comparable performance to the results obtained here. Regardless, we show that completion times for telemanipulated surgery are already comparable to manual surgery for subjects who are inexperienced in performing actual surgery.

One of the primary motivators for robot-assisted retinal surgery is to prevent the rare mistakes that can happen during manual surgery, potentially leading to surgical complication or vision loss. Sudden eye/head movement is only one potential cause of such a mistake. These rare mistakes can be difficult to capture and characterize during a structured experiment, but we see some indication of this when we consider the results of the intermediate surgeon using the DDS on Day 2, shown in Fig. 4.7h; we see a large spike in downward force with no apparent reason. This is the type of mistake that can be prevented with a robotic system.

In all our experiments, subjects manually manipulated a light probe in the phantom eye with their left hand while either manually or telemanipulating the instrument with their right hand. This directly injects human hand tremor into the system, and also leads to bending of the delicate instruments when they do not work in concert, resulting in unintended motion at the end-effector. To truly demonstrate the capabilities of the telemanipulated system, all manual interaction should be removed by telemanipulating both instruments.

Because of the fixed trocar point in telemanipulated surgery, the motion of the eyeball was negligible. This resulted in clear visualization of the retina, which the surgeons appreciated. The skilled surgeons believe that because of the higher completion time, the telemanipulated system in its current form might not be clinically feasible for the membrane peeling procedures which they are skilled at performing. They believe that the system will be useful for experimental procedures like retinal vein cannulation and gene therapy, which are difficult for even skilled surgeons because of the high precision required.

4.5 Conclusion

In this paper, we have presented a telemanipulation system for retinal surgery that uses unmodified commercially available instruments. The system is compact and light enough that it could reasonably be made head-mounted in future work to passively compensate for head and eye movements. Two actuation mechanisms were developed that enable the system to use commercially available actuated instruments, and a quick-change instrument adapter

was developed that enables change of instruments during surgery. The instrument actuation mechanisms and quick-change instrument adapter could be easily adapted to work with existing retinal-surgery systems. Our experimental results with a force-sensitive phantom eye show that telemanipulated surgery shows promise in reduction of peak downward forces on the retina as compared to manual surgery for surgically novice users, and training with the system results in improved performance.

4.6 Acknowledgements

This project was funded by Intuitive Surgical Technology Research Grants and an unrestricted departmental grant to the Moran Eye Center from Research to Prevent Blindness. The authors would like to thank Alexandra Shamir for her technical assistance, Dr. Nikhil Batra and Dr. Jim Bell for their assistance with surgical equipment, Dr. Stephen Mascaro for allowing use of his lab equipment, and SmarAct GmbH for technical support. This work made use of University of Utah shared facilities of the Micron Microscopy Suite sponsored by the College of Engineering, Health Sciences Center, Office of the Vice President for Research, and the Utah Science Technology and Research (USTAR) initiative of the State of Utah.

CHAPTER 5

EFFECT OF HAPTIC-INTERFACE KINEMATICS ON PERFORMANCE IN TELEMANIPULATED RETINAL SURGERY

5.1 Introduction

Minimally invasive surgical procedures of the retina—including, but not limited to, peeling of membranes, cannulation for retinal-vein occlusions, and repair of retinal tears—involves inserting instruments into the eye through trocars on the sclera. With these instruments, surgeons manipulate delicate structures that can range from $0.5\,\mu$m to a few hundred micrometers [45, 46] (Fig. 5.1). Additionally, surgeons must pivot the instruments about the trocars to reduce excessive stress on the scleral tissue, and reduce unwanted eye motion for a stable visualization. Procedures like membrane peeling require delicate and accurate motions of the instruments by the surgeon. For example, scraping membranes with a diamond-dusted scraper requires motions similar to painting with a brush. Grasping the membrane and peeling it with a forceps requires slow controlled movements just above the surface of the retina to reduce fragmentation of the membrane. The curvature of the retina poses a challenge to the surgeon, especially to inexperienced surgeons who often fail to compensate for the curvature. To perform the complex motions required in retinal surgery, surgeons use a combination of rotary and linear motions to achieve the desired end-effector motion while trying to minimize motion at the trocar. As a result, retinal-surgical procedures are difficult, and it take years of training to master.

To improve surgical outcomes in retinal surgery, a number of research groups have developed robot-assisted retinal-surgery systems—including both telemanipulated systems [13, 15, 49, 52, 53, 70], and cooperative manipulators [55, 56] that could be used in a telemanipulated approach—which have been shown to improve positioning precision in retinal procedures. There are two primary potential benefits that motivate telemanipulated surgical

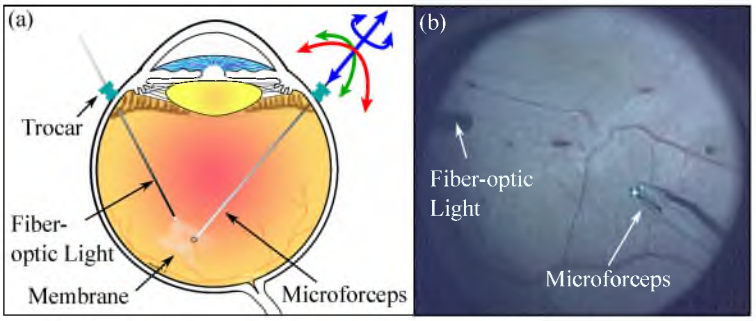

Figure 5.1. Membrane-peeling surgery. (a) Surgeons use a combination of three rotary and one translational motions of the instrument to achieve the desired instrument motion inside the eye while trying to maintain the trocar point stationary. Modified version of image courtesy James Gilman, CRA, FOPS. (b) Membrane-peeling surgery as seen through a surgical microscope. Image courtesy Nikhil Batra, M.D.

systems relative to both manual surgery and cooperative manipulators. The first is the ability to scale down the motion of the surgeon's hand to improve precision, which can be combined with filtering for additional tremor reduction [56]. The second is the ability to provide "intuitive" control directly over the end-effector of the instrument, as opposed to controlling the less-intuitive inverted motion of the instrument's handle. This potential benefit is motivated by the intuitive nature of robotic systems such as the da Vinci Surgical System compared to manual laparoscopic surgery. However, as we show in this paper, how to implement intuitive control of the end-effector is not trivial, and a recent study suggests that we should not automatically assume that telemanipulated retinal-surgery systems are more intuitive than cooperative manipulators [56].

The trocar constrains the instrument to a point on the surface of the eye, kinematically removing two degrees-of-freedom (2-DOF), leaving only 4-DOF to define the pose of the instrument. These 4-DOF include the 3-DOF orientation about the center of the trocar—this orientation is typically controlled using a remote-center-of-motion (RCM) mechanism [55], or a "virtual RCM" implemented in software—and an additional 1-DOF translation through the trocar, as depicted in Fig. 5.1. For intuitive control of the instrument's end-effector, these 4-DOF are mapped to the 3-DOF Cartesian position of the end-effector, and the 1-DOF rotation of the end-effector about the axis of the instrument's shaft. That is, once the surgeon establishes the position of the end-effector, 2-DOF of its orientation are constrained. (Note that this is true of rigid instruments, but it is not the case when using "intra-ocular dexterity" devices [70].) The precise manipulators used for retinal surgery typically have limits on achievable velocity (relative to achievable velocity of the human hand), so it is typically desirable to utilize a haptic interface that has, at a minimum,

actuation in the 3-DOF Cartesian position to convey the instrument's constrained velocity to the surgeon.

Due to the kinematic constraints imposed by the trocar, there is not a unique "correct" mapping from the 6-DOF pose of the surgeon's hand to the 4-DOF pose of the end-effector. As a result, different research groups have utilized different haptic-interface kinematics in their respective telemanipulation systems; these choices have typically been made with some rationale, but without rigorous justification. The three most common haptic-interface kinematic are as follows.

5.1.1 4-DOF Virtual Trocar

Constrain the haptic interface to have the same kinematic constraints as the instrument. As the 3-DOF position of the end-effector and 1-DOF rotation about the instrument's shaft axis is controlled, the 2-DOF orientation of the haptic interface's stylus matches that of the instrument through the trocar, effectively creating a virtual trocar in the haptic interface's workspace. The potential benefit of this type of haptic-interface kinematics is that there is always a one-to-one mapping between motions of the haptic interface and motions of the instrument, and there is always a direct correspondence between the pose of the stylus in the surgeon's hand and the instrument being observed in the microscope. This can be accomplished independent of master-slave scaling, since rotations are invariant to scaling. Research groups in [14] and [15] use this approach by implementing a mechanical kinematic constraint to act as the trocar in their custom haptic interfaces. These kinematics can also be implemented in software with a haptic interface with 6-DOF actuation, but these devices tend to be relatively large and expensive.

5.1.2 6-DOF Underactuated

Utilize an inexpensive haptic interface that has 6-DOF motion but only 3-DOF actuation. The most common example of this type of interface is the Geomagic Touch (formerly the PHANTOM Omni). The actuated 3-DOF Cartesian position of the stylus' gimbal (i.e., wrist) is mapped to the 3-DOF Cartesian position of the instrument's end-effector, and the sensed-but-not-actuated rotation about the stylus' axis is mapped to the rotation of the instrument about its shaft axis. This method leaves the 2-DOF "pointing" orientation of the stylus free; the surgeon can rotate the stylus' unactuated 2-DOF gimbal without any motion of the instrumentkdeals.net/ resulting, which has the potential to lead to confusion. Additionally, the orientation of the stylus in the surgeon's hand will not be aligned with the orientation of the instrument observed in the microscope in general, which could also

contribute to confusion. Potential benefits of this type of haptic interface include low cost and compact size. The research group in [16] used this approach with a custom haptic interface that effectively utilizes the same kinematics and actuation of the Geomagic Touch.

5.1.3 4-DOF Separable

Utilize a haptic interface that is essentially two decoupled interfaces—a 3-DOF Cartesian interface that is mapped to the 3-DOF Cartesian position of the end-effector, and a 1-DOF rotation that is mapped to the 1-DOF rotation about the instrument's shaft axis. Our group recently implemented such a haptic interface by mechanically locking the gimbal of a Geomagic Touch to eliminate 2-DOF [61]. Unlike with the 4-DOF Virtual Trocar kinematics, there is no attempt here to align the stylus' 2-DOF pointing orientation with that of the instrument (which we have established cannot be controlled independently of the end-effector's position). This method is motivated by studies that show that translations and rotations are *separable* in the human mind [71,72]. The potential benefit of this type of haptic interface is that there is a one-to-one mapping between motions of the haptic interface and motions of the instrument, unlike with the 6-DOF Underactuated kinematics, but with the same low cost and compact size of the 6-DOF Underactuated interfaces. However, using this method, there is not perfect correspondence between the 2-DOF pointing orientation of the stylus in the surgeons's hand and the orientation of the instrument observed in the microscope, which could lead to confusion.

In [61], we developed a compact retinal-surgery telemanipulator, which was telemanipulated using a gimbal-locked Geomagic Touch haptic interface with 4-DOF, as described above. In our experiments, we found that subjects who were inexperienced in real retinal surgery performed better (in certain metrics of success) than expert surgeons who had performed a significant number of real surgeries. Additionally, the expert surgeons complained that the restrained gimbal prevented them from using their own wrist motions efficiently. This led us to question the efficacy of locking the stylus' gimbal to enforce 4-DOF motion, and ultimately led to the study in this paper. We previously hypothesized that the 4-DOF Virtual Trocar kinematics would be the best (albeit most expensive) option if it were available, and that the 6-DOF Underactuated kinematics would be the worst option due to the seeming disconnect between 6-DOF hand motions and 4-DOF instrument motions. However, as we will show, this hypothesis was incorrect.

In this paper, we study operator performance on a positioning task that simulates motions used in retinal surgery. We compare performance using the three different haptic-interface kinematic introduced previously. The retinal-surgery manipulator introduced

in [61] is used in the experiments, and the different haptic-interface kinematics are implemented, in software, on a PHANTOM Premium 6DOF haptic interface. We present results from an experiment with 12 human subjects, using a variety of performance metrics designed to quantify the subjects' ability to perform precise and efficient motions representative of retinal surgery. The conclusion of our study is that the 6-DOF Underactuated kinematics, which is a simple, compact, and inexpensive option, leads to the best overall performance. However, we provide discussion with caveats to this conclusion.

5.2 Methods

5.2.1 Subjects

An experiment is performed by 12 (4 female) right-handed subjects with ages ranging from 23 to 42 years, recruited from the university population, with the approval of the institutional review board. Subjects had normal touch sensation and normal (corrected) vision, by self-report. Subjects were not compensated for their participation.

5.2.2 Apparatus

5.2.2.1 Retinal manipulator

The manipulator (Fig. 5.2), developed in [61], comprises a 3-DOF translation stage and a 3-DOF spherical wrist, which enables the manipulator to position the instrument inside a 20-mm-diameter spherical-section bowl centered on the retina with a virtual RCM on the surface of the eye (a sphere of 25.4-mm diameter). The positioning precision of the manipulator while performing constrained motion near the retina is $<1\,\mu$m, and the maximum velocity at the end-effector is 6 mm/s. Because the manipulator utilizes piezoelectric stick-slip actuators, it effectively behaves as an *admittance-type* device.

5.2.2.2 Telemanipulation system

A PHANTOM Premium 6DOF is used as the master haptic interface to telemanipulate the retinal-surgery slave manipulator. A master-slave position controller is implemented in which the scaled slave end-effector position is mapped as a proxy point in the master workspace, and a software spring-damper ($K_p = 0.1\,$N/mm, $K_d = 0.004$N·s/mm) is implemented between the proxy and the position of the haptic-interface gimbal. The scaled position of the master's gimbal is given as a position command to the slave's end-effector. The orientation of the stylus is set according the haptic-interface kinematics used, as described below. A low-level controller is implemented to servo the end-effector to the desired Cartesian position in its workspace. A clutch (foot pedal) is used to engage/disengage the

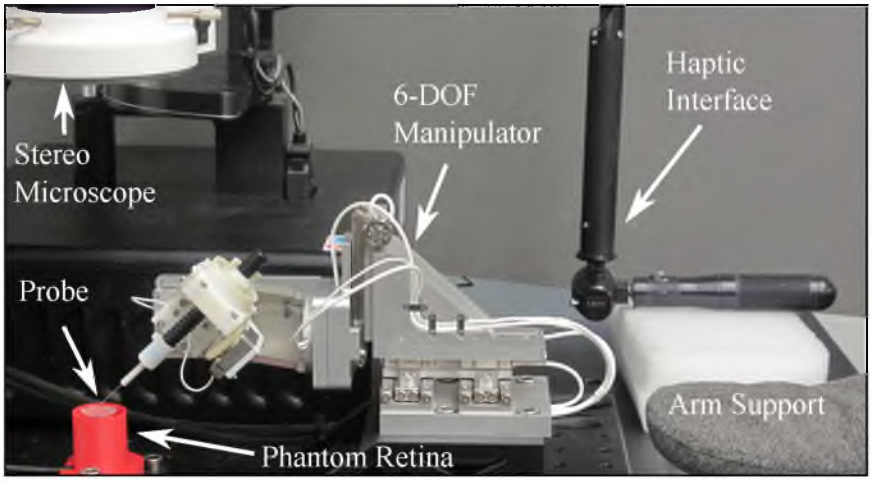

Figure 5.2. Experimental setup of the retinal-surgery system. The surgeon looks at the phantom retina using a stereo microscope, and telemanipulates the end-effector of the instrument using the PHANTOM Premium 6DOF haptic interface under different software-controlled kinematics to interact with a force-sensitive phantom retina.

slave from the master. The RCM movement of the instrument about the trocar is handled in software. A master-slave scaling of 8:1 was chosen such that the task would not require repositioning of the master during a trial. For reference, an 8:1 scaling was used in [61], and a 7:1 scaling was used in [53]. An instrument with a tungsten probe at the tip was used as the end-effector for experiments in this study.

Three different haptic-interface kinematics as described in Section 5.1 were implemented in software. Figure 5.3 shows the orientation of the haptic-interface stylus when the end-effector is at different points on the retina. With the 4-DOF Virtual Trocar kinematics, a trocar point is mapped to the workspace of the haptic interface, and the required orientation of the stylus is calculated based on the trocar point and the end-effector position. A software spring-damper ($K_p = 4000\,\mathrm{N/rad}$, $K_d = 15\ \mathrm{N{\cdot}s/rad}$) is implemented on the two master gimbal joints to achieve the desired orientation for the stylus. The result is that the orientation of the stylus matches the orientation of the instrument on the manipulator at each instant as can be seen in Fig. 5.3i l. In our experiments, a fixed trocar point is used. With the 6-DOF Underactuated kinematics, the operator is free to rotate the stylus as they wish. With the 4-DOF Separable kinematics, the gimbal joints of the interface are fixed at a constant value relative to the previous link, which simulates a mechanical gimbal lock, using the same gimbal controller gains described above (Fig. 5.3m–p). Because of the specific haptic interface used, the orientation of the stylus at points 1 and 2 on the retina are similar with the 4-DOF Virtual Trocar and 4-DOF Separable kinematics,

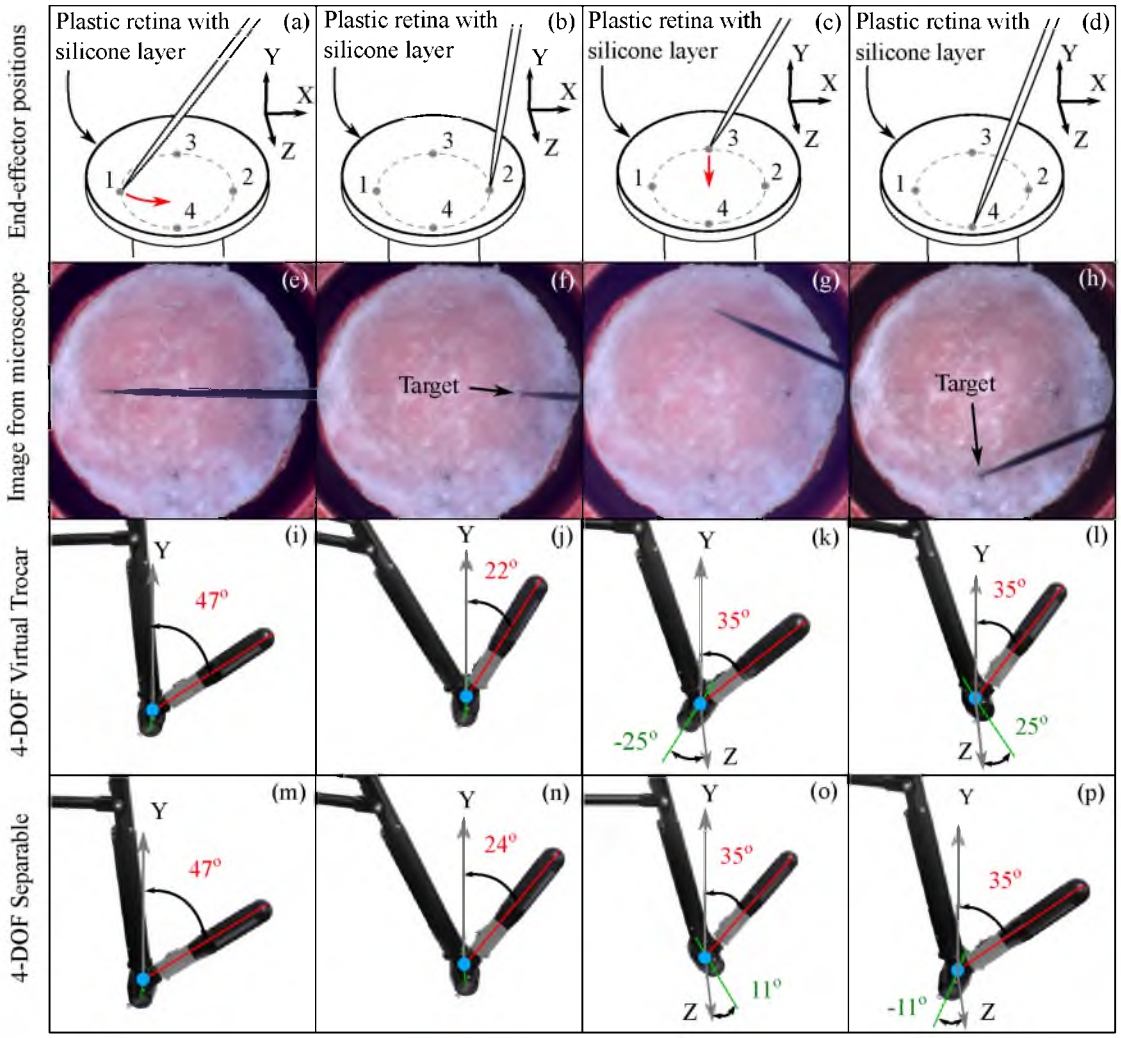

Figure 5.3. Relation between end-effector and stylus orientations. (a)–(d) Illustration of the end-effector at different target points on the retina. (e) (h) Microscope image of the phantom retina with the end-effector at different target points as shown in (a)–(d), respectively. The black dots ($\sim$100 μm) are the target points to which the subjects move the end-effector, labeled in (f) and (h). The haptic-interface stylus orientations are shown in (i) (l) for the 4-DOF Virtual Trocar kinematics, and in (m) (p) for the 4-DOF Separable kinematics, for the end-effector positions in (a)–(d), respectively; with the 6-DOF Underactuated kinematics, the orientation of the stylus is controlled by the operator, and hence not shown. The blue dot in the center of the gimbal indicates the point on the haptic interface that is mapped to the end-effector of the manipulator (i.e., the tip of the instrument), and the grey region indicates the gripping area on the stylus.

whereas the orientations are approximately mirrored about the XY plane at points 3 and 4. In all three haptic-interface kinematics, the roll joint on the stylus is locked in software ($K_p = 4000\,\mathrm{N/rad}$, $K_d = 15\,\mathrm{N{\cdot}s/rad}$) since rotation of the instrument about its shaft axis is not relevant for the Cartesian positioning task used in this study.

5.2.2.3 Phantom Eye

A phantom eye setup is used to simulate the retina in this study [61]. The setup consists of a plastic retina with the curvature of a 25.4-mm sphere, which is mounted on an ATI Nano17 SI-12-0.12 force/torque sensor (noise $< \pm 4$mN). A 0.5-mm-thick silicone layer (Dragon Skin 30, Smooth-On Inc.) is attached to the plastic retina to simulate the deformable behavior of a real retina. The stiffness of the silicone layer is different from that of an actual retina, and hence, the forces measured in this study can only be used for comparisons within this study.

5.2.3 Procedure

During the experiment, subjects telemanipulated the tip of the tungsten-probe instrument of the retinal manipulator while visualizing the retina through a microscope. The subjects were instructed to hold the stylus of the haptic interface like a pen. In each trial, the subject had to move the end-effector from one point to another on the surface of the retina (Fig. 5.3a–d). Trials were performed in the X direction (point 1 to point 2) or the Z direction (point 3 to point 4). At the start of a trial, the end-effector was automatically positioned at the start point (point 1 or 3), and subjects were instructed to move the probe tip to the end point (point 2 or 4, respectively) along a straight line as viewed from above while maintaining contact with the silicone retina. The subjects were instructed to touch the retina as delicately as possible without breaking contact, while drawing as straight a line as possible to the target, and they were instructed to take as much time as necessary to do so. An audio alarm was played when the downward force on the retina was less than 4 mN (the sensor's noise level), indicating the probe tip was not touching the retina sufficiently. Subjects were instructed to note the deformation of the retina as an indication of excessive downward forces.

Ten trials were performed per subject for each combination of direction and haptic-interface kinematics. Six permutations of the order of the three different haptic-interface kinematics are possible, and two subjects perform each particular order. The order in which the two different directions are assigned for a particular haptic-interface kinematics was randomized, and all the ten trials for a particular direction are performed together,

followed by the next direction. After changing to a new haptic-interface kinematics, subjects were given a 5-min trial period with the new system.

Points 1, 2, 3, and 4 were determined by the experimenter by touching the points on the surface with the probe tip and registering the positions in software before the start of experiments, and were the same for all the subjects. The distance between point 1 and point 2, and point 3 and point 4, was 11 mm. During experiments, the sclera of the model eye [61] was removed after registering the trocar position to provide an unhindered view of the silicone retina and to eliminate the need for a fiber-optic light source.

At the end of the experiment, subjects were asked to rate the different haptic-interface kinematics in terms of the most comfortable and the least comfortable, and the haptic-interface kinematics in which they thought (subjectively) that their control of the probe tip was best and worst.

5.2.4 Measures

To evaluate performance, we use a variety of metrics to quanitfy the deviation of the probe tip from the desired straight-line path as viewed from above, the ability to follow the curvature of the retina while controlling the forces applied on the retina, and the completion time for a trial. Figure 5.4a and 5.4b shows the path taken by the probe tip and the force data, respectively, during a typical trial in which the subject is telemanipulating the probe tip from point 3 to point 4. Data in a trial were analyzed only after the probe tip moved a distance of 1 mm from the start point.

To measure deviation from the desired straight-line path as viewed from above, we compute the mean deviation ($\bar{d}$) and the maximum deviation ($d_{\max}$) of the probe tip from a vertical plane passing through the two points of interest (see Fig. 5.4a). A low value for $\bar{d}$ and $d_{\max}$ is desirable.

To measure the ability of the subject to follow the curvature of the retina, we use the fraction of the completion time for a trial for which the probe tip is not in contact with the retina (τ_{nc}). The end-effector is considered to be not in contact with the retina if the force magnitude on the retina is less than 4 mN. A value of $\tau_{nc} = 0$ would mean that the subject maintained contact with the retina throughout the trial (never hearing the audio alarm), and $\tau_{nc} = 1$ would indicate that the audio alarm was on for the entire trial and the subject did not maintain sufficient contact. An ideal subject touching the retina as delicately as possible would have a value of $\tau_{nc} = 0.5$ approximately, indicating that the subject could perfectly track the curved retinal surface with a delicate touch.

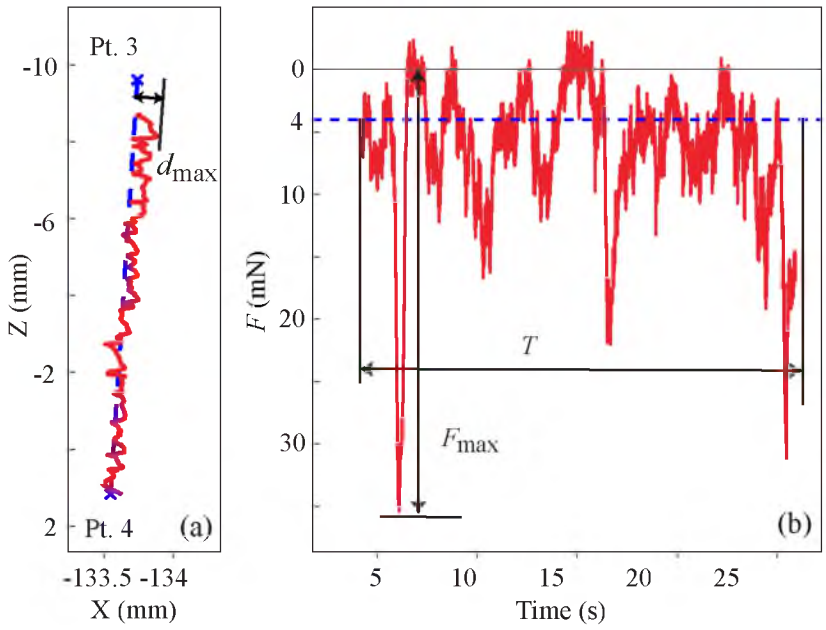

Figure 5.4. Typical experimental trial. (a) Position of the probe-tip (solid red line) as the subject telemanipulates it from point 3 to point 4 (blue crosses connected by blue dashed line). (b) Corresponding force data from the phantom retina segmented above and below the threshold force.

To evaluate the subjects' ability to control downward forces applied on the retina, we look at the mean downward force ($\bar{F}$) and the maximum downward force ($F_{\max}$) in a trial (see Fig. 5.4b). Only force magnitudes above the threshold of 4 mN are considered for calculating $\bar{F}$ and $F_{\max}$. A low value for $\bar{F}$ and $F_{\max}$ is desirable. We also note that τ_{nc} should be taken into account when evaluating force results (e.g., a seemingly good mean force could result from poor contact being maintained).

Finally, we look at the total completion time (T) for a trial. Although subjects were instructed to take as much time as required to complete a trial, the completion time gives us information about the intuitiveness of the different haptic-interface kinematics.

5.3 Results

Figure 5.5 shows the experimental results for all conditions and subjects. We find a strong effect of the direction of the motion of the probe tip (X vs. Z), so the results for each direction are analyzed separately. An independent-samples t-test was used to compare the different kinematics, using a significance level of $\alpha < 0.05$.

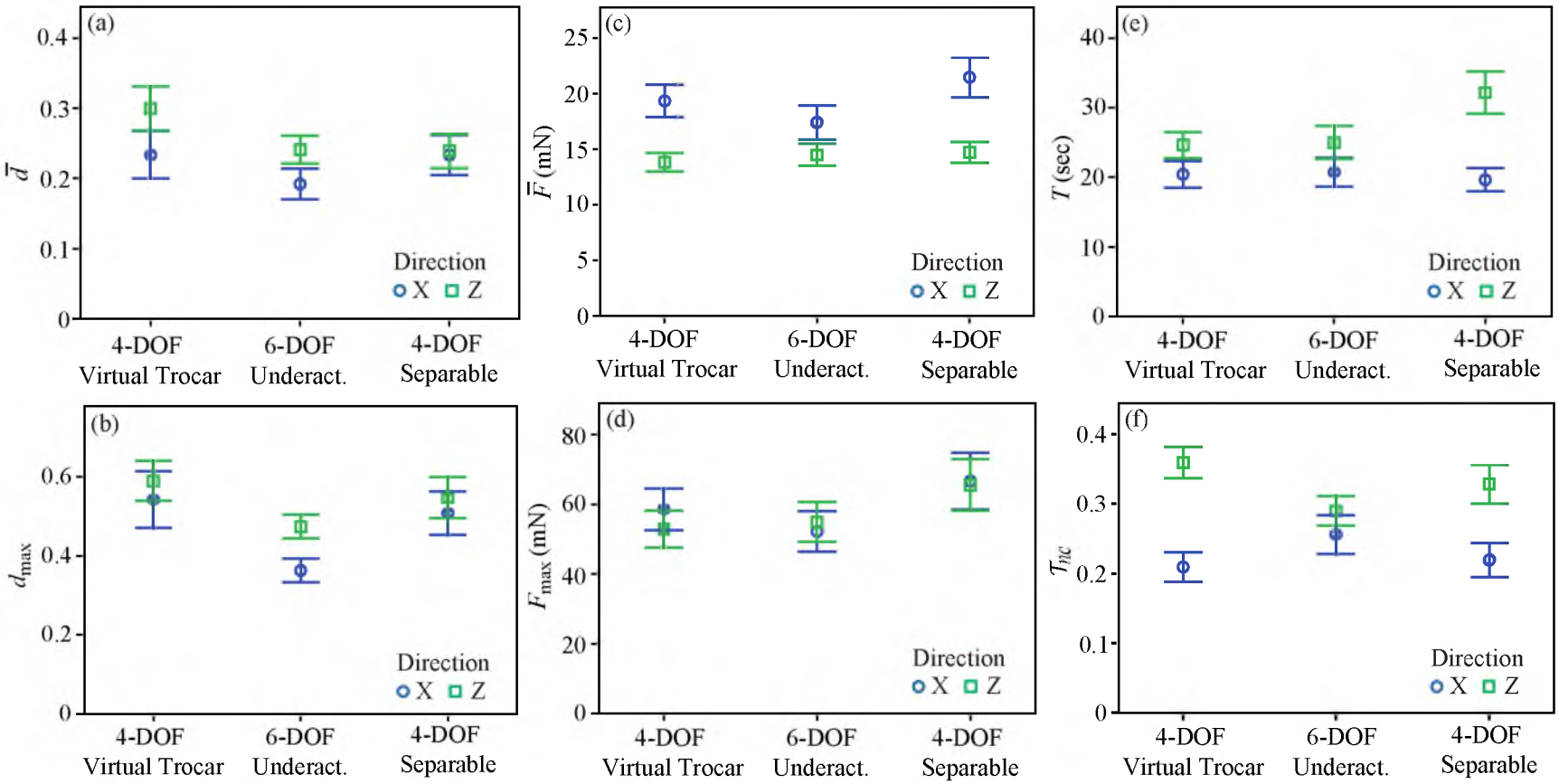

Figure 5.5. Experimental results for all subjects and trials for $\bar{d}$, $d_{\max}$, $\bar{F}$, $F_{\max}$, T, and τ_{nc} for a given haptic-interface kinematics and motion direction. Error bars indicate the 95% confidence interval on the mean.

5.3.1 Ability to follow a desired path

We find that the mean devation from a straight path as viewed from above ($\bar{d}$) is significantly higher with the 4-DOF Virtual Trocar kinematics than with both of the others for motions in the Z direction (Fig. 5.5a). $\bar{d}$ is significantly lower with the 6-DOF Underactuated kinematics than with both of the others for motions in the X direction. We find that the maximum deviation from the straight path ($d_{\max}$) is significantly lower with the 6-DOF Underactuated kinematics than with both of the others for motions in both the X and Z directions.

We find that the fraction of time for which the end-effector is not in contact with the retina (τ_{nc}) is significantly lower (i.e., farther from 0.5) with the 6-DOF Underactuated kinematics than with both of the others for motions in the Z direction. However, τ_{nc} is significantly higher with the 6-DOF Underactuated kinematics than with both of the others for motions in the X direction, and it appears that it is in this direction that subjects have the most difficulty following the curved retinal surface (based on this metric).

By looking at the results for $\bar{d}$, $d_{\max}$, and τ_{nc} in their totality, we conclude that the 6-DOF Underactuated kinematics leads to the best overall performance in terms of being able to precisely control the end-effector of the instrument along a desired path on the surface of the retina.

5.3.2 Force applied to the retina

We find that the mean downward force on the retina ($\bar{F}$) is significantly lower with the 6-DOF Underactuated kinematics than with the 4-DOF Virtual Trocar kinematics, which is in turn significantly lower than with the 4-DOF Separable kinematics for motions in the X direction (Fig. 5.5c). We find that the maximum downward force on the retina ($F_{\max}$) is significantly higher with the 4-DOF Separable kinematics than with both of the others for motions in the Z direction. $F_{\max}$ is significantly higher with the 4-DOF Separable kinematics than with the 6-DOF Underactuated kinematics in the X direction (Fig. 5.5d). We also note that the maximum forces are an order of magnitude larger than the sensor's noise. By looking at these results together, we find that the 6-DOF Underactuated kinematics leads to the best performance in terms of being able to precisely control (and limit) the force applied to the retina, and the 4-DOF Separable kinematics leads to the worst performance.

5.3.3 Completion time

We find that the completion time (T) for motions in the Z direction is significantly higher with the 4-DOF Separable kinematics than with both of the others (Fig. 5.5e). We believe

that these poor results are likely because subjects cannot use changes in hand orientations to control the center of the gimbal, and as a result, they have to translate their entire hand, which requires slower movements to be precise. It is also possible that the incorrect orientation of the stylus during motions in Z (see Fig. 5.3o–p) causes the operator to slow down. We note that the longer completion time did not correspond to more precise motion or better force control, and conclude that the 4-DOF Separable kinematics performs the worst in terms of completion time.

5.3.4 Qualitative assesment of different kinematics

The majority of subjects (92%) found the 6-DOF Underactuated kinematics to be the most comfortable to use and believed that they had best control of the end-effector with these kinematics (58%). The majority of subjects found the 4-DOF Virtual Trocar kinematics to be the least comfortable (58%) and believed these kinematics resulted in the worst control over the end-effector (67%). The qualitative surveys clearly point to the 6-DOF Underactuated kinematics being the most preferred, and the 6-DOF Virtual Trocar being the least preferred.

5.3.5 Summary of results

We find that for a task that is reminiscent of tracing the surface of the retina while applying a gentle force, the subjects' performance was best with the 6-DOF Underactuated kinematics, and the subjects also preferred these kinematics over the others considered. After the 6-DOF Underactuated kinematics, subjects' performance was best with the 4-DOF Virtual Trocar kinematics; however, subjects subjectively preferred these kinematics the least of the three considered.

5.4 Discussion

The hand motions required (and permitted) with the three haptic-interface kinematics are quite different from each other. With the 4-DOF Virtual Trocar, the subjects use coupled translations and rotations of the hand/wrist to move the stylus such that the orientation constraint on the stylus due to a fixed trocar point was satisfied. With the 6-DOF Underactuated kinematics, it was observed that the subjects typically used wrist rotations to move the stylus, as the orientation of the stylus is set by the subject as desired. With the 4-DOF Separable kinematics, the subjects had to largely use translations of the hand to move the stylus. This difference in the type of motion required by the subjects likely explains the degraded performance with the 4-DOF Separable kinematics, as maintaining

precision while using translation hand movements (i.e., arm movements) is difficult. This is supported by prior research which shows that movement time for a task is lower with wrist motions compared to arm motions as the task difficulty increases [73, 74]. Due to the kinematic similarity between the 4-DOF Virtual Trocar and 4-DOF Separable kinematics in the X direction, they show similar performance across metrics in the X direction, as expected.

It should be noted that the subjects in our study were surgically inexperienced, and the outcomes, in terms of the objective and subjective metrics, could be different for experienced retinal surgeons.

In our study, the 4-DOF Virtual Trocar kinematics were implemented in software using a fully actuated PHANTOM Premium 6DOF haptic interface. We must be cautious that our results may be affected by that implementation, and may not apply directly to custom 4-DOF Virtual Trocar interfaces that implement the kinematics mechanically. In a software implementation, end-effector motions require simultaneous translation and rotation motions of the stylus. Because the haptic interface used in this study is an impedance-type device, the orientation constraint on the stylus has limited stiffness. Any error in the orientation between the stylus and the desired orientation will cause a restoring torque on the stylus opposing the movement of the stylus by the subject away from the desired orientation. For instance, if the subject attempts to move the stylus with a pure translation, without permitting the controller to properly orient the stylus, a torque will be applied on the stylus to reduce its orientation error. Alternatively, if the subject attempts to use mainly rotary motion of the stylus, like observed with the 6-DOF Underactuated kinematics, a restoring torque will be applied against the pure rotary motion of the stylus induced by the subject. This effect is pronounced if minimal master-slave scaling is implemented, since a small translation of the end-effector (and thus the stylus) corresponds to a relatively large change in instrument (and thus stylus) orientation, which can result in large restoring torques. For the 8:1 master-slave scaling used in this study, the restoring torques seemed negligible. We believe that the combined effect of the restoring torques and the complexity of movement required with the 4-DOF Virtual Trocar kinematics contributed to the low scores in its subjective qualitative assessment. It is possible that a haptic device that is capable of rendering stiffer environments could lead to better outcomes with the 4-DOF Virtual Trocar kinematics implemented in software.

Until this point, we have neglected an important component of retinal surgery: orbital manipulation. During retinal surgery, surgeons often rotate the eye (under the stationary

microscope) to better visualize a specific location on the retina, and then perform precision tasks at that new location. This is accomplished by using the two instruments, acting in concert, to apply forces on the trocars. So although the instrument movements considered in this paper were only 4-DOF, a surgeon utilizes the full 6-DOF pose of an instrument to perform retinal surgery (2-DOF for orbital manipulation, and 4-DOF for movement within the eye). This means that any retinal-surgery robot should also be capable of manipulating the 6-DOF pose of the instrument, if orbital manipulation is required. However, this does not necessarily mean that the master haptic interface in a telemanipulated retinal-surgery system must have 6-DOF. If the intent is to recreate the method of manual orbital manipulation at the master, the most obvious way to accomplish it is using a 6-DOF fully actuated haptic interface, such as the PHANTOM Premium 6DOF used in this paper. It would be difficult to recreate manual orbital manipulation using a 6-DOF Underactuated haptic interface, such as a Geomagic Touch, since it is not possible to render trocar forces to the stylus and it is not possible to enforce coordination of the styluses of the left and right hands. However, one could imagine methods in which orbital manipulation could be accomplished in a telemanipulation scenario that do not attempt to recreate the haptics of manual orbital manipulation—methods that could be implemented with 6-DOF Underactuated interfaces or custom 4-DOF interfaces—using clutching techniques that decouple orbital manipulation from precision instrument motions. In any case, the results of the study in this paper should be considered not only in determining the type of haptic interface to use in a retinal-surgery telemanipulation system, but also how that interface is controlled during tasks that require high precision.

5.5 Conclusion

We have studied operator performance during a task reminiscent of telemanipulated retinal surgery with three different haptic-interface kinematics that have been utilized in prior systems. The different kinematics were implemented in software on a PHANTOM Premium 6DOF haptic interface. An instrument attached to a retinal-surgery manipulator was telemanipulated to perform a precise positioning task on a force-sensing phantom retina. Results from a study with 12 human subjects show that the subjects' overall performance was best, in terms of the ability to precisely and quickly trace a desired path on the curved surface of the retina while applying gentle forces, with the kinematics that represent a compact, inexpensive, and commercially available option, and that subjects' subjective preference agrees with the objective performance results.

CHAPTER 6

RECOMMENDATIONS FOR FUTURE WORK

The retinal manipulator developed in Chapter 4 was designed to be head-mountable. The head-mounting of the retinal manipulator will mitigate complications due to movement of the patient's head relative to the instrument. Due to head movement, the high resolution of the manipulator cannot be capitalized on for procedures like retinal vein cannulation, which requires inserting a delicate needle in a retinal vein that measures less than 100 μm in diameter. Spontaneous retinal venous pulsations have shown to change the diameter of retinal veins [75]. So even after head-mounting the manipulator, retinal venous pulsations can cause unintended relative motion between the instrument and the retina. The head-mounting mechanism needs to be developed and the hypothesis that head-mounting a manipulator will sufficiently remove unintended relative motion between the instrument and the retina enabling efficient cannulation of retinal veins has to be tested.

In our experiments, we observed that the maximum velocity of our manipulator was not sufficient for bulk repositioning tasks during simulated membrane peeling surgery. The maximum velocity at the end-effector is limited by the maximum joint velocities which are relatively low. Tasks that require high resolution are generally performed at low velocities, and tasks that require high velocities do not generally require high resolution. A potential kinematic design for the manipulator could use additional degrees of freedom to modify the structure of the manipulator such that the trade-off between resolution and velocity at the end-effector can be choosen based on the task.

The studies presented in this work have not addressed an important requirement in retinal surgery: accessing the periphery of the retina. In real surgery, surgeons rotate the eye with the instruments inserted into the eye (known as orbital manipulation) to visualize and access the peripheral retina. Two different approaches can be used to access the peripheral retina in robot-assisted retinal surgery: (1) rotate the eye as in manual retinal surgery by moving the trocar on the sclera, or (2) develop an actuated vision system

that visualizes the peripheral retina without moving the eye. Although our manipulator is capable of moving the trocar on the surface of the eye, rotating the eye with instruments inserted into the eye will require multiple manipulators for coordinated movement between the different instruments inserted. With an actuated vision system, a manipulator with a larger workspace, or an end-effector with high intraocular dexterity [70], will be required to access the peripheral retina. An actuated vision system has been developed for robot-assisted cataract surgery [76], and a similar system could potentially be used for visualization in retinal surgery. However, it is not clear which of the two methods described here would be appropriate for accessing the periphery of the retina in retinal surgery.

The requirements of a haptic interface for retinal surgery needs to be explored further. Chapter 5 compares different haptic-interface kinematics required for retinal-surgery. Surgeons have to use coupled translations and rotations of the hand to achieve the desired end-effector motions inside the eye. Instrument motions required in different procedures such as membrane peeling and retinal vein cannulation are significantly different. Retinal vein cannulation requires slow positioning of a needle close to the retina, followed by insertion of the needle into a vein. In contrast, membrane peeling requires scraping with diamond-dusted scraper, which involves relatively fast movements across the retinal surface. The haptic interfaces for retinal surgery have to be compact if the goal is to incorporate the system with existing surgical microscopes used to visualize the retina. Further, the haptic-interface should have provisions for controlling the trocar on the sclera to enable orbital manipulation. This could be accomplished by a haptic-interface that enables full 6-DOF control of the instrument, or a system with a clutching mechanism that enables switching between controlling the end-effector and controlling eye rotation. It is not obvious which of the two methods would result in the best performance for an operator telemanipulating a retinal-surgery system.

Finally, other applications in microsurgery could be explored for the telemanipulation system developed in this work. Owing to the design of our manipulator, software modifications will enable it to satisfy workspace requirements for other procedures in the eye, such as cataract surgeries and stent placement for glaucoma, and for certain neurosurgical procedures [77]. The compact size of the manipulator combined with the ability to be mounted on a stereotactic frame would address some of the limitations of existing robot-assisted neurosurgical systems [78]. The capability of the system to be used in procedures other than retinal surgery will increase its potential for commercialization.

CHAPTER 7

CONCLUSIONS

In this dissertation, we have presented intuitive methods for telemanipulation of manipulators that use piezoelectric stick-slip actuators (PSSAs). A rate-control telemanipulation method for control of manipulators using PSSAs was developed. The formulation of an impulsive manipulator Jacobian was explained, which enables us to use open-loop models of the manipulator to solve for the input number of steps required by the manipulator for a desired end-effector movement. Experimental results quantifying the effectiveness of the proposed methods were presented. We found that effective teleoperation is possible despite inaccurate joint measurements, and we discussed ways to minimize errors.

The effect of static loads on a prismatic and a rotary PSSA was studied, and empirical model relating the step size to the load was obtained. The actuator-specific parameters of the model can be calibrated for by taking 14 measurements of the average step size (6 for the prismatic joint and 8 for the rotary joint) in specific configurations of the manipulator. The maximum error in the developed load-dependent model for a prismatic and a rotary PSSA is 15% and 2%, respectively, as compared to 40% and 7% for the prismatic and rotary PSSA, respectively, when using a model that does not account for the effect of static loads.

To demonstrate the application of PSSAs in retinal surgery, we have presented a telemanipulation system for retinal surgery that uses a full range of existing disposable instruments. The system uses a PSSA-based manipulator that has submicron resolution at the end-effector, and is compact and light enough that it could reasonably be made head-mounted to passively compensate for head movements. A soft actuator-based and a stepper motor-based mechanism were presented that enable the system to use a variety of existing disposable actuated instruments. An instrument adapter was developed that enables quick-change of instruments during surgery. The instrument actuation mechanisms and instrument change adapter can be easily adapted to work with existing retinal-surgery systems. A custom stylus developed for the Geomagic Touch haptic interface enables intuitive and ergonomic telemanipulation of actuated instruments. Experimental results for simulated membrane

peeling surgery with a force-sensing phantom retina show that skilled surgeons perform as well as manual surgery with the telemanipulated system, and novice surgeons perform better with the telemanipulated system than manual surgery performed by skilled surgeons in certain performance metrics. Training with the telemanipulated system was found to improve operator performance.

We have studied operator performance during a task reminiscent of telemanipulated retinal surgery with three different haptic-interface kinematics: 4-DOF Virtual Trocar, which simulates the surgeons hand directly manipulating the end-effector of the instrument inside the eye; 6-DOF Underactuated, which can be implemented with inexpensive commercial haptic interfaces (e.g., Geomagic Touch); and 4-DOF Separable, which decouples control of translation and rotation of the instrument's end-effector in the eye. The different kinematics were implemented in software on a PHANTOM Premium 6DOF haptic interface. An instrument attached to a retinal-surgery manipulator was telemanipulated to perform a precise positioning task on the force-sensing phantom retina. Results from a study with 12 human subjects show that the subjects' overall performance was best—in terms of the ability to precisely and quickly trace a desired path on the curved surface of the retina while applying gentle forces—with the 6-DOF Underactuated kinematics that represents a compact, inexpensive, and commercially available option. The subjects' subjective preference agrees with the objective performance results.

The studies presented in this dissertation highlight the potential of PSSA-based manipulators in microsurgery, and motivate further research required for the realization of a clinically relevant microsurgical system.

APPENDIX A

KINEMATICS OF 6-DOF RETINAL MANIPULATOR

In this appendix, we derive the forward kinematics, inverse kinematics, and Jacobian of the 6-DOF retinal manipulator.

A.1 Forward Kinematics

The 6-DOF retinal manipulator presented in Chapter 4 is a serial-link manipulator comprising a Cartesian stage with three prismatic joints, and a spherical wrist with three rotary joints attached distally to the prismatic stage. The manipulator was modeled using the Denavit-Hartenberg (DH) convention [79] as shown in Fig. A.1, and Table A.1 shows the DH parameters for the manipulator.

The system shown in Fig. A.1 has seven coordinate frames. Frame 0 represents the base frame. Frame 1, 2, and 3 are attached to the first, second, and third links, and move along $\vec{z}_0$, $\vec{z}_1$, and $\vec{z}_2$ by the joint displacements q_1, q_2, and q_3, respectively. Frame 4 is attached to the fourth link and rotates by q_4 about $\vec{z}_3$. Similary, frame 5 and frame 6 are attached

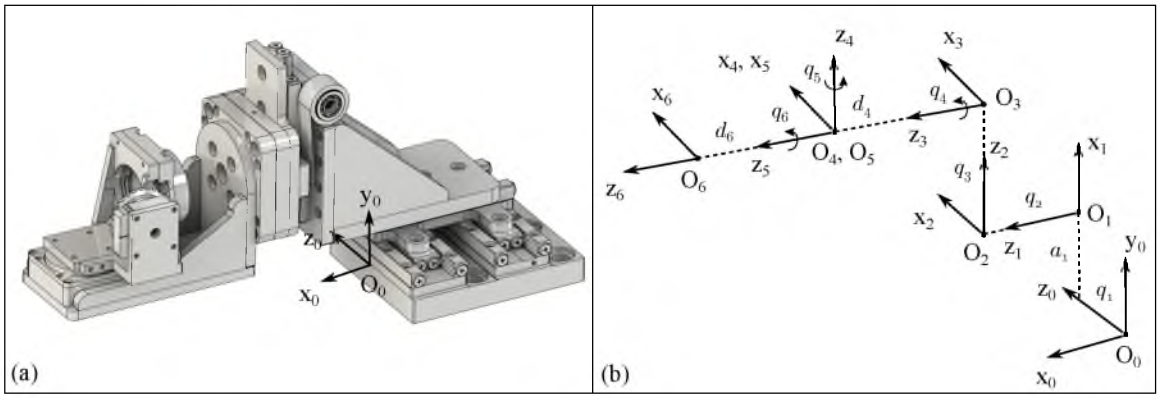

Figure A.1. 6-DOF retinal manipulator. (a) Manipulator in its home position. (b) Coordinate frames for the manipulator with DH parameters.

Table A.1. DH parameters for the 6-DOF retinal manipulator. q_i represents displacement of joint i.

i	α_i	a_i	d_i	θ_i
1	$\frac{\pi}{2}$	a_1	q_1	$\frac{\pi}{2}$
2	$\frac{\pi}{2}$	0	q_2	$\frac{\pi}{2}$
3	$\frac{-\pi}{2}$	0	q_3	0
4	$\frac{\pi}{2}$	0	d_4	q_4
5	$\frac{-\pi}{2}$	0	0	q_5
6	0	0	d_6	q_6

to the fifth and sixth links, and rotate about $\vec{z}_4$ and $\vec{z}_5$ by joint displacements q_5 and q_6, respectively.

The measured values for the DH parameters of the manipulator shown in Fig. A.1(b) are:

$$a_1 = 0.0589\,\text{m}$$
$$d_4 = 0.0912\,\text{m}$$
$$d_6 = 0.0603\,\text{m}$$

The homogeneous transformation from frame i to $i-1$ is given by:

$$^{i-1}T_i = \begin{bmatrix} \cos\theta_i & -\sin\alpha_i\cos\alpha_i & \sin\theta_i\sin\alpha_i & a_i\cos\theta_i \\ \sin\theta_i & \cos\theta_i\cos\alpha_i & -\cos\theta_i\sin\alpha_i & a_i\sin\theta_i \\ 0 & \sin\alpha_i & \cos\alpha_i & d_i \\ 0 & 0 & 0 & 1 \end{bmatrix} \tag{A.1}$$

For the 6-DOF retinal manipulator, the transformation from frame 6 to frame 0 is given by:

$$^0T_6 = \prod_{i=1}^{6} {}^{i-1}T_i \tag{A.2}$$

$$^0T_6 = \begin{bmatrix} sq_5cq_6 & -sq_5sq_6 & cq_5 & d_2 + d_4 + d_6cq_5 \\ -sq_4cq_5cq_6 - cq_4sq_6 & sq_4cq_5sq_6 - cq_4cq_6 & sq_4sq_5 & a_1 + d_3 + d_6sq_4sq_5 \\ cq_4cq_5cq_6 - sq_4sq_6 & -cq_4cq_5sq_6 - sq_4cq_6 & -cq_4sq_5 & d_1 - d_6cq_4sq_5 \\ 0 & 0 & 0 & 1 \end{bmatrix} \tag{A.3}$$

where s_i and c_i represent the sine and cosine of q_i, respectively. Consequently, we deduce the forward kinematics for the manipulator as:

$$ {}^0\vec{d}_{03} = \begin{bmatrix} {}^0d_{03x} \\ {}^0d_{03y} \\ {}^0d_{03z} \end{bmatrix} = \begin{bmatrix} d_2 + d_4 + d_6 c q_5 \\ a_1 + d_3 + d_6 s q_4 s q_5 \\ d_1 - d_6 c q_4 s q_5 \end{bmatrix} \tag{A.4} $$

where ${}^0\vec{d}_{03}$ is the vector from O_0 to O_6, expressed with respect to frame 0.

A.2 Velocity Jacobian

The Jacobian of the 6-DOF retinal manipulator relating end-effector linear (${}^0\dot{d}_{06}$) and angular (${}^0\omega_{06}$) velocities to joint velocities ($\dot{\vec{q}}$) is given by:

$$ \begin{bmatrix} {}^0\dot{d}_{06} \\ {}^0\omega_{06} \end{bmatrix} = J(\vec{q})\dot{\vec{q}} \tag{A.5} $$

$$ = \begin{bmatrix} z_0 & z_1 & z_2 & z_3 \times d_{36} & z_4 \times d_{46} & z_5 \times d_{56} \\ 0 & 0 & 0 & z_3 & z_4 & z_5 \end{bmatrix} \dot{\vec{q}} \tag{A.6} $$

$$ = \begin{bmatrix} 0 & 1 & 0 & 0 & -d_6 s q_5 & 0 \\ 0 & 0 & 1 & -d_6 c q_4 s q_5 & d_6 s q_4 c q_5 & 0 \\ 1 & 0 & 0 & d_6 s q_4 s q_5 & -d_6 c q_4 c q_5 & 0 \\ 0 & 0 & 0 & 1 & 0 & c q_5 \\ 0 & 0 & 0 & 0 & c q_4 & s q_4 s q_5 \\ 0 & 0 & 0 & 0 & s q_4 & -c q_4 s q_5 \end{bmatrix} \begin{bmatrix} \dot{q}_1 \\ \dot{q}_2 \\ \dot{q}_3 \\ \dot{q}_4 \\ \dot{q}_5 \\ \dot{q}_6 \end{bmatrix} \tag{A.7} $$

A.3 Inverse Kinematics

The inverse kinematics for the 6-DOF retinal manipulator is solved by decoupling the motion of the Cartesian stages and the spherical wrist as shown below:

$$ {}^0T_5 = {}^0T_1\,{}^1T_2\,{}^2T_3\,{}^3T_4\,{}^4T_5\,{}^5T_6 \tag{A.8} $$

$$ {}^2T_3{}^{-1}\,{}^1T_2{}^{-1}\,{}^0T_1{}^{-1}\,{}^0T_6 = {}^3T_4\,{}^4T_5\,{}^5T_6 \tag{A.9} $$

$$ \underbrace{\begin{bmatrix} 0 & 0 & 1 & -q_1 \\ 0 & -1 & 0 & a_1 + q_3 \\ 1 & 0 & 0 & -q_2 \\ 0 & 0 & 0 & 1 \end{bmatrix}}_{{}^2T_3{}^{-1}\,{}^1T_2{}^{-1}\,{}^0T_1{}^{-1}} \underbrace{\begin{bmatrix} t_{11} & t_{12} & t_{13} & t_{14} \\ t_{21} & t_{22} & t_{23} & t_{24} \\ t_{31} & t_{32} & t_{33} & t_{34} \\ 0 & 0 & 0 & 1 \end{bmatrix}}_{{}^0T_6} = {}^3T_4\,{}^4T_5\,{}^5T_6 \tag{A.10} $$

$$ \begin{bmatrix} t_{31} & t_{32} & t_{33} & t_{34} - q_1 \\ -t_{21} & -t_{22} & -t_{23} & -t_{24} + a_1 + q_3 \\ t_{11} & t_{12} & t_{13} & t_{14} - q_2 \\ 0 & 0 & 0 & 1 \end{bmatrix} = $$

$$ \begin{bmatrix} c q_4 c q_5 c q_6 - s q_4 s q_6 & -c q_4 c q_5 s q_6 - s q_4 c q_6 & -c q_4 s q_5 & -d_6 c q_4 s q_5 \\ s q_4 c q_5 c q_6 + c q_4 s q_6 & -s q_4 c q_5 s q_6 + c q_4 c q_6 & -s q_4 s q_5 & -d_6 s q_4 s q_5 \\ s q_5 c q_6 & -s q_5 s q_6 & c q_5 & d_4 + d_6 c q_5 \\ 0 & 0 & 0 & 1 \end{bmatrix} \tag{A.11} $$

We first solve for the joint angles of the spherical wrist q_4, q_5, and q_6 from Eq. A.11.

$$\begin{aligned} \sin^2 q_5 &= t_{11}^2 + t_{12}^2 \\ \cos q_5 &= t_{13} \\ q_5 &= \text{atan2}(\pm\sqrt{t_{11}^2 + t_{12}^2}, t_{13}) \end{aligned} \tag{A.12}$$

$$\begin{aligned} -t_{23} &= -sq_4 sq_5 \\ t_{33} &= -cq_4 sq_5 \\ \tan q_4 &= \frac{t_{23}}{-t_{33}} \\ q_4 &= \text{atan2}(t_{23}, -t_{33}) \end{aligned} \tag{A.13}$$

$$q_6 = \text{atan2}(-t_{12}, t_{11}) \tag{A.14}$$

When $\sin q_5 = 0$ in Eq. A.13, a wrist singularity occurs, and only a linear combination of q_4 and q_6 can be found.

1. If $q_5 = 0$, then

$${}^3T_4\,{}^4T_5\,{}^5T_6 = \begin{bmatrix} c(q_4+q_6) & -s(q_4+q_6) & 0 & 0 \\ s(q_4+q_6) & c(q_4+q_6) & 0 & 0 \\ 0 & 0 & 1 & d_4+d_6 \\ 0 & 0 & 0 & 1 \end{bmatrix} \tag{A.15}$$

$$q_4 + q_6 = \text{atan2}(-t_{21}, t_{31}) \tag{A.16}$$

2. If $q_5 = \pi$, then

$${}^3T_4\,{}^4T_5\,{}^5T_6 = \begin{bmatrix} -c(q_4-q_6) & -s(q_4-q_6) & 0 & 0 \\ -s(q_4-q_6) & c(q_4-q_6) & 0 & 0 \\ 0 & 0 & 1 & d_4-d_6 \\ 0 & 0 & 0 & 1 \end{bmatrix} \tag{A.17}$$

$$q_4 - q_6 = \text{atan2}(t_{21}, -t_{31}) \tag{A.18}$$

One possible solution is to arbitrarily set $q_6 = 0$ in Eq. A.16 and Eq. A.18.
From Eq. A.11, q_4, and q_5, we can solve for q_1, q_2, and q_3.

$$q_1 = t_{34} + d_6 cq_4 sq_5 \tag{A.19}$$

$$q_2 = t_{14} - d_4 - d_6 cq_5 \tag{A.20}$$

$$q_3 = t_{24} - a_1 - d_6 sq_4 sq_5 \tag{A.21}$$

Thus, we have solved for the joint displacements given the pose of frame 6 with respect to frame 0.

APPENDIX B

KINEMATIC CONDITIONING DURING CONSTRAINED MOTION

In this appendix, we discuss the kinematic conditioning of the manipulator for the constrained manipulation task in retinal surgery. The constrained Jacobian used for characterizing kinematic conditioning was formulated using the restricted Jacobian [80] and task priority [81] adapted for constrained manipulation in robot-assisted surgery [82].

B.1 Formulation of Jacobian for Constrained Manipulation

The trocar constraint in retinal surgery requires that velocities tangent to the surface of the sclera at the trocar should be zero. Due to the trocar constraint, only 4-DOF motions (3-DOF translation and 1-DOF rotation about the instrument's shaft) are controlled by the operator, and 2-DOF are used to maintain the trocar constraint.

Consider the tangent plane in $\mathbb{R}^3$ to be defined by the trocar point $\vec{x}_t$, and a normal to the plane $\hat{n}$. Let $\vec{x}_{rcm}$ be a point on the instrument's shaft that is currently passing through $\vec{x}_t$, and $\vec{x}$ is the position of the end-effector. $\dot{\vec{x}}_{rcm}$ and $\dot{\vec{x}}$ are the velocities at the trocar and at the end-effector, respectively, given by:

$$\dot{\vec{x}}_{rcm} = J_{rcm}(\vec{q})\dot{\vec{q}} \tag{B.1}$$

$$\dot{\vec{x}} = J_v(\vec{q})\dot{\vec{q}} \tag{B.2}$$

where $J_{rcm}(\vec{q}) \in \mathbb{R}^{3\times n}$. $J(\vec{q}) = \begin{bmatrix} J_v \\ J_\omega \end{bmatrix}$ where J_v and J_ω are the translational and rotational submatrices, respectively. $J(\vec{q})$ is given by Eq. A.5. For simplicity of notation, $J_i(\vec{q})$ will be referred to as J_i henceforth.

The velocity of the instrument along the tangent plane at the trocar should be zero. This constraint can be expressed in terms of joint velocities as:

$$A\dot{\vec{x}}_{rcm} = AJ_{rcm}\dot{\vec{q}} = H\dot{\vec{q}} = 0 \tag{B.3}$$

$$A = \begin{bmatrix} \hat{l}^T \\ \hat{m}^T \end{bmatrix} \tag{B.4}$$

where $\hat{l}$ and $\hat{m}$ are orthogonal vectors spanning the tangent plane and $\hat{l} \times \hat{m} = \hat{n}$, and H is the constraint Jacobian at the trocar.

From [82], for a constrained task with primary task Jacobian H and secondary task Jacobian J_v, the end-effector velocity $\dot{\vec{x}}$ is given by:

$$\dot{\vec{x}} = \hat{J}\dot{\vec{q}} \tag{B.5}$$

$$\hat{J} = J_v(I - H^+H) \tag{B.6}$$

where H^+ is the psuedoinverse of H given by:

$$H^+ = H^T(HH^T)^{-1} \tag{B.7}$$

In Eq. B.5, the Jacobian at the end-effector J_v is projected on to the null space of the constraint Jacobian H.

B.2 Scaling Matrices to Normalize Jacobian

Because the manipulator uses a combination of prismatic and rotary actuators, the elements of Jacobians H and J_v have different units. It was shown in [83] that the condition number and generalized inverse of the Jacobian matrix are not invariant to change in units. The concept of a "characteristic length" was proposed in [84], and scaling matrices that depend on the capabilities of the actuators were proposed in [85] to render the Jacobian matrix unit invariant. We use scaling matrices as described in [85] to normalize the Jacobian matrices of our manipulator.

Let $\Delta\dot{\vec{x}}$ be the vector of task velocity ($\dot{x}_i$) normalized by the maximum task velocity ($\dot{x}_{i,\max}$), and $\Delta\dot{\vec{q}}$ be the vector of joint velocity ($\dot{q}_i$) normalized by the maximum joint ($\dot{\vec{q}}_{i,\max}$) . $\Delta\dot{\vec{x}}$ and $\Delta\dot{\vec{q}}$ are given by:

$$\dot{\vec{x}} = S_T\Delta\dot{\vec{x}} \tag{B.8}$$

$$\dot{\vec{q}} = S_J\Delta\dot{\vec{q}} \tag{B.9}$$

where S_T and S_J are diagonal matrices with maximum task and joint velocities as diagonal elements, respectively. From Eq. B.2, Eq. B.8, and Eq. B.9:

$$S_T\Delta\dot{\vec{x}} = JS_J\Delta\dot{\vec{q}} \tag{B.10}$$

$$\Delta\dot{\vec{x}} = S_T^{-1}JS_J\Delta\dot{\vec{q}} = J_n\Delta\dot{\vec{q}} \tag{B.11}$$

where $J_n = S_T^{-1}JS_J$ is the normalized Jacobian that maps normalized joint velocities to normalized task velocities. The elements of S_J are obtained from actuator specifications. S_T

can be used to set task-space velocity specifications for a manipulator. For our manipulator, we used the maximum measured task-space velocities as elements of S_T. S_J and S_T for the manipulator are given by:

$$S_J = \text{diag}(\begin{bmatrix} 0.013\,\frac{\text{m}}{\text{s}} & 0.013\,\frac{\text{m}}{\text{s}} & 0.013\,\frac{\text{m}}{\text{s}} & 0.26\,\frac{\text{rad}}{\text{s}} & 0.44\,\frac{\text{rad}}{\text{s}} & 0.44\,\frac{\text{rad}}{\text{s}} \end{bmatrix}) \tag{B.12}$$

$$S_T = \text{diag}(\begin{bmatrix} 0.006\,\frac{\text{m}}{\text{s}} & 0.006\,\frac{\text{m}}{\text{s}} & 0.006\,\frac{\text{m}}{\text{s}} \end{bmatrix}) \tag{B.13}$$

The normalized Jacobian matrices $J_{v,n}$ and H_n are used to form the normalized constrained Jacobian in Eq. B.5 as:

$$\hat{J}_n = J_{v,n}(I - H_n^+ H_n) \tag{B.14}$$

B.3 Kinematic Conditioning in the Workspace

To study the conditioning of the manipulator during constrained motion, we look at the condition number of J_n defined as:

$$\kappa = \sqrt{\text{tr}(J_n J_n^T)\text{tr}((J_n J_n^T)^{-1})} \tag{B.15}$$

Fig. B.1 shows κ for the manipulator for the reachable workspace inside the eye. κ reduces as the manipulator approaches its wrist singularity when the instrument shaft is parallel to the X axis in Fig. B.1(b). One might presume that κ would be maximum when the instrument shaft is vertical as the wrist of the manipulator is in its best-conditioned pose, but an algorithmic singularity occurs due to the constraint at the trocar. As a result, κ reduces as the end-effector moves closer to the trocar.

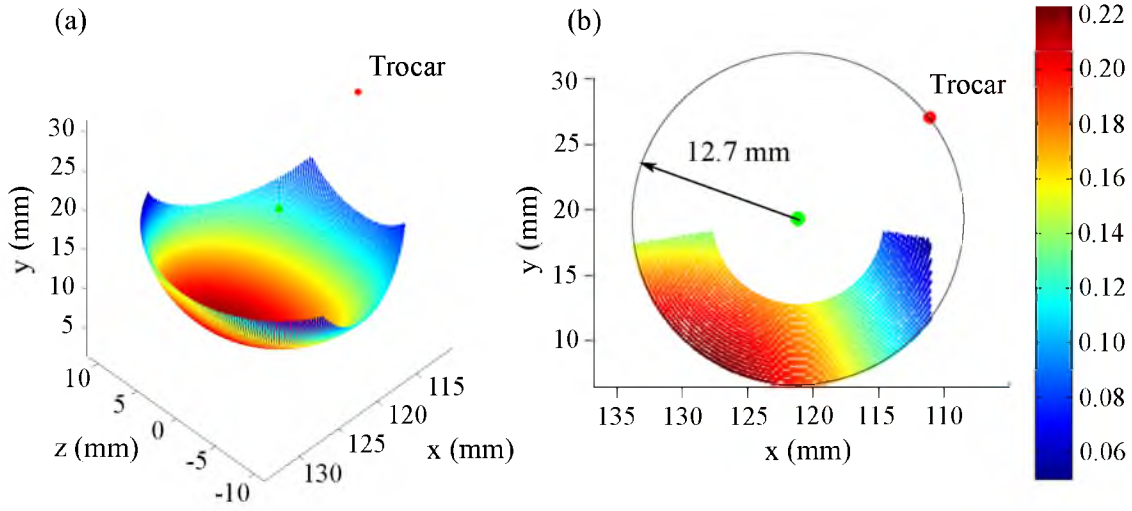

Figure B.1. Kinematic conditioning for the manipulator. (a) κ for the reachable workspace on the surface of the retina. (b) Due to an algorithmic singularity at the trocar, κ reduces as the end-effector approaches the trocar.

APPENDIX C

VERIFICATION OF PRECISION AND RESOLUTION AT THE END-EFFECTOR

In this appendix, we present experiments performed to verify the precision and resolution at the end-effector attached to the 6-DOF retinal manipulator.

C.1 Precision

To verify the precision of our manipulator, we performed an experiment while imaging the end-effector (tungsten probe attached using the quick-change adapter) under a VHX-5000 digital microscope [86]. A virtual RCM point was implemented in the workspace of the manipulator, and the tool tip was positioned at a distance from the trocar that is representative of the distance of the retinal surface from the trocar. From an initial position, the end-effector was commanded to move by 100 microns along an axis, and then another command was issued to return the end-effector to the initial position. This was performed five times, and spread in the end-effector position, which indicates the repeatability/precision at the end-effector, was found to be less than 1 micron. The sequence of images in Fig. C.1 shows the position of the end-effector before and after the 100 micron commands were given. Figures on the left column show the initial position of the probe tip and figures on the right column show the end-position of the probe tip. The blue mesh was superimposed by the microscope and has a width of 1 micron. The red box was added to indicate that the position of the end-effector before and after the movement command is within a micron (within the same box). This experiment shows that the plastic 3D printed parts are stiff and do not affect the precision of our system.

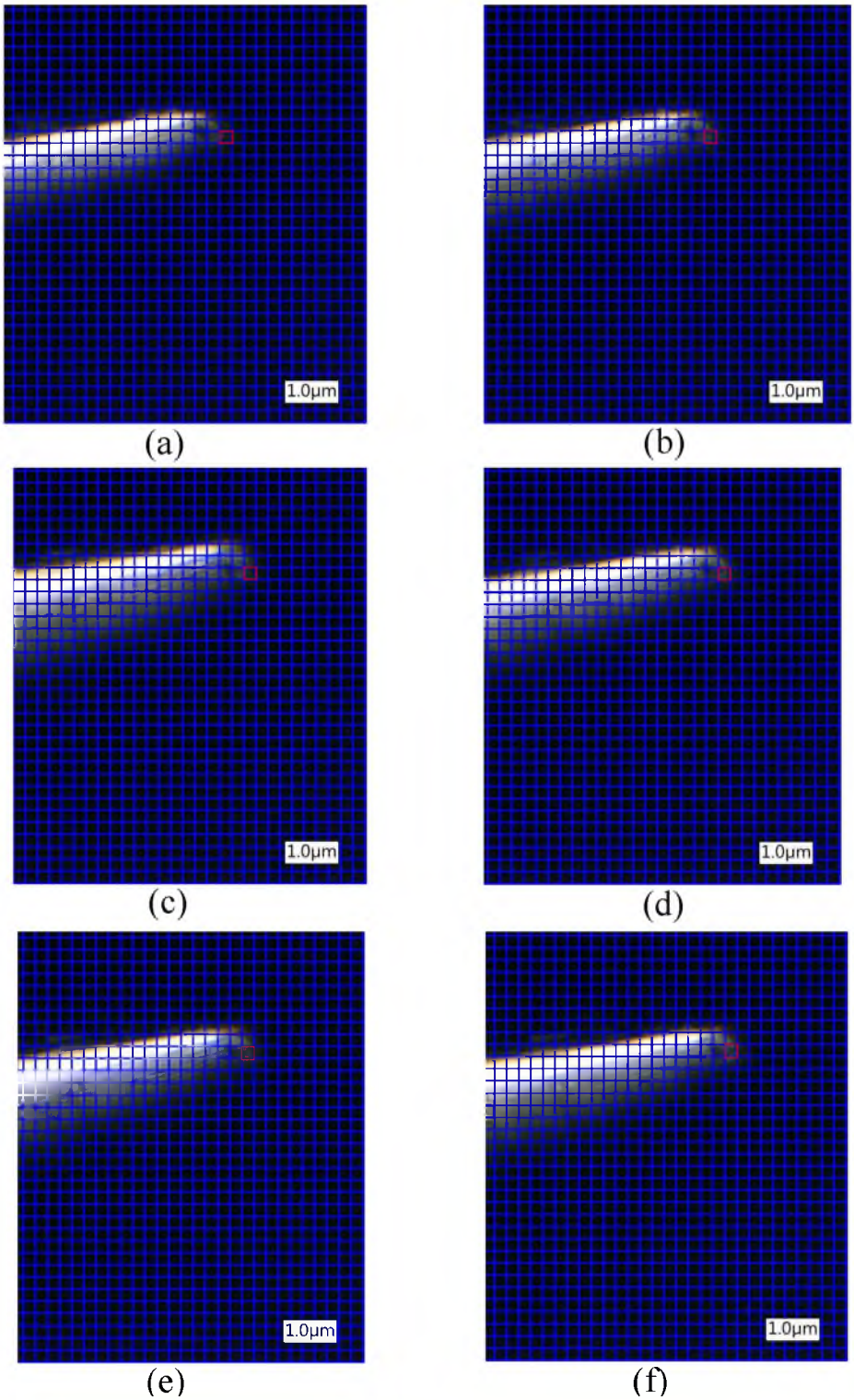

Figure C.1. Images from a microscope for verifying precision. (a), (c), (e) Initial position of the end-effector. (b), (d), (f) Position of the end-effector after two consecutive movement commands of 100 microns and -100 microns at the end-effector along the Y-axis. The blue mesh was superimposed by the microscope and have a width of 1 micron. The red box was added to indicate that the position of the end-effector before and after the movement command is within a micron (within the same box).

C.2 Resolution

The resolution at the end-effector for our manipulator is the worst-case resolution of the linear actuators. This resolution is specific to the controller described in Section 2.3.2. The maximum sensor resolution on the linear stages are 100 nm, and the linear stages are capable of moving in 50 nm steps.

The resolution was measured by commanding 10 steps to the linear stages, measuring the displacement for the 10 steps from joint sensors, and dividing the displacement by 10. To verify the resolution, the end-effector was imaged under the microscope while commands were given to the end-effector. The series of images in Fig. C.2 show the displacement of the end-effector for 10 step commands. It can be seen that the displacement from (a)-(b), and (b)-(c) is less than 6 microns, and the corresponding displacement from joint sensors was 4.6 microns and 5.5 microns, respectively. This was repeated for 5 trials in each direction, and the worst-case resolution was found to be 550 nm obtained by dividing the displacement by 10.

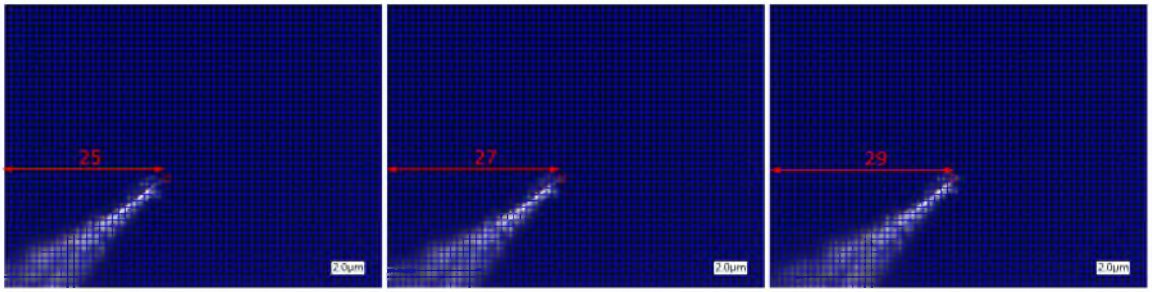

Figure C.2. Images from a microscope for verifying resolution. (a) Initial position of the end-effector. (b) Position of the end-effector after 10 step commands. (c) Position of the end-effector after another 10 step commands from the position of the end-effector in (b).

REFERENCES

[1] T. Higuchi and Y. Yamagata, "Micro robot arm utilizing rapid deformations of peizoelectric elements," *Advanced Robotics*, vol. 6, no. 3, pp. 353–360, 1992.

[2] "Zyvex Nanomanipulator," http://www.zyvex.com/.

[3] "Kleindiek Nanotechnik MM3A," http://www.nanotechnik.com/.

[4] "Imina Techonologies miBot," http://www.imina.ch/.

[5] "Attocube Nanopositioners," http://www.attocube.com/.

[6] "SmarAct GmbH," http://www.smaract.de.

[7] B. E. Kratochvil, L. Dong, and B. J. Nelson, "Real time rigid-body visual tracking in a scanning electron microscope," *Int. J. Robotics Research*, vol. 28, no. 4, pp. 488–511, 2009.

[8] H. Hötzendorfer, I. Giouroudi, S. Bou, and M. Ferros, "Evaluation of different control algorithms for a micromanipulation system," in *Int. Conf. Engineering and Mathematics*, 2006.

[9] J.-M. Breguet and R. Clavel, "Stick and slip actuators: design, control, performances and applications," in *Proc. Micromechatronics and Human Science*, 1998, pp. 89–95.

[10] S. H. Chang and S. S. Li, "A high resolution long travel friction-drive micropositioner with programmable step size," *Review of Scientific Instruments*, vol. 70, no. 6, pp. 2776–2782, 1999.

[11] J. Y. Peng and X. B. Chen, "Modeling of piezoelectric-driven stick-slip actuators," *IEEE/ASME Trans. Mechatronics*, vol. 16, no. 2, pp. 394–399, 2011.

[12] A. J. Lockwood, J. J. Wang, R. Gay, and B. J. Inkson, "Characterising performance of TEM compatible nanomanipulation slip-stick intertial sliders against gravity," *Jounal of Physics:Conference Series*, vol. 126, no. 1, p. 012096, 2008.

[13] M. Nasseri, M. Eder, S. Nair, E. Dean, M. Maier, D. Zapp, C. Lohmann, and A. Knoll, "The introduction of a new robot for assistance in ophthalmic surgery," in *Int. Conf. IEEE Engineering in Medicine and Biology Society*, 2013, pp. 5682–5685.

[14] R. Hendrix, N. Rosielle, and H. Nijmeijer, "Design of a haptic master interface for robotically assisted vitreo-retinal eye surgery," in *Int. Conf. on Advanced Robotics*, 2009, pp. 1–6.

[15] A. Gijbels, E. Vander Poorten, P. Stalmans, H. Van Brussel, and D. Reynaerts, "Design of a teleoperated robotic system for retinal surgery," in *Proc. IEEE Int. Conf. Robotics and Automation*, May 2014, pp. 2357–2363.

[16] H. Takahashi, T. Yonemura, N. Sugita, M. Mitsuishi, S. Sora, A. Morita, and R. Mochizuki, "Master manipulator with higher operability designed for micro neuro surgical system," in *Proc. IEEE Int. Conf. Robotics and Automation*, 2008, pp. 3902–3907.

[17] ©2011 IEEE. Reprinted, with permission, from, M. Nambi and A. Damani and J. J. Abbott, "Toward intuitive teleoperation of micro/nano-manipulators with piezoelectric stick-slip actuators," in *Proc. IEEE/RSJ Int. Conf. Intelligent Robots and Systems*, 2011, pp. 445–450.

[18] J. J. Abbott, Z. Nagy, F. Beyeler, and B. J. Nelson, "Robotics in the small, Part I: Microbotics," *IEEE Robotics and Automation Mag.*, vol. 14, no. 2, pp. 92 –103, june 2007.

[19] L. Dong and B. J. Nelson, "Robotics in the small, Part II: Nano-robotics," *IEEE Robotics and Automation Mag.*, vol. 14, no. 3, pp. 111 –121, sept. 2007.

[20] S. Fatikow and V. Eichhorn, "Nanohandling automation: trends and current developments," *Proc. Institution of Mechanical Engineers, Part C: J. Mechanical Engineering Science*, vol. 222, no. 7, pp. 1353–1369, 2008.

[21] M. Rakotondrabe, Y. Haddab, and P. Lutz, "Voltage/frequency proportional control of stick-slip micropositioning systems," *IEEE Trans. on Control Systems Technology*, vol. 16, no. 6, pp. 1316–1322, 2008.

[22] B. Sedghi, B. Srinivasan, and R. Longchamp, "Control of hybrid systems via dehybridization," in *Proc. American Control Conference*, 2002, pp. 692–697.

[23] H. C. Liaw, B. Shirinzadeh, and J. Smith, "Enhanced sliding mode motion tracking control of piezoelectric actuators," *Sensors and Actuators A: Physical*, vol. 138, no. 1, pp. 194–202, 2007.

[24] R. Saeidpourazar and N. Jalili, "Nano-robotic manipulation using a RRP nanomanipulator: Part A–Mathematical modeling and development of a robust adaptive driving mechanism," *Applied Mathematics and Computation*, vol. 206, pp. 618–627, 2008.

[25] ——, "Nano-robotic manipulation using a RRP nanomanipulator: Part B–Robust control of manipulator's tip using fused visual servoing and force sensor feedbacks," *Applied Mathematics and Computation*, vol. 206, pp. 628–642, 2008.

[26] W. Zesch, R. Buchi, A. Codourey, and R. Siegwart, "Inertial drives for micro- and nanorobots: Two novel mechanisms," in *SPIE Microrobotics and Micromechanical Systems*, 1995, pp. 80–88.

[27] O. Tonet, M. Marinelli, G. Megali, A. Sieber, P. Valdastri, A. Menciassi, and P. Dario, "Control of a teleoperated nanomanipulator with time delay under direct vision feedback," in *Proc. IEEE Int. Conf. Robotics and Automation*, 2007, pp. 3514–3519.

[28] C. Ware and R. Arsenault, "Frames of reference in virtual object rotation," in *Symp. Applied Perception in Graphics and Visualization*, 2004, pp. 135–141.

[29] Reprinted with permission from Springer Science and Business Media. A. Damani, M. Nambi, and J. J. Abbott, "An empirical study of static loading on piezoelectric stick-slip actuators of micromanipulators," in *Experimental Robotics*, 2013, vol. 88, pp. 55–69.

[30] J.-M. Breguet, W. Driesen, F. Kaegi, and T. Cimprich, "Applications of piezo-actuated micro-robots in micro-biology and material science," in *Int. Conf. on Mechatronics and Automation*, 2007, pp. 57–62.

[31] D. Schurzig, R. F. Labadie, A. Hussong, T. S. Rau, and R. J. Webster III, "Design of a tool integrating force sensing with automated insertion in cochlear implantation," *IEEE/ASME Trans. Mechatronics*, vol. 17, no. 2, pp. 381–389, 2012.

[32] S. Fatikow, T. Wich, H. Hülsen, T. Sievers, and M. Jähnisch, "Microbot system for automatic nanohandling inside a scanning electron microscope," *IEEE/ASME Trans. Mechatronics*, vol. 12, no. 3, pp. 244–252, 2007.

[33] M. Nambi, A. Damani, and J. J. Abbott, "Toward intuitive teleoperation of micro/nano-manipulators with piezoelectric stick-slip actuators," in *Proc. IEEE/RSJ Int. Conf. Intelligent Robots and Systems*, 2011, pp. 445–450.

[34] H. Jung, J. Y. Shim, and D. Gweon, "New open-loop actuating method of piezoelectric actuators for removing hysteresis and creep," *Review of Scientific Instruments*, vol. 71, no. 9, pp. 3436–3440, 2000.

[35] Y. Lv and Y. Wei, "Study on open-loop precision positioning control of a micropositioning platform using a piezoelectric actuator," in *Proc. World Congress on Intelligent Control and Automation*, 2004, pp. 1255–1259.

[36] J. W. Li, G. S. Yang, W. J. Zhang, S. D. Tu, and X. B. Chen, "Thermal effect on piezoelectric stick-slip actuator systems." *Review of Scientific Instruments*, vol. 79, no. 4, p. 046108, 2008.

[37] P. K. Gupta, P. S. Jensen, and E. de Juan Jr., "Surgical force and tactile perception during retinal microsurgery," in *Int. Conf. Medical Image Computing and Computer-Assisted Intervention*, vol. 1679, 1999, pp. 1218–1225.

[38] A. D. Jagtap and C. N. Riviere, "Applied force during vitreoretinal microsurgery with handheld instruments," in *Int. Conf. IEEE Engineering in Medicine and Biology Society*, 2004, pp. 2771–2773.

[39] S. P. N. Singh and C. N. Riviere, "Physiological tremor amplitude during retinal microsurgery," in *IEEE Northeast Bioengineering Conf.*, 2002, pp. 171–172.

[40] L. F. Hotraphinyo and C. N. Riviere, "Three-dimensional accuracy assessment of eye surgeons," in *IEEE Int. Conf. Engineering in Medicine and Biology Society*, 2001, pp. 3458–3461.

[41] C. N. Riviere, R. S. Rader, and P. K. Khosla, "Characteristics of hand motion of eye surgeons," in *Int. Conf. IEEE. Engineering in Medicine and Biology Society*, 1997, pp. 1690–1693.

[42] C. N. Riviere and P. S. Jensen, "A study of instrument motion in retinal microsurgery," in *Int. Conf. IEEE Engineering in Medicine and Biology Society*, 2000, pp. 59–60.

[43] M. Balicki, A. Uneri, I. Iordachita, J. Handa, P. Gehlbach, and R. Taylor, "Micro-force sensing in robot assisted membrane peeling for vitreoretinal surgery," in *Int. Conf. Medical Image Computing and Computer-Assisted Intervention 2010*, ser. LNCS, 2010, vol. 6363, pp. 303–310.

[44] C. A. McCannel, E. J. Olson, M. J. Donaldson, S. J. Bakri, J. S. Pulido, and D. Mueller, "Snoring is associated with unexpected patient head movement during monitored anesthesia care vitreoretinal surgery," *Retina*, vol. 32, no. 7, pp. 1324–7, 2012.

[45] J. R. Wilkins, C. A. Puliafito, M. R. Hee, J. S. Duker, E. Reichel, J. G. Coker, J. S. Schuman, E. A. Swanson, and J. G. Fujimoto, "Characterization of epiretinal membranes using optical coherence tomography," *Ophthalmology*, vol. 103, no. 12, pp. 2142–2151, 1996.

[46] P. B. Henrich, C. A. Monnier, M. Loparic, and P. C. Cattin, "Material properties of the internal limiting membrane and their significance in chromovitrectomy," *Ophthalmologica*, vol. 230, no. 2, pp. 11–20, 2013.

[47] G. Donati, A. D. Kapetanios, and C. J. Pournaras, "Complications of surgery for epiretinal membranes," *Graefe's archive for clinical and experimental ophthalmology*, vol. 236, no. 10, pp. 739–746, 1998.

[48] D. Harmon and J. Merritt, "Demand for ophthalmic services and ophthalmologists—a resource assessment." *A Study Prepared by Market Scope, LLC*, pp. 1–2, 2009.

[49] P. S. Jensen, K. W. Grace, R. Attariwala, J. E. Colgate, and M. R. Glucksberg, "Toward robot-assisted vascular microsurgery in the retina," *Graefe's archive for clinical and experimental ophthalmology*, vol. 235, no. 11, pp. 696–701, 1997.

[50] D.-Y. Yu, S. Cringle, and I. Constable, "Robotic ocular ultramicrosurgery," *Australian and New Zealand J. of Ophthalmology*, vol. 26, pp. S6–S8, 1998.

[51] W. Wei, C. Popplewell, S. Chang, H. F. Fine, and N. Simaan, "Enabling technology for microvascular stenting in ophthalmic surgery," *J. Medical Devices*, vol. 4, no. 1, p. 14503, 2010.

[52] Y. Ida, N. Sugita, T. Ueta, Y. Tamaki, K. Tanimoto, and M. Mitsuishi, "Microsurgical robotic system for vitreoretinal surgery," *Int. J. Computer Assisted Radiology and Surgery*, vol. 7, no. 1, pp. 27–34, 2012.

[53] H. Meenink, R. Hendrix, G. Naus, M. Beelen, H. Nijmeijer, M. Steinbuch, E. Oosterhout, and M. Smet, "Robot-assisted vitreoretinal surgery," *Medical robotics: minimally invasive surgery*, pp. 185–209, 2012.

[54] E. Rahimy, J. Wilson, T. Tsao, S. Schwartz, and J. Hubschman, "Robot-assisted intraocular surgery: development of the IRISS and feasibility studies in an animal model," *Eye*, vol. 27, no. 8, pp. 972–978, 2013.

[55] A. Uneri, M. A. Balicki, J. Handa, P. Gehlbach, R. H. Taylor, and I. Iordachita, "New steady-hand eye robot with micro-force sensing for vitreoretinal surgery," in *IEEE Int. Conf. Biomedical Robotics and Biomechatronics*, 2010, pp. 814–819.

[56] A. Gijbels, E. Vander Poorten, B. Gorissen, A. Devreker, P. Stalmans, and D. Reynaerts, "Experimental validation of a robotic comanipulation and telemanipulation system for retinal surgery," in *IEEE Int. Conf. Biomedical Robotics and Biomechatronics*, 2014, pp. 144–150.

[57] R. A. MacLachlan, B. C. Becker, J. Cuevas Tabarés, G. W. Podnar, L. A. Lobes, and C. N. Riviere, "Micron: an actively stabilized handheld tool for microsurgery," *IEEE Trans. Robotics*, vol. 28, no. 1, pp. 195–212, 2012.

[58] C. Song, P. L. Gehlbach, and J. U. Kang, "Active tremor cancellation by a "smart" handheld vitreoretinal microsurgical tool using swept source optical coherence tomography," *Opt. Express*, vol. 20, no. 21, pp. 23 414–23 421, 2012.

[59] A. Saxena and R. Patel, "An active handheld device for compensation of physiological tremor using an ionic polymer metallic composite actuator," in *Proc. IEEE/RSJ Int. Conf. Intelligent Robots and Systems*, 2013, pp. 4275–4280.

[60] W. Latt, U.-X. Tan, C. Shee, and W. Ang, "A compact hand-held active physiological tremor compensation instrument," in *IEEE/ASME Int. Conf. on Advanced Intelligent Mechatronics*, 2009, pp. 711–716.

[61] M. Nambi, P. S. Bernstein, and J. J. Abbott, "A compact retinal-surgery telemanipulator that uses disposable instruments," in *Int. Conf. Medical Image Computing and Computer-Assisted Intervention*, 2015.

[62] Y. Xia and G. M. Whitesides, "Soft lithography," *Annual review of materials science*, vol. 28, no. 1, pp. 153–184, 1998.

[63] H. Yu, J.-H. Shen, K. M. Joos, and N. Simaan, "Design, calibration and preliminary testing of a robotic telemanipulator for OCT guided retinal surgery," in *Proc. IEEE Int. Conf. Robotics and Automation*, 2013, pp. 225–231.

[64] M. Balicki, J.-H. Han, I. Iordachita, P. Gehlbach, J. Handa, R. Taylor, and J. Kang, "Single fiber optical coherence tomography microsurgical instruments for computer and robot-assisted retinal surgery," in *Int. Conf. Medical Image Computing and Computer-Assisted Intervention*, 2009, pp. 108–115.

[65] A. Gupta, B. Gonenc, M. Balicki, K. Olds, J. Handa, P. Gehlbach, R. H. Taylor, and I. Iordachita, "Human eye phantom for developing computer and robot-assisted epiretinal membrane peeling," in *Int. Conf. IEEE Engineering in Medicine and Biology Society*, 2014, pp. 6864–6867.

[66] Y. Noda, Y. Ida, S. Tanaka, T. Toyama, M. F. Roggia, Y. Tamaki, N. Sugita, M. Mitsuishi, and T. Ueta, "Impact of robotic assistance on precision of vitreoretinal surgical procedures," *PloS one*, vol. 8, no. 1, p. e54116, 2013.

[67] H. Yu, J.-H. Shen, R. J. Shah, N. Simaan, and K. M. Joos, "Evaluation of microsurgical tasks with OCT-guided and/or robot-assisted ophthalmic forceps," *Biomedical optics express*, vol. 6, no. 2, pp. 457–472, 2015.

[68] T. Ueta, Y. Yamaguchi, Y. Shirakawa, T. Nakano, R. Ideta, Y. Noda, A. Morita, R. Mochizuki, N. Sugita, M. Mitsuishi, and Y. Tamaki, "Robot-assisted vitreoretinal surgery: development of a prototype and feasibility studies in an animal model," *Ophthalmology*, vol. 116, no. 8, pp. 1538–1543, 2009.

[69] H. F. Fine, W. Wei, R. E. Goldman, and N. Simaan, "Robot-assisted ophthalmic surgery," *Canadian Journal of Ophthalmology*, vol. 45, no. 6, pp. 581–584, 2010.

[70] W. Wei, R. Goldman, N. Simaan, H. Fine, and S. Chang, "Design and theoretical evaluation of micro-surgical manipulators for orbital manipulation and intraocular dexterity," in *Proc. IEEE Int. Conf. Robotics and Automation*, 2007, pp. 3389–3395.

[71] M. R. Masliah and P. Milgram, "Measuring the allocation of control in a 6 degree-of-freedom docking experiment," in *Proc. SIGCHI Conf. on Human Factors in Computing Systems*, 2000, pp. 25–32.

[72] R. J. K. Jacob, L. E. Sibert, D. C. McFarlane, and M. P. Mullen Jr, "Integrality and separability of input devices," *ACM Trans. on Computer-Human Interaction*, vol. 1, no. 1, pp. 3–26, 1994.

[73] J. B. Boyle and C. H. Shea, "Wrist and arm movements of varying difficulties," *Acta Psychologica*, vol. 137, no. 3, pp. 382 – 396, 2011.

[74] G. D. Langolf, D. B. Chaffin, and J. A. Foulke, "An investigation of fitts law using a wide range of movement amplitudes," *J. of Motor Behavior*, vol. 8, no. 2, pp. 113–128, 1976.

[75] D. K. Kumar, B. Aliahmad, H. Hao, M. Z. Che Azemin, and R. Kawasaki, "A method for visualization of fine retinal vascular pulsation using nonmydriatic fundus camera synchronized with electrocardiogram," *ISRN Ophthalmology*, vol. 2013, 2013.

[76] J. B. Alvarez, J. Zhang, and A. Seam, "Method, apparatus and a system for robotic assisted surgery," Apr. 23 2013, US Patent App. 13/868,769.

[77] H. J. Marcus, K. Zareinia, L. S. Gan, F. W. Yang, S. Lama, G.-Z. Yang, and G. R. Sutherland, "Forces exerted during microneurosurgery: a cadaver study," *The Int. J. of Medical Robotics and Computer Assisted Surgery*, vol. 10, no. 2, pp. 251–256, 2014.

[78] L. Zamorano, Q. Li, S. Jain, and G. Kaur, "Robotics in neurosurgery: state of the art and future technological challenges," *Int. J. Medical Robotics and Computer Assisted Surgery*, vol. 1, no. 1, pp. 7–22, 2004.

[79] P. P. Richard, *Robot Manipulators: Mathematics, Programming and Control.* The MIT Press, 1981.

[80] D. N. Nenchev, "Restricted jacobian matrices of redundant manipulators in constrained motion tasks," *Int. J. Robotics Research*, vol. 11, no. 6, pp. 584–597, 1992.

[81] Y. Nakamura, *Advanced robotics: redundancy and optimization.* Addison-Wesley Longman Publishing Co., Inc., 1990.

[82] H. Azimian, R. V. Patel, and M. D. Naish, "On constrained manipulation in robotics-assisted minimally invasive surgery," in *IEEE Int. Conf. Biomedical Robotics and Biomechatronics*, 2010, pp. 650–655.

[83] K. L. Doty, C. Melchiorri, E. M. Schwartz, and C. Bonivento, "Robot manipulability," *IEEE Trans. Robotics*, vol. 11, no. 3, pp. 462–468, 1995.

[84] M. Tandirci, J. Angeles, and F. Ranjbaran, "The characteristic point and the characteristic length of robotic manipulators," *Proc. of ASME Conf. Robotics, Spatial Mechanisms & Mech. Sys.*, vol. 45, pp. 203–208, 1992.

[85] L. Stocco, S. Salcudean, and E. Sassani, "Matrix normalization for optimal robot design," in *Proc. IEEE Int. Conf. Robotics and Automation*, vol. 2, 1998, pp. 1346–1351.

[86] "Keyence VHX5000," http://www.keyence.com/.